論文 / 著書情報
Article / Book Information

題目(和文)	現実都市域におけるガスト指標のラージ・エディー・シミュレーション
Title(English)	LARGE EDDY SIMULATION OF THE GUST INDEX OVER A REALISTIC URBAN AREA
著者(和文)	ヌルルフダアハマド
Author(English)	Nurul Huda Ahmad
出典(和文)	学位:博士(工学), 学位授与機関:東京工業大学, 報告番号:甲第10164号, 授与年月日:2016年3月26日, 学位の種別:課程博士, 審査員:神田 学,高木 泰士,秋田 大輔,木内 豪,中村 恭志
Citation(English)	Degree:Doctor (Engineering), Conferring organization: Tokyo Institute of Technology, Report number:甲第10164号, Conferred date:2016/3/26, Degree Type:Course doctor, Examiner:,,,,
学位種別(和文)	博士論文
Type(English)	Doctoral Thesis

LARGE EDDY SIMULATION OF THE GUST INDEX OVER A REALISTIC URBAN AREA

（現実都市域におけるガスト指標のラージ・エディー・シミュレーション）

NURUL HUDA BINTI AHMAD

TOKYO INSTITUTE OF TECHNOLOGY

LARGE EDDY SIMULATION OF THE GUST INDEX OVER A REALISTIC URBAN AREA

（現実都市域におけるガスト指標のラージ・エディー・シミュレーション）

NURUL HUDA BINTI AHMAD

A thesis submitted in partial fulfilment of the
requirements for the award of the degree of
Doctor of Engineering

Department of International Development Engineering
Graduate School of Science and Engineering
Tokyo Institute of Technology

MARCH 2016

"I hereby declare that I have read this thesis and in
my opinion this thesis is sufficient in terms of scope and
quality for the award of the degree of
Doctor of Engineering."

Signature : .....

Name of Supervisor : **PROF. DR. MANABU KANDA**

Date : .....

"I declare that this thesis entitled

Large Eddy Simulation of the Gust Index over a Realistic Urban Area

is the result of my own research except as cited in the references.

The thesis has not been accepted for any degree and is

not concurrently submitted in candidature of any other degree."

Signature : .....

Name : **NURUL HUDA BINTI AHMAD**

Date : .....

A very honour dedication to my beloved
parents, Mr. Ahmad Bin Ariffin and Mrs. Zariah Binti Che Kob,
my supportive siblings and friends.

ACKNOWLEDGEMENT

In the process of completing this work, I received contributions from a number of academicians and organizations. To them, I wish to express my sincere appreciation to my supervisor, Prof. Dr. Manabu Kanda and Dr. Atsushi Inagaki for initiating this research topic and for their encouragement and guidance. Also without the support from Prof. Dr. Takayuki Aoki and Dr. Naoyuki Onodera in performing the large eddy simulation (LES) with lattice Boltzmann method (LBM), this work would not have been the same as presented. I would also like to thank the PALM group and Prof. Dr. Siegfried Raasch at the Universität Hannover for their assistance while testing the parallelized large eddy simulation model (PALM). This research could not be accomplished without the support from the Japan Society for the Promotion of Science (JSPS) KAKENHI Grant Numbers 25249066 and 26420492 and the support received from the Joint Usage/Research Center for Interdisciplinary Large-scale Information Infrastructures and High performance Computing Infrastructure in Japan. I am also indebted to the Ministry of Higher Education (MOHE) for granting me sponsorships (SLAI) and to the Universiti Teknologi Malaysia (UTM) for approving my study leave. The Tokyo Tech's librarians also deserved special thanks for their assistance in supplying me with some relevant materials and data. I extend my sincere appreciation to all Kanda Lab's members especially to Dr. Alvin Christopher Galang Varquez and Miss Ayako Yagi, not to forget, Mrs. Yuko Okamoto for their supports and assistance since the beginning of this work. I am grateful to many Malaysian and international colleagues for their comments at different stages of this work. Finally, my gratitude is due to my parents and family members for their sacrifices, concerns and undying love.

ABSTRACT

The aim of this research is to quantitatively present a general relationship between the intensity of gust and the urban morphology. Two large eddy simulation (LES) models named as the parallelized LES model (PALM) and lattice Boltzmann model (LBM) were executed. It was confirmed that both models produce the same accuracy. The PALM was used to validate the new gust parameter while the LBM was applied to simulate and examine the gusts environment without uncertainties in the inflow condition. The coastal area of Tokyo was selected to represent the urban morphology. The simulations run over realistic geometry surfaces of the build up area with 2 m resolution in all direction to explicitly resolve the fine building shape and also the flow at the pedestrian level. It considers only the shear driven turbulence (i.e. no Coriolis force and thermal stratification) and developed the boundary layer naturally. A new parameter called the gust index (GI) was defined as the local maximum wind speed divided by the free stream velocity. This universalize definition make it comparable quantitatively at different locations within urban canopies. Moreover, this parameter is decomposed into mean wind ratio (MWR) and turbulent part ratio (TPR) component to evaluate the quality of gustiness. This procedure can mask detailed structures of individual buildings with keeping the bulk characteristics of the urban morphology. At the pedestrian level, it is quantitatively shown that the GI decrease with increasing building coverage, λ_p, which notably contribute by the TPR through out the range of λ_p compared to the MWR. Such a result was explained by the change of flow regimes within the building canyon. Apparently, at the higher elevation above the canopy layer, the effect of the building coverage becomes irrelevant to all normalized velocity ratios and the roughness length, as a comprehensive aerodynamic property of roughness was well represented.

SUMMARY (JAPANESE)

本論は「Large Eddy Simulation of the Gust Index over a Realistic Urban Area」（現実都市域におけるガスト指標のラージ・エディー・シミュレーション）と題して, 英文で書かれ, 以下の８章から構成される.

第 1 章「Introduction」(序論)では, おもに風工学分野と気象学分野で行われてき従来のガスト研究に関するレヴィユーを行い, ガストの定義方法, 歩行高さにおける平均風速などの旧来の成果について問題点・研究課題を提示し, 本論の動機・目的について論じている.

第 2 章「Description of an Appropriate Spatial Gust Index」(適切な空間ガスト指標について)では突風現象の定量評価のためのガスト指標（gust index）を提案した．従来の突風率（gust factor）は最大風速と局所的な時間平均値の比として定義され，街区の淀み域でも大きな値をとりうる．これに対し外層風速との比と定義することで，突風の強さを 1 次元的に評価することができる．これにより街区内での場所の比較のみならず，サイト間の比較なども可能となる.

第 3 章「Description of the simulation model」（シミュレーションモデルについて）では，本研究で使用した格子ボルツマン法 LES モデル及び, Navier-Stokes 方程式に基づく LES モデルの方程式系について記述した．また, 計算対象領域である東京都臨海部の建物分布について記した.

第 4 章「Validation」（モデル評価）では，格子ボルツマン法 LES のモデル性能評価を目的とし，風洞実験及び使用実績豊富な Navier-Stokes 式に基づく LES モデルとの比較を行い，両モデルがほぼ同程度の精度を持つこと

を明らかにした．また，ガスト指標の外力(外層風速)依存性について検討するため，実都市幾何形状を地表面に配した気流のシミュレーションを行い，大気境界層の現実的な外層風速の範囲内では，ガスト指標が外力に依存しないことを示した．

第 5 章「General description of the flow field within a realistic urban area」（現実都市域における流れの性質）では，基本的な乱流統計量の性質について記述した．風洞実験における粗面及び滑面の乱流境界層との比較を行った結果，地表面近傍では違いが出るものの，境界層高度の約半分以上では地表面性状に依らない乱流統計量の相似性が概ね成り立つことを示した．

第 6 章「Horizontal distribution of the flow field within a realistic urban area」（現実都市域における流れ場の水平分布構造）では，瞬間及び平均風速，レイノルズ応力の水平断面分布を描画し，地物の影響範囲について検討を行った．ガスト指標の空間分布を描画し，これについても地物との対応関係を視覚的に示した．

第 7 章「General relationship between the gust index and the urban morphology」（ガスト指標と都市幾何形状の普遍的な関係）では，ガスト指標と建物分布との関係性について議論した．計算領域を水平方向の小領域に分割し，その小領域の中でガスト指標の平均値及び，マクロな建物幾何パラメータ（平均建物高さや建蔽率）を算出し，比較した．これにより歩行者レベルのガスト指標が建蔽率に対してほぼ線形に減少することを明らかにした．また，その勾配がある建蔽率を境に大きく変わることが分かり，これは従来提案されている 2 次元建物キャノピーの流れ分類で説明できることを示した．

第 8 章「Concluding remarks」（結論）では本研究成果及び，現時点で未解決の点を記述した．

以上要するに，本論文は数値計算に基づく実都市の突風評価手法を提案するものであり，都市気象・都市計画分野で工学上高く評価される．よって，博士（工学）として価値が十分あるものと認められる．

TABLE OF CONTENTS

LIST OF FIGURES

LIST OF SYMBOLS

A	-	Area/Sample	m^2
C	-	Model coefficient	
c	-	Velocity vector	
dx	-	Grid length in *x*-direction	m
dy	-	Grid length in *y*-direction	m
dz	-	Grid length in *z*-direction	m
E	-	Magnitude of the velocity gradient tensor	
g	-	Gravitational force	$m\ s^{-2}$
k	-	Turbulence kinetic energy	$m^2\ s^{-2}$
k	-	Height of the roughness element	m
m	-	Gradient	
N	-	Grid resolution	
n	-	Total number of sample	
Q	-	Velocity gradient tensor	
q	-	Specific humidity	
t	-	Time	s
H	-	Cube/building height	m
U	-	Mean wind speed	$m\ s^{-1}$
$\widetilde{U}$	-	Mean wind ratio	
$\widetilde{U}_{max}$	-	Gust index	
$\widetilde{U}'$	-	Turbulent part ratio	
u	-	Wind velocity in streamwise (*x*-direction)	$m\ s^{-1}$
uw	-	Reynolds stress (mean component)	$m^2\ s^{-2}$
v	-	Wind velocity in spanwise (*y*-direction)	$m\ s^{-1}$
w	-	Wind velocity in vertical direction (*z*-direction)	$m\ s^{-1}$
X, x	-	Computation domain streamwise (*x*-direction)	m
Y, y	-	Computation domain spanwise (*y*-direction)	m

Z, z	-	Computation domain height (z-direction)	m
z_0	-	Roughness length	m
δ	-	Boundary layer height	m
ε	-	Turbulence dissipation	$m^2 s^{-3}$
λ	-	Area index	
Δ	-	Interval/width	
ν	-	Kinematic viscosity	$m^2 s^{-1}$
ω	-	Weighting factor	
ρ	-	Density	$kg\ m^3$
τ	-	Relaxation time	s
σ	-	Standard deviation	m
θ	-	Potential temperature	K
$[\ ]$	-	Values average in patch size	
$[\ ]_{bin}$	-	Values average in bin range	

Superscript/Subscript/Accent

ave	-	Average
b	-	Bulk
f	-	Frontal
i	-	i-th number of sample
ins	-	Instantaneous
loc	-	Local
max	-	Maximum
p	-	Plan
∞	-	Freestream
$*$	-	Friction
$'$	-	Turbulent
$\sim$	-	Ratio

$\bar{}$	-	Mean
1, 2, ...	-	Assigned number for the reference/point

Abbreviation

ABL	-	Atmospheric boundary layer
BGK	-	Bhatnagar-Gross-Krook
CAD	-	Computer-aided design
CFD	-	Computational fluid dynamics
CS	-	Coherent-structure
CSM	-	Coherent-structure Smagorinsky model
D3Q19	-	Three dimensional, 18 discrete velocities (plus one null)
GI	-	Gust index
GPU	-	Graphics processing units
GS	-	Grid scale
IMUK	-	Institute of Meteorology and Climatology
JMA	-	Japan Meteorological Agency
LBM	-	Lattice Botzmann method
LES	-	Large eddy simulation
MOST	-	Monin-Obukhov similarity theory
MWR	-	Mean wind ratio
NOAA	-	National Oceanic and Atmospheric Administration
PALM	-	Parallelized LES model
Q	-	Quarter
SGS	-	Subgrid-scale
TKE	-	Turbulent kinetic energy
TPR	-	Turbulent part ratio

LIST OF APPENDICES

LIST OF TABLES

CHAPTER 1

INTRODUCTION

1.1 Literature Review

1.1.1 General gusts definition

The National Oceanic and Atmospheric Administration (NOAA) defined the gusts as a sudden, brief increase wind speed above the average wind speed. Based on the U.S. weather observing practice, the wind speed is qualify as gusts when the maximum wind speed reaches at least 30 km h^{-1}, deviate between the peaks and calm condition at about 17 km h^{-1} and lasting for less than 20 s. The Editors of Encyclopaedia Britannica added that gusts cause by the turbulent flow around an obstacle which occur regularly over buildings and rough ground. From these definitions, gusts can generally describe as the disturbed air that blown in sudden, high speed and in a short period of time and it potentially gave an impact on its surrounding. In getting more clear understanding on the physical meaning of the strength of the blown wind, the Japan Meteorological Agency (JMA) categorized the wind speed and it effect towards the pedestrian, vegetation, moving car and the infrastructure as summarized in Table 1.1.

Table 1.1 The strength of the wind blow, translated from the Classification Table of the Rain and Wind leaflet, JMA (2014).

	Average wind speed (m s^{-1})	Approximate wind speed (km h^{-1})	Forecast terminology	Indication of speed	Pedestrian	Vegetation and utility	On road transportation	Building and infrastructure	Instantaneous wind speed (m s^{-1})
	10~15	~50	Somehow strong wind	On road transportation speed	It is difficult to walk against the wind.	Whole trees and wires begin to sway.	Feel the crosswind if the the transport in the high speed and the wind stream perpendicular to it.	The antenna begins to sway.	20
	15~20	~70	Strong wind		Walk against the wind will cause fall. Work at high level is extremely dangerous.	Wire, signboards and galvanized iron plate begins to flutter.	During the high-speed operation, the driver can sense the increase in the crosswind.	The roof, tiles, roofing material peeled off. Shutters start to shake.	30
	20~25	~90	Very strong wind	Highway transportation speed	Need to hold on to something to stand. Fear to be injured by the flying objects.	Broken tree or thin trunk and trees that do not have a strong roots grip begin to collapse. Signboards fall and scattered. Road signs tilt.	It becomes difficult to drive at a normal speed.	The roof, tiles, roofing material scattered.	
	25~30	~110							40
	30~35	~125	Severe wind	Express train	Outdoor condition is very dangerous.		The wind able to rollover a moving truck.	Inadequate metal roof or temporary scaffolding starts to collapse.	50
	35~40	~140				Many of the trees, poles and street lights fall. Block wall collapsed.		Exterior materials are scattered over a wide range, which exposed the base material.	
	40~	140~						May collapse a living house. May cause deformed in the steel structure.	60

Wind advisory High wind warning Extreme wind warning

The JMA averaged the wind speed within 10 min, while the instantaneous wind speed duration is of 3 s. Referring to Table 1.1, the instantaneous wind speed is about 1.5 times the average wind speed. The wind was measured based on the unstable atmospheric conditions. The wind speed phenomenon at a certain location and its consequence damage as described in the table may significantly differ from the nearby observation measurement due to the terrain and surrounding buildings. Although the wind speed is the same, the state of damage is different depending on the blowing way of the wind and the structure affected.

Gusts term might easily misunderstood as this phenomenon dependence on many factor such as its scale, source, location of occurrence, etc. Therefore, gusts were reviewed in several sections in this chapter as following.

1.1.2 Urban surface geometry and wind environment at the pedestrian level

It is vital to understand the wind flows close to the ground in densely built up areas because most activities of the residents occur at this level. Anomalous and unpredictable gusts may occur when wind flows through the maze created by a rugged urban landscape. Pedestrians and infrastructure may be harmed from such gusts, including injuries, death, damage, destruction of urban vegetation, power outages and traffic collisions as illustrated in Fig. 1.1. These negative impacts of gusts have encouraged the comprehensive study of the complex flows found within large urban areas and attempts to determine their relationships with the urban morphology.

This research empirically relate gusts at the pedestrian level with “bulk” geometrical parameters at the district or city scale, thereby identifying high-risk areas for gusts in terms of various urban morphologies.

Figure 1.1 Gusts in an urban area, illustration taken from the Classification Table of the Rain and Wind leaflet, JMA (2014).

1.1.3 Mean wind velocity ratio at the pedestrian level

The flow environment should be evaluated in terms not only of the gusty flow but also of the mean flow. In addition, since the concept to analyse the mean wind environment is useful also for analysing the gusty flow, the conventional studies on the mean wind ratio are reviewed.

Some studies have attempted to predict spatially averaged mean velocity profiles within urban canopies using simple models (Macdonald 2000; Martilli et al. 2002; Coceal and Belcher 2004). Although these models are very useful for approximately determining the mean wind profile within the canopy layer, they cannot precisely predict the mean wind velocity close to the ground, as demonstrated by a direct numerical simulation (Leonardi and Castro 2010). Moreover, these models are mostly validated for homogeneous building arrays rather than more realistic complicated building arrangements.

Some studies have examined the wind environment in cities at the pedestrian level in terms of the mean wind ratio (MWR), which is defined as the mean wind

speed (U) normalised by the free stream velocity (U_∞). Kubota et al. (2008) conducted a wind tunnel test using scaled models of selected detached and apartment houses from real cities in Japan. They reported that the MWR decreases in areas with higher plan area index (λ_p) values. Hu and Yoshie (2013) used a computational fluid dynamics (CFDs) turbulence model as a reference urban model of a typical residential area in Shanghai, and found that the MWR was affected not only by λ_p but also by the configuration of roughness in urban areas, variation in the heights of buildings, and wind direction. A large eddy simulation (LES) by Razak et al. (2013) for simplified but varied building arrays demonstrated a robust relationship in which the MWR decreased with an increase in the frontal area index (λ_f). Taken together, these studies suggest the possibility that the MWR can be explained by simple geometrical indices such as λ_p and λ_f.

In this research, the similar approach was followed for the gusts. In addition, the MWR in the urban area is also evaluated.

1.1.4 Gusts at the pedestrian level

Researchers in the fields of wind engineering and architectural engineering have investigated gusts at the pedestrian level. The main focus has been on detailed and local flow structures around a single building or specific building clusters rather than on the overall relationship between gusts and bulk geometrical parameters at the district or city scale. Murakami et al. (1983) conducted a long-term observation of gusts around a single high-rise building and its surroundings near the surface. The large amount of data collected was analysed to make a detailed estimate of the local gust factor distribution around buildings. He and Song (1999) performed an LES to simulate the wind flow at 2 m above the ground around a group of buildings with different geometries. The gusts associated with different wind conditions were visualised in detail.

Recent developments in computational resources have allowed computations of town-scale urban airflows at high spatial resolution. Some studies have examined the effects of not only individual buildings but also groups of buildings on street-level flows. These studies conducted simulations of turbulent flow in and above cubical roughness, and revealed that turbulent organized structures are much larger than surface obstacles (Kanda et al. 2004; Kanda 2006; Castillo et al. 2011). Moreover, Inagaki et al. (2012) demonstrated that such turbulent structures predominantly determine the instantaneous flow distribution within the canopy layer. Park et al. (2013) simulated turbulent flow in an actual city with a 5 m domain resolution, and observed a tail-off in the coherent turbulent structure induced by significantly tall buildings at a great distance downstream. However, it has proven difficult to obtain a general and quantitative description of gusts at the pedestrian level and to understand their relationships with the urban morphology. This is probably due to the complexity of the building morphology, together with the three-dimensionality and intermittent nature of turbulence.

1.1.5 General meteorological studies of gusts

Most gust studies have been conducted within the framework of conventional meteorology, including the definition of gusts, the time required to define the average and/or maximum wind velocity, the statistical features of gusts, and the influential meteorological parameters of gusts (e.g., surface roughness, observation height, atmospheric stability, etc.). Such studies have not focused on the pedestrian level but rather on the surface layer based on Monin-Obukhov Similarity Theory (MOST) (Monahan and Armendariz 1971; Wieringa 1973; Wilson 2000; Verkaik 2000; Azad and Alam 2010).

The gustiness that summarized in Table 1.2, is the normalized values of the maximum wind speed by the mean wind speed. The averaging time for the mean wind speed and the interval of the maximum wind speed varies between each investigator. The factors will be lower as the maximum wind speed duration is shorter and/or the greater the mean wind speed averaging time. In term of different in

the measurement height (not shown in the table), Davis and Newstein (1968) suggested that the gust factor should decrease with height by referring the assembled data from many investigators.

Table 1.2 Summary of gust factors, Davis and Newstein (1968).

Investigator	Range of gust factor	Time average of mean wind speed	Duration of maximum wind speed
Brekker (1959)	1.30-1.08	varies	-
Cramer (1960)	1.62-1.38	10 min	instantaneous
Deese (1964)	2.00-1.20	5 min	instantaneous
Durst (1960)	1.59-1.00	1 h	1 h to 0.5 s
Faber and Bell (1963)	2.05-1.28	1 h	Instantaneous to 1 min
Shellard (1965)	1.90-1.30	10 min	3-5 s
Vellozzi and Cohen (1967)	1.56	1 h	1 s

Due to the locality of the urban area, several parameters especially the mean wind speed change by points and locations mainly wind flow at the pedestrian level. Therefore, this conventional approach needs to be modified to make it universal and comparable with other locations or even experiments.

1.2 Background of the Research Problem

A vigorous and populous urban landscape might be vulnerable in the unpleasant wind event such as a strong gust. As a consequence of this fact, it is essential to understand the features of the wind flow within this area particularly at the pedestrian level. As reviewed above, there are so many studies related to the wind flow and/or gust at different scale. The micro- and local-scale studies might focus on the pedestrian level which consider only a single building (Murakami et al. 1983), a cluster of real building (He and Song 1999), simplified urban model (Hu and Yoshie 2013, Razak et al. 2013, Inagaki et al. 2012) or even the real urban area (Kubota et al. 2008, Park et al. 2013). It is capable to map the spatial distributions of

the wind statistics for these studies. For a bigger scale (i.e., meso-scale), the wind and/gust measured at a surface layer level at a certain location (i.e., point measurement).

It is discovered that there is lacking in understanding the gust that occur in an acceptable huge area horizontally which comprise a realistic urban roughness. Moreover, the relationship between the flow characteristics in the surface layer and those at the pedestrian level (Sect. 7.5 of Chapter 7) are not reveal yet by the previous researcher. Thus, it is suggested that there are some gaps between the results from studies undertaken in the two disciplines in which gusts are commonly studied: wind engineering (Sect. 1.1.4) and meteorology (Sect. 1.1.5).

1.3 Objective and Importance of the Study

Although the researches on gusts are many, those matching the purpose of this research are rare as reviewed in the previous sections.

Thus, this research is important to reveal the wind flow characteristics specifically the gusts within this build up area and determine a general similarity and description that can associate the different scale or level as mentioned before. It can be done by assigning an appropriate definition for the related parameter.

Furthermore, this research was highly motivated by a simulation of the wind flow over a huge urban area performed by Onodera et al. (2013). Therefore, it is feasible to achieve the final goal of this study which is to quantitatively analyse the relationship between the gust at the urban pedestrian levels and the building morphology.

1.4 Scopes of the Study

The ultimate objective of this study was achieved by coordinating the research framework as shown in Fig. 1.2. This structured workflow is elaborated in the sequential chapters. The basic understanding on gusts is reviewed in the previous section of this chapter. The conventional gust factor and proposed spatial gust index are defined in Chapter 2. Next, Chapter 3 describes the large eddy simulation (LES) models which executed mainly to resolve the instantaneous wind speed and other wind flow elements within a realistic city. The preliminary study contributes in defining an appropriate spatial gust index performed by parallelized LES model (PALM). Subsequently, the lattice Boltzmann method (LBM) was conducted to reach the main purpose of this research. Both LES models were validated and demonstrated in Chapter 4. In stead of that, the gust index defined in Chapter 2 is also justified in this chapter. Following, Chapter 5 and 6 presents the general description of the flow field by the wind profile (in the streamwise and vertical direction and the related geometrical parameters) and horizontal distribution (including the spatial gust index map) respectively; focusing on the statistics computed from the LBM simulation. The foremost part of this research as priory mentioned (Sect. 1.2) contributes in Chapter 7. Finally, the concluding remarks and several recommendations for future work are stated in Chapter 8.

1.5 Summary

In a nutshell, this chapter introduced and reviewed the wind environment in the urban area specifically the gust at the pedestrian level. A clear objective in finding the general relation between the gust index and the urban morphology empirically was stated. The general overview of the research was also described for the following chapters. It is expected that this study will contributes some knowledge about the gust in an urban area and also filling some gap between the two streams of the gust studies which are the wind engineering and the meteorology.

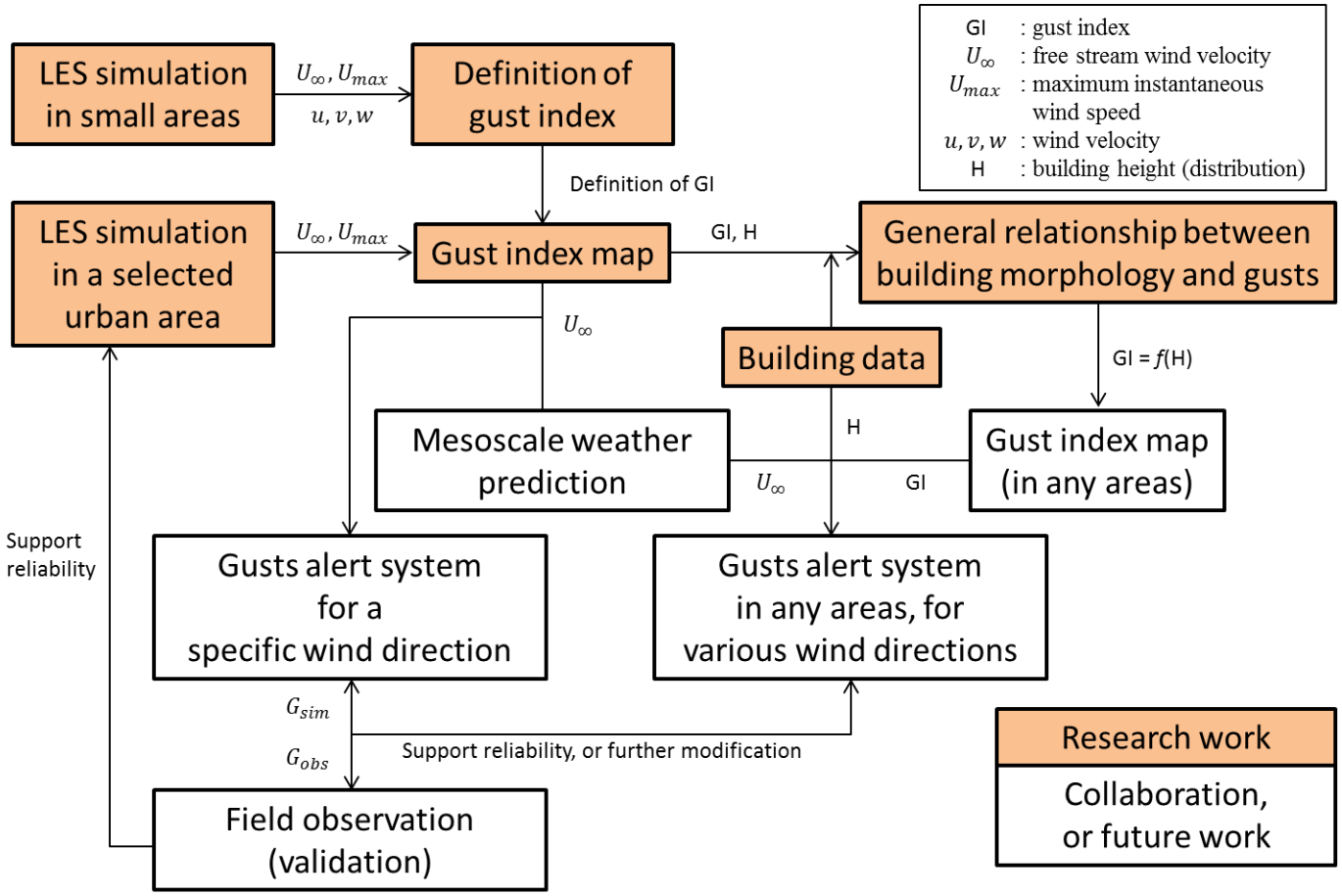

Figure 1.2 Research flowchart.

CHAPTER 2

DEFINING AN APPROPRIATE SPATIAL GUST INDEX

2.1 Introduction

This chapter will introduce a new dimensionless, spatial indicator for gusts known as the gust index. Briefly, this index is the ratio of the maximum instantaneous wind speed to the free stream velocity at a chosen height. Priory, an established conventional gust factor will be described. Some constraint from this conventional gust factor initiate in defining the gust index. Moreover, the gust index decomposed into its components which known as the mean wind ratio and the turbulent part ratio to get more comprehensive insight.

2.2 The Spatial Gust Index

Conventionally, the gust factor, G, which assess the relative importance of the turbulent component to the mean velocity is defined as in Eq. 2.1;

$$G = \frac{U_{max}}{U}, \tag{2.1}$$

where U_{max} is the instantaneous maximum wind speed over a period of time and U is the mean wind speed of a certain averaging time. The gust factor is locally defining variable because U_{max} and U are measured at a certain location. A more general discussion is enabled by extrapolating the mean wind speed to the level of 10 m by assuming the log-law or Monin-Obukhov similarity (He and Song 1999). An averaging time of 10 min has been conventionally used for the same reason. The use of this parameter has had some success in the modelling of the gust factor in flat fields based on a similarity framework (Monahan and Armendariz 1971; Wieringa 1973; Wilson 2000; Verkaik 2000; Azad and Alam 2010). It is difficult to use this parameter when comparing results among different locations in an urban canopy because not only U_{max} but also U changes from point to point due to the disturbance from surrounding buildings. This can cause an infinitely large G in stagnation points, irrespective of the magnitude of U_{max}.

Therefore, a new definition of the gustiness level is proposed because the established gust factor has a different practical purposed. For this, the GI applied in this study calculated as follows:

$$\widetilde{U}_{max} = \frac{U_{max}}{U_{\infty}}, \tag{2.2}$$

where the instantaneous maximum wind speed is normalised to the free stream velocity U_{∞} instead of the local mean wind speed used in Eq. 2.1. This definition is suitable for the research purpose of examining and comparing the intensity of gusts in different areas of the same simulation domain, or even in different experiments.

Although this definition is only applicable for numerical simulations or indoor experiments, it is still useful for obtaining the general relationship between the intensity of gusts and building morphology. In the real atmosphere, geostrophic wind could be used instead of the free stream velocity.

2.3 The Gust Index and its Component

For further insight into gust characteristics, the maximum instantaneous wind speed was decomposed into a mean wind speed (U) and the turbulent part (U') using Eq. 2.3 below:

$$U_{max} = U + U'. \tag{2.3}$$

The MWR was obtained by normalizing the local mean wind speed by the free stream velocity as follows:

$$\widetilde{U} = \frac{U}{U_{\infty}}. \tag{2.4}$$

Following the same procedure as the GI and MWR, the turbulent part ratio (TPR) was defined as follows:

$$\widetilde{U}' = \frac{U'}{U_{\infty}} = \frac{U_{max} - U}{U_{\infty}}. \tag{2.5}$$

The MWR has been used to analyse the mean wind distribution within an urban canopy to determine the relationship with the urban building morphology (Kubota et al. 2008: Keck et al. 2014). TPR is a new parameter that expresses the contribution of the turbulent fluctuation in gusty wind. Although this parameter has similar characteristics to the standard deviation of velocity fluctuation which has

conventionally been analysed, it can directly show the relative contributions of the MWR and TPR in observed gust events.

It should be noted that this newly defined GI with Eqs. 2.2 to 2.5 can readily provide the conventional gust factor.

2.4 Summary

This brief chapter presented the definition of the gust index and its components (i.e.; mean wind ratio and turbulent part ratio) applied in this research. The ratio between the maximum instantaneous wind speeds to the free stream velocity applied. While the conventional gust factor normalised by the local mean wind speed. This locality characteristic of the gust factor leads to misinterpret the gusts intensity at different locations. Thus, the proposed gust index is comprehensible enough to express the gusts spatially. Moreover, the gust index component which is the mean wind ratio can describe mean wind distribution. While, the turbulent part ratio articulates the contribution of the turbulent fluctuation.

CHAPTER 3

DESCRIPTION OF THE SIMULATION MODEL

3.1 Introduction

This chapter will explain the models used to simulate the wind flow within an urban area. There are two different large eddy simulation (LES) models used. The first LES model known as the parallelized large eddy model (PALM) which used as a preliminary study of the gust in an urban area and find out the most suitable gust index definition. In the second stage, the other simulation which applied the LES model combined with the lattice Boltzmann method (LBM) was executed on a realistic urban area and 100 times larger domain than the one simulated in the PALM. This simulation used to fulfil the main objective of this study which is to find the general relationship between the gust index and the urban morphology. Each of the models mentioned will be described further.

3.2 Parallelized Large Eddy Simulation Model

3.2.1 Model description

The parallelized large eddy simulation model (PALM) has been developed and maintained by Raasch and Schröter (2001) from Institute of Meteorology and Climatology (IMUK) of Leibniz Universität Hannover, Germany. This open source simulation model software was widely used around the world such as United States, Brazil, China, Korea, Japan and etc. The model is used to simulate the atmospheric and oceanic flows. Thus, the urban atmospheric boundary layer (ABL) is simulated in this study.

PALM is a finite difference model which computes the approximated Navier-Stokes equations of the non-hydrostatic and incompressible Boussinesq, the first law of thermodynamics and the subgrid-scale (SGS) turbulent kinetic energy (TKE) equations. These governing equations separate the eddy by its scale and filtered implicitly with the Schumann volume-balance approach. The numerical grid discretize the equations spatially which based on the marker-and-cell method (Arakawa C grid). The third-order Runge–Kutta method (leapfrog scheme) is used for the time integration. The advection is solves by the second order central finite differences by Piacsek–Williams. The smaller than grid scale turbulence is parameterize by the SGS model which based on the modified Smagorinsky model and applied the one-and-a-half-order Deardorff subgrid closure scheme.

The final set of PALM equations is shown below:

Navier-Stokes equations

$$\frac{\partial \overline{u_\iota}}{\partial t} = -\frac{\partial \overline{u_k}\,\overline{u_\iota}}{\partial x_k} - \frac{1}{\rho_0}\frac{\partial \bar{\pi}^*}{\partial x_i} - \varepsilon_{ijk} f_j \overline{u_k} + \varepsilon_{i3k} f_3 \bar{u}_{k_g} + g\frac{\bar{\theta} - \theta_0}{\theta_0}\delta_{i3} + \nu\frac{\partial^2 \overline{u_\iota}}{\partial x_k^2} - \frac{\partial \tau_{ki}^r}{\partial x_k} \qquad (3.1)$$

First principle (using potential temperature)

$$\frac{\partial \bar{\theta}}{\partial t} = -\frac{\partial \overline{u_k}\bar{\theta}}{\partial x_k} - \frac{\partial H_k}{\partial x_k} + Q_\theta \tag{3.2}$$

Equation for specific humidity (passive scalar)

$$\frac{\partial \bar{q}}{\partial t} = -\frac{\partial \overline{u_k}\bar{q}}{\partial x_k} - \frac{\partial W_k}{\partial x_k} + Q_w \tag{3.3}$$

Continuity equation

$$\frac{\partial \overline{u_k}}{\partial x_k} = 0 \tag{3.4}$$

Normal stresses include in the stress tensor are now included in a modified dynamic pressure

$$\begin{aligned} \tau_{ki}^r &= \tau_{ki} - \frac{1}{3}\tau_{jj}\delta_{ki} \\ \bar{\pi}^* &= \bar{p}^* + \frac{1}{3}\tau_{jj}\delta_{ki} \end{aligned} \tag{3.5}$$

Subgrid-scale (SGS) stresses (fluxes) to be parameterized in the SGS model

$$\begin{aligned} \tau_{ki} &= \overline{u_k u_\iota} - \overline{u_k}\,\overline{u_\iota} \\ H_k &= \overline{u_k \theta} - \overline{u_k}\bar{\theta} \\ W_k &= \overline{u_k q} - \overline{u_k}\bar{q} \end{aligned} \tag{3.6}$$

More details about PALM can be access via the online documentations which provided by the developer (https://palm.muk.uni-hannover.de).

Parallelization of the large eddy simulation (LES) model means that a different set of data were resolved by the same program code which carried out by the massively parallel occupied processor elements. Instead of that, PALM is also capable to be performed on shared memory computer.

There are many studies of the wind flow in an urban area by executing the set of governing equations from PALM such as Inagaki et al. (2012), Letzel et al. (2012), Kanda et al. (2013), Keck et al. (2014) and Park et al. (2015). Referring to those published work, PALM used in this study to simulate the gust over an urban area.

3.2.2 Simulation setup

The numerical domain explicitly resolves the decomposed 2 m resolution of the real urban morphologies that acquired from 3D Map Data (MAPCUBE) provided by the CAD Center. Ground topography is not considered (i.e.; flat ground). The wind simulated over an equally spaced domain of 1,000 m × 1,000 m foot print and 600 m height (500 × 500 × 300 grids) induced the shear driven turbulent flow (i.e.; no heat flux). The wind flows from the left to the right of each domain of Fig. 3.1. The domains differ by its classification of the urban surfaces namely as the commercial land, skyscrapers area and residential area.

The lateral boundary conditions of the model are cyclic and non-slip for all building and ground surfaces. While, the free-slip conditions was applied at the domain top. The rough wall function prescribed a Prandtl layer for each wall surface was based on Monin–Obukhov similarity theory. The different initial turbulent inflows were set at 3 m s^{-1}, 6 m s^{-1} and 12 m s^{-1} directed along the *x*-axis. The simulation time was last for 3 hours.

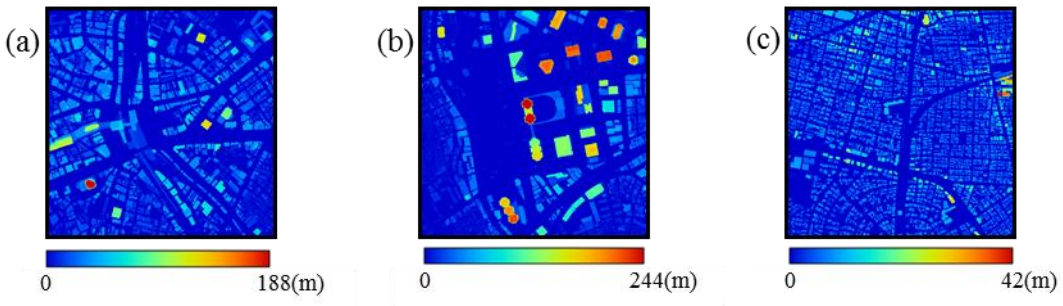

Figure 3.1 Building height distribution of the (a) commercial land (b) skyscrapers (c) residential area.

3.3 Lattice Boltzmann Method and Large Eddy Simulation

3.3.1 Model description

A CFD code based on the LBM has been developed to execute large-scale wind simulations over a 10 × 10 km domain of an urban area in Tokyo, with 1 m resolution (Onodera et al. 2013). A stable calculation of turbulent flows with a very high Reynolds number is possible by applying an LES to the LBM (Hou et al. 1994; Yu et al. 2005). A subgrid scale (SGS) model that implies a coherent-structure Smagorinsky model (CSM) enables local determination of the model parameter (Kobayashi and Wu 2006). This approach provides an efficient, fast and parallel computation for a large-scale simulation with a very fine resolution that is also geometrically complex (Kobayashi et al. 2008; Bernaschi et al. 2010; Onodera et al. 2013). In this study, the same model as that used by Onodera et al. (2013) was used to simulate a developing urban boundary layer under neutral stratification. A detailed description of this model has been provided by Onodera et al. (2013).

The LBM is based on a discrete equation derived from the Boltzmann equation. It treats flow as a limited number of pseudo-particles in a streaming and collision process. Because the physical space is discretised by a uniform grid, particles move into the neighbouring grid points after one time step. Discrete velocities are expressed by the D3Q19 model (Bernaschi et al. 2010; Onodera et al. 2013) which shown in Fig. 3.2. The bulk velocity is calculated by integrating the velocity distribution function in a volume. The collisions of a mass of particles are modelled by the Bhatnagar-Gross-Krook (BGK) model (Zou and He 1996; Onodera et al. 2013). This provides an advantage over the continuity in the Navier-Stokes equation.

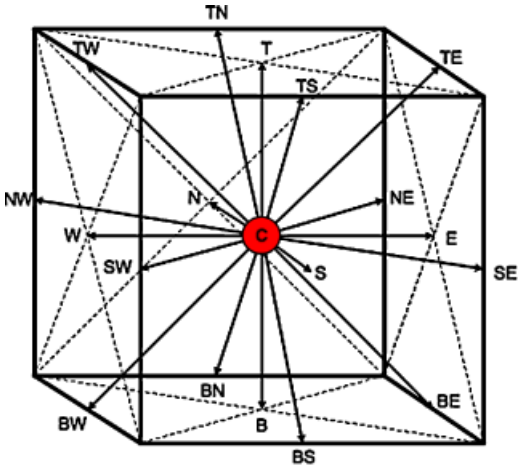

Figure 3.2 The arrows represent the directions of the fluid populations (i.e., a set of 18 discrete velocities including one null vector corresponding to particles at rest) according to the D3Q19 scheme Bernaschi et al. (2010).

Listed are the functions contained in this model (Onodera et al. 2013). The time evolution of the discretized velocity function is

$$f_i(x+c_i\Delta t,\, t+\Delta t) = f_i(x,\, t) - \frac{1}{\tau}\left(f_i(x,\, t) - f_i^{eq}(x,\, t)\right) + F_i(x,\, t) \tag{3.7}$$

where Δt is the time interval and $f_i^{eq}(x,\, t)$ is the local equilibrium distribution at the time t and position x as below.

$$f_i^{eq} = \omega_i \rho \left(1 + \frac{3c_i.u}{c^2} + \frac{9(c_i.u)^2}{2c^4} - \frac{3u^2}{2c^2}\right) \tag{3.8}$$

and here ρ is the density and u is the macroscopic velocity. The relaxation time, τ is determined using the kinematic viscosity as in Eq. 3.9,

$$\tau = \frac{1}{2} + \frac{3\nu}{c^2\Delta t} \tag{3.9}$$

The components of the 19 velocity vectors c_i in three dimensions of the D3Q19 model is as below,

$$c_i = \begin{cases} (0,0,0) & & & i = 0, \\ (\pm c, 0,0), & (0, \pm c, 0), & (0,0, \pm c) & i = 1-6, \\ (\pm c, \pm c, 0), & (\pm c, 0, \pm c), & (0, \pm c, \pm c) & i = 7-18, \end{cases} \tag{3.10}$$

and the corresponding weighting factors are,

$$\omega_i = \begin{cases} 1/3 & i = 0, \\ 1/18 & i = 1-6, \\ 1/36 & i = 7-18. \end{cases} \tag{3.11}$$

The LES resolved the flow dynamics of large-scale structures on a grid scale (GS). An SGS model considers the effects of smaller-scale turbulent structures, and is based on the concept of eddy viscosity. In the Navier-Stokes equation, LES modelling is implemented in the turbulent diffusion term by introducing an SGS-eddy viscosity. In the LBM, SGS modelling is accomplished in a collision term using eddy viscosity, which has the same form as is modelled in the Navier-Stokes equation.

$$\nu_{SGS} = C\bar{\Delta}^2|\bar{S}| \tag{3.12}$$

where C is the model coefficient, $\bar{\Delta}$ is the filter width and $|\bar{S}|$ is the magnitude of the velocity strain tensor.

As this simulation is designed for a large scale and encloses a realistic and complex urban area, the CSM can be applied (Kobayashi et al. 2008). The CSM models the small-scale turbulent diffusion using the second invariant of a velocity gradient tensor. This model is suitable for parallel computing without an averaging process because the model parameter is calculated using locally-defined variables only.

The model coefficient C_{CSM} is calculated by treating the coherent structure F_{CS} as a function of the velocity gradient tensor Q and its magnitude E. The formula for the stated parameters listed as in Eq. 3.13.

$$\begin{gathered} C_{CSM} = C'|F_{CS}|^{3/2} \\ F_{CS} = \frac{Q}{E}(-1 \le F_{CS} \le 1) \\ Q = -\frac{1}{2}\frac{\partial \bar{u}_j}{\partial \bar{x}_i}\frac{\partial \bar{u}_i}{\partial \bar{x}_j}, E = \frac{1}{2}\left(\frac{\partial \bar{u}_j}{\partial \bar{x}_i}\right)^2 \end{gathered} \tag{3.13}$$

The coefficient $C' = 1/20$ is a fix model parameter and it is optimized for a wide range simulations.

3.3.2 Simulation setup

It is likely that gusts are affected by the buildings in the upwind direction. Thus, the gust distribution in a developing boundary layer from the coastal edge of the buildings was examined using a numerical simulation. Part of a coastal area in Tokyo was chosen for the simulation as shown in Fig. 3.3 and 3.4. In this setting, a large computational domain along the streamwise direction was required to develop a boundary layer high enough to obtain robust statistics within an urban canopy that was free from the boundary layer height. Therefore, a large domain size (19.2 km streamwise [X], 4.8 km spanwise [Y] and 1 km vertical direction [Z]) was used. A fine grid resolution of 2 m in all directions was used to explicitly resolve the individual building shapes and also the flow at the pedestrian level. This provided a 9600 × 2400 × 500 mesh for this computational domain. A realistic building geometry in a coastal area of Tokyo was implemented in the geometry of the ground morphology without the topographical elevation. Other than the building geometry, this model did not consider any difference in the solid surface conditions. Part of Tokyo Bay was included, which extended to a few kilometres from the inlet, and was expressed as a flat surface without any buildings.

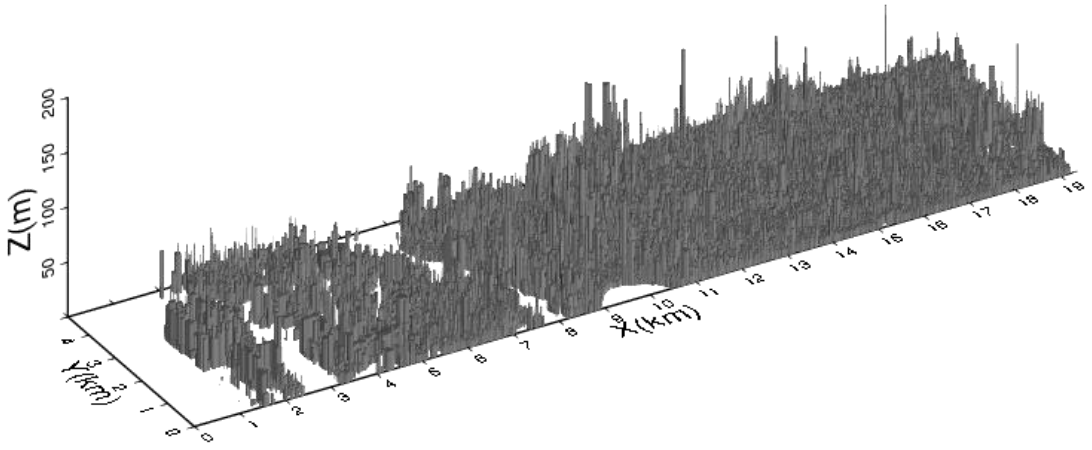

Figure 3.3 Three dimensional scaled view of the building height data.

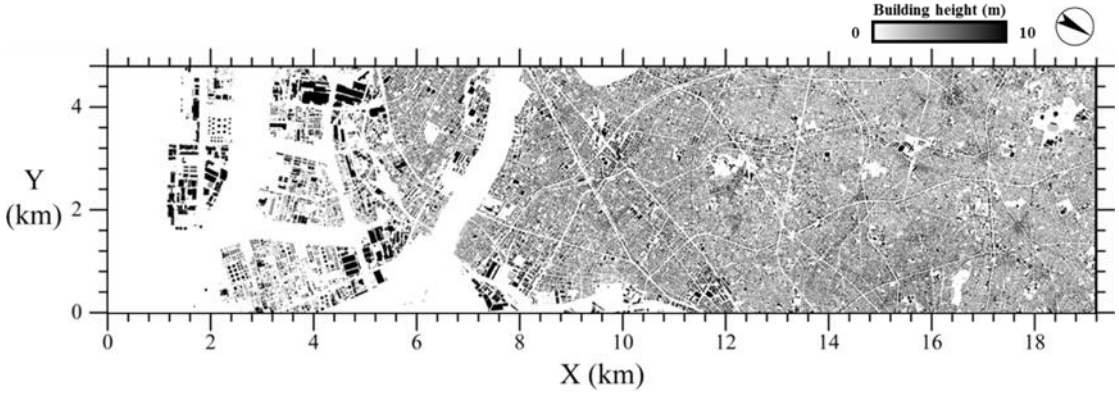

Figure 3.4 Building height within a 19.2 km (X) × 4.8 km (Y) × 1 km (Z) simulation domain of an urban area of Tokyo.

For the boundary conditions, a continuous bulk uniform inflow of 10 m s^{-1} was applied at the domain inlet. The flow blew from the coastal area toward the inland urban area. The outlet boundary applied the radiation condition. A spanwise periodic boundary condition was used in the domain. A no-slip boundary condition was imposed on a solid surface. The bounce-back scheme makes it easy to implement the no-slip velocity condition with complex shapes. In the bounce-back rule, a particle that collides with a stationary wall will be reflected in the opposite direction of its velocity and returned to its original location (He et al. 1997; Yin and Zhang 2012; Onodera et al. 2013). The top of the domain is treated the same as the condition of the grid next to the bottom wall where the slip velocity can be resolved (He et al. 1997). Moreover, the artificial wave due to a very sensitive simulation output at the domain top boundary was damped. This deficit also encountered by

setting an appropriate simulation domain height. The thermal stratification and the Coriolis force are not considered in this simulation, which considers only the shear driven turbulence.

The simulation time was 4320 s and the computation was performed by the 900 graphics processing units (GPUs) of a supercomputer facility (TSUBAME 2.5). It needs a very small time step which is 0.008 s due to the instability in resolving the discrete equation of the lattice Boltzmann equation. The final 600 s was used for the analysis when the boundary layer had already reached a quasi-steady state. The simulation finished within 40 h, due to the numerical algorithm of the LBM, using massively parallel GPU computing in the supercomputer system. The model had the same accuracy as that reported by Castillo et al. (2011) (data not shown).

3.4 Summary

As a conclusion, there are two main large eddy simulations (LES) model used in this study. The first model which is parallelized large eddy simulation model (PALM) performed mainly to find out the suitable gust index definition. In fulfilling the final goal of this study, the simulation was conducted over a huge domain by executing the large eddy simulation that applied the lattice Boltzmann method (LBM). The discretized equation derived from the Boltzmann equation provides an advantage over the continuity in the Navier-Stokes equation. Thus, the LBM approach provides an efficient, fast and parallel computation for a large-scale simulation with a very fine resolution and geometrically complex. However, each of the simulation models contributed a great role in the research outcomes. Concisely, a general relationship between the gust index and the urban morphology can be revealed from the simulations output.

CHAPTER 4

VALIDATION

4.1 Introduction

Extending from the previous chapter, the simulation models (i.e.; the lattice Boltzmann method (LBM) and the parallelized LES model (PALM)) executed in this research will be validated with an established wind tunnel test results to confirm their performances. In the second part, the probability distribution function use to justify the most appropriate description to represent the spatial gust index. The outputs from PALM provide several denominator candidates to be tested in defining the new gust index. Both, the simulation models and the new gust index were the foremost elements in generalising the relationship between the gusts event and the urban morphology.

4.2 Simulation Models Inter-comparison

In the first stage, the accuracy of the parallelized large eddy simulation model (PALM) compared with the wind tunnel test results from Martinuzzi and Tropea (1993). This validation was also done by Letzel et al. (2008). Then, the PALM numerical model verified with the large eddy simulation (LES) that performed with the lattice Boltzmann method (LBM).

The airflow around an isolated cube as shown in Fig. 4.1 performed for both numerical methods as was done before in the wind tunnel experiment. Moreover, PALM was an established model for the atmospheric boundary layer study on the flat and the real city as listed in sect. 3.2.1.

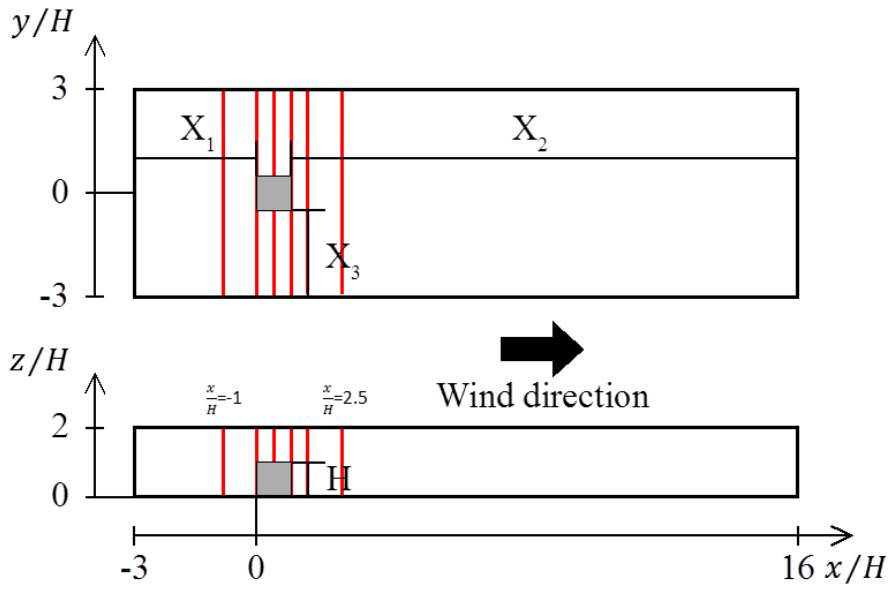

Figure 4.1 Domain setting for the validation simulation. Red lines show each measurement location (x/H = -1, 0, 0.5, 1, 1.5, 2.5).

Figure 4.2 shows the vertical distribution of the average wind speed ratio between the main flow, U and the inflow, U_b obtained from the simulation results. The profiles shown was plotted for several locations (i.e.; before, in the middle and after the cube). A number of different grid resolution, N, applied in the simulation. The profiles show a good agreement with the experimental results as the grid resolution increased.

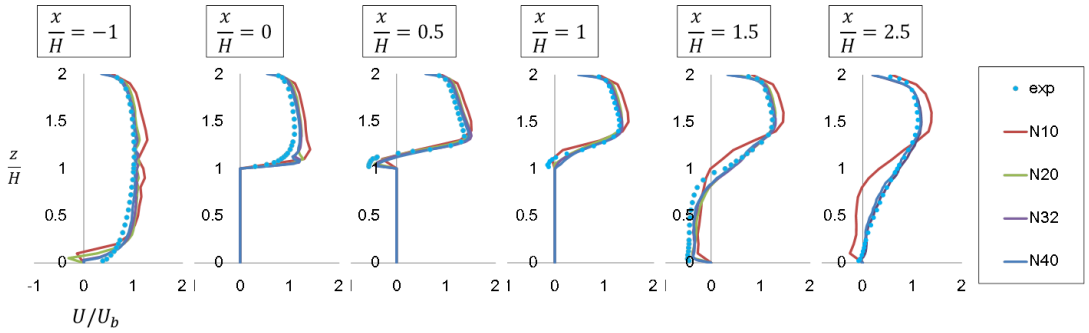

Figure 4.2 Vertical profile of the average wind speed, U, normalized to the bulk inflow cross-section average wind speed, U_b. Experiment data shown by the dotted line. Each profile represents the position mentioned in Fig. 4.1.

The vertical (cube centre) and horizontal (bottom layer) cross-sections of the time averaged streamline shown in Fig. 4.3. Focusing to the vertical cross-section of the N = 32 case, the swirling flow line near the bottom of the cube downwind side can be seen. Such streamline is not reproduced in the coarser spatial resolution. However, the streamlines for the horizontal cross-section does not show an essential difference although the domain resolution changed.

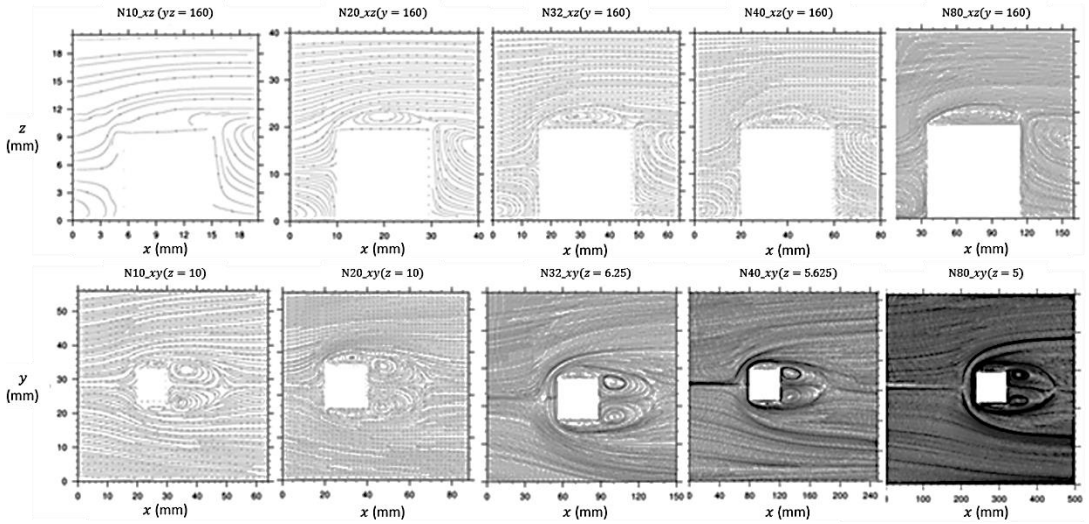

Figure 4.3 The streamlines around the cube centre vertical cross-section and lowermost horizontal cross-sectional. N is the number of grids to resolve the cube piece.

The vertical profile of U/U_b compute from PALM and LBM-LES compared as in Fig. 4.4. Different resolution, i.e. N = 16, 32 and 64, set-up for both simulations. PALM and LBM-LES profiles fit well when N = 64 for all location measured. However, the domain resolution of an actual simulation conducted for this research was fixed to 2 m (~N = 32) and homogeneous in all direction for an economical computation in term of time and cost.

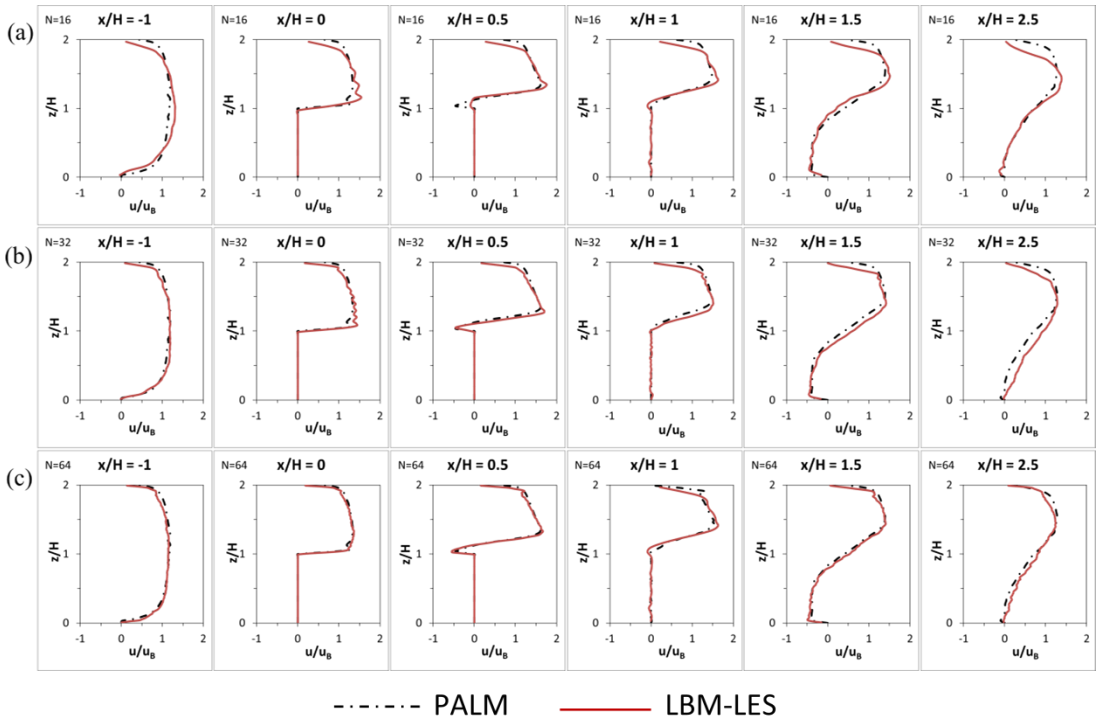

Figure 4.4 Comparison between the PALM and LBM-LES vertical profile of U/U_b. Domain resolution of (a) 3 m (N =16), (b) 1.5 m (N =32) and (c) 0.75 m (N =64) is homogeneous in all direction (*dx*=*dy*=*dz*).

4.3 Justification of the Gust Index Definition

The instantaneous maximum wind speed distribution U_{max} was plotted as shown in Fig. 4.5. Several denominators namely the spatial averaged wind speed, U_{ave}, friction velocity U^*, local wind speed, U_{loc}, freestream velocity, U_∞, at certain reference level, used to normalize the U_{max} and define the spatial gust index (GI) (Huda et al. 2014; Huda et al. 2015). All the wind speeds measured at 2 m height except for the U_∞ (i.e.; at 600 m or domain top).

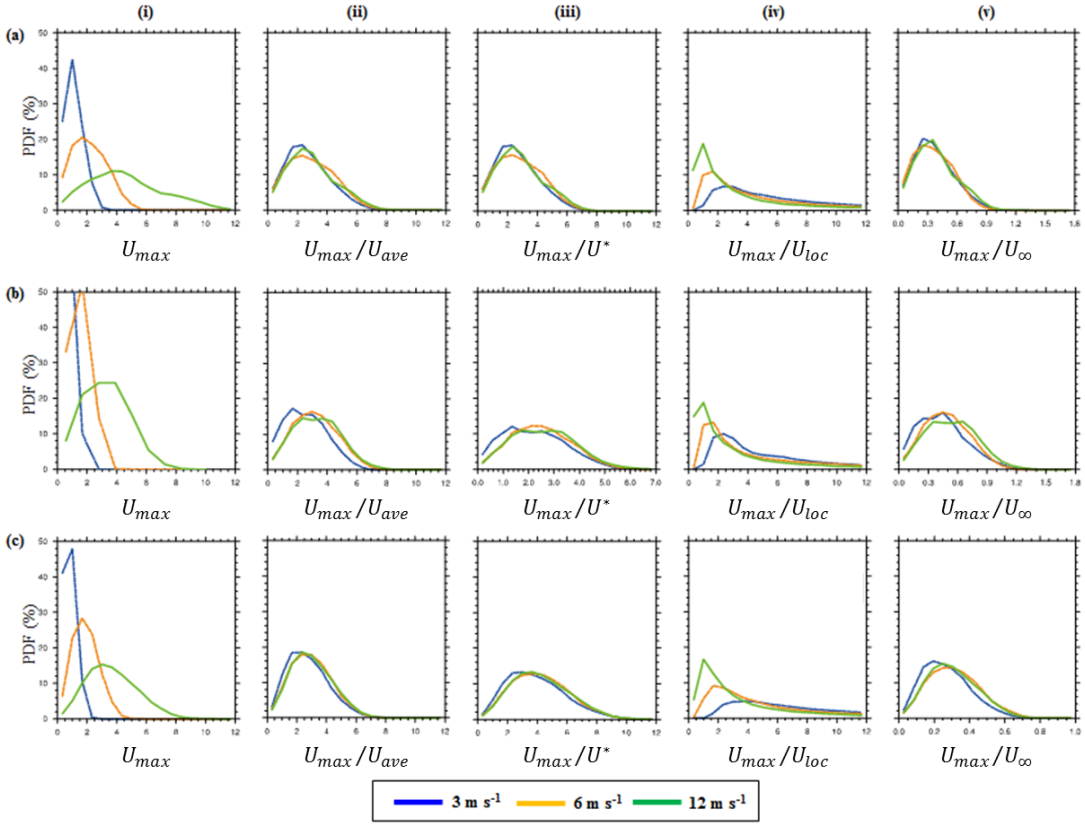

Figure 4.5 Probability density distribution of the (i) maximum wind speed, U_{max} and for four different definitions of the gust index, (ii) U_{max}/U_{ave}, (iii) U_{max}/U^*, (iv) U_{max}/U_{loc}, (v) U_{max}/U_∞ for the (a) commercial land (b) skyscrapers (c) residential area. Different line colours show the change in the input wind speed.

From the analysis done, the U_{max}/U_∞ as in Fig. 4.5v was proposed as the feasible gust index definition to be used in this study. The probability density

distributions of this definition were independence with the change in the input wind. Moreover, the U_∞ is homogeneous spatially and temporally at the measured height. The other two definitions which are U_{max}/U_{ave} and U_{max}/U^* seem to be acceptable. However, U_{ave} changes with height which lead it to be impossible in the consideration while the U^* is difficult to be obtained. Moreover, both are not homogeneous throughout the simulation domain. The other definition, which is U_{max}/U_{loc} obviously dependant to the change in the simulation inflows and this ratio eliminated.

4.4 Summary

This chapter consist of two main subjects. The simulation models, the PALM and LBM were verified with the results from the wind tunnel test on an isolated cube. The vertical profile of the average wind speed examine at selected locations. The profiles show a good agreement with the experimental results as the grid resolution increased. The profiles from different domain resolution also compared. Consequently, the 0.75 m (N = 64) resolution gave the best fit profiles between the PALM and LBM simulations. However, the 2 m (~N = 32) domain resolution in all direction still gave a compatible results and was chosen for the actual simulations for an efficient computation in term of time and cost. Next, the justification of a representative gust index which is appropriate for the spatial distribution was done. The ratio between the maximum instantaneous wind speeds to the free stream velocity applied in generalising the relationship between the gusts event and the urban morphology.

CHAPTER 5

GENERAL DESCRIPTION OF THE FLOW FIELD WITHIN A REALISTIC URBAN AREA

5.1 Introduction

General description of the flow field from the simulation output will be presented in this chapter. It is divided into two main parts which focus on the boundary layer development together with the parameters of the realistic urban domain and the wind profile in streamwise and vertical direction. Besides understanding the flow characteristics, all the figures illustrated confirm the correctness of the simulations executed. The data presented here retrieved from the large eddy simulation (LES) that applied the lattice Boltzmann method (LBM).

5.2 Urban Geometry Parameters and Boundary Layer Development

The building height in the three dimensional and the plan views were shown previously in Fig. 3.3 and 3.4 of Chapter 3 respectively. Figure 5.1 statistically presents the averaged values (in spanwise) of the important parameters that describe the simulation domain.

There are a number of tall buildings (H_{max}) which more than 60 m height along the streamwise. In average, the building height (H_{ave}) is about 10 m while its standard deviation, σ_H, lies in between 5 to 15 m. The plan area index, λ_p, and the frontal area index, λ_f, increase along the streamwise. The λ_f was calculated only in the same wind direction applied in the simulation which is from the left to the right of the domain. It is important to note that the domain ground surface is just flat (i.e.; no topography). Equations 5.1 to 5.4 used to calculate the H_{ave}, σ_H, λ_p and λ_f respectively From this general building statistics, it is shown that the simulation domain contained a rough, dense and realistic urban figure except at the beginning of the domain which is just a flat inlet. These urban parameters are also important in explaining the growth of the boundary layer where it starts to develop from the first building edge.

$$H_{ave} = \frac{\sum_{i=1}^{i=n} H_i}{n} \tag{5.1}$$

$$\sigma_H = \sqrt{\frac{\sum (H_i - H_{ave})^2}{n}} \tag{5.2}$$

$$\lambda_p = \frac{\sum A_p}{\sum A} \tag{5.3}$$

$$\lambda_f = \frac{\sum A_f}{\sum A} \tag{5.4}$$

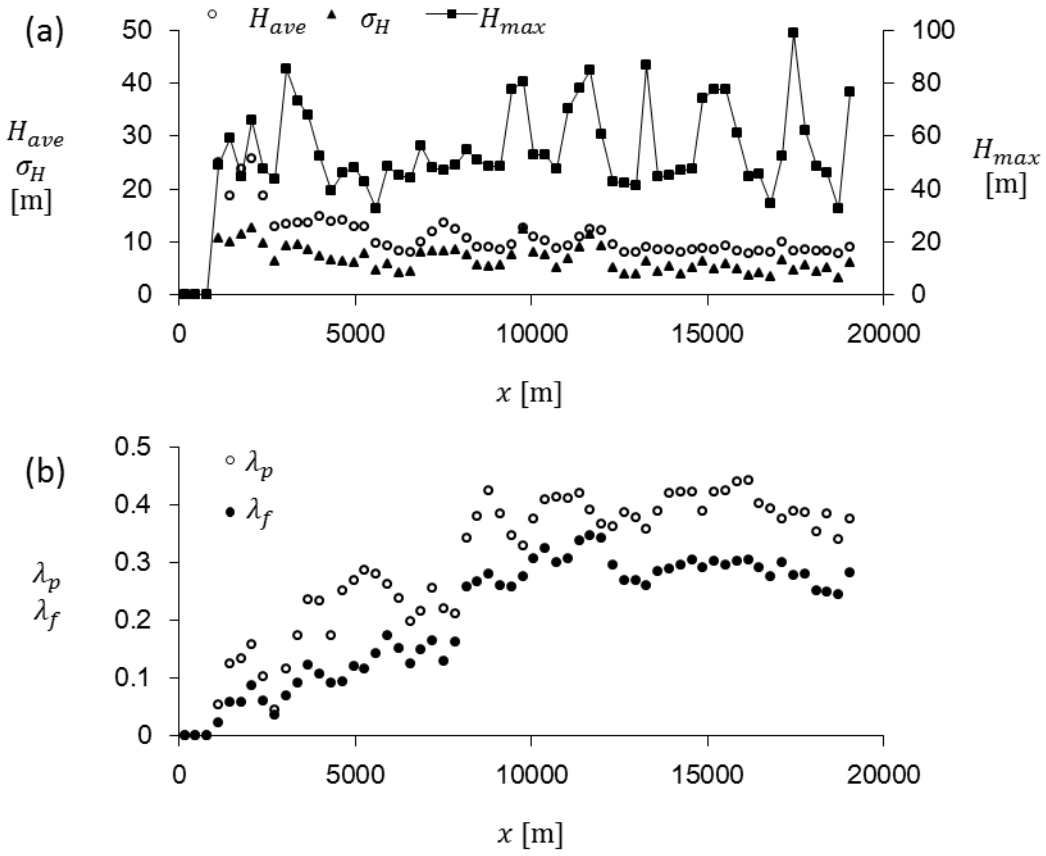

Figure 5.1 Geometry parameter of the simulation domain. (a) Maximum building height, H_{max}, average building height, H_{ave} and its standard deviation σ_H. (b) The plan area index, λ_p and frontal area index, λ_f.

The boundary layer height, δ developed along the streamwise direction of the simulation domain (x-direction). Its development generate by the shear driven turbulent due to the urban roughness (i.e.; no buoyancy). In general, the δ is the distance normal from the ground surface to the height where $U = 0.99U_{\infty}$. The height increases along the x-direction as shown in Fig. 5.2a and reached almost 500 m. The δ (y-axis) and domain streamwise (x-axis) is illustrated in Fig 5.2b again by the logarithmic scale. The δ calculated from the simulation is compared with an experimental result from Garratt (1990). It was a neutral wind tunnel experiment to study the boundary layer growth from a smooth to rough surface and represent by $\delta = (z_{01}/z_{02})x^{0.8}$. The gradient of the simulation and the experimental were match but differ in values. This is cause by the different in the surface roughness ratio. Moreover, Jiménez (2004) discovered that the roughness elements became less effective to the logarithmic layer as it ratio to the boundary layer height, δ/k more

than 40. Figure 5.2c confirm this relationship as the normalised values of the H_{ave}/δ and σ_H/δ is almost constant at about 0.02 for the latter half of the domain.

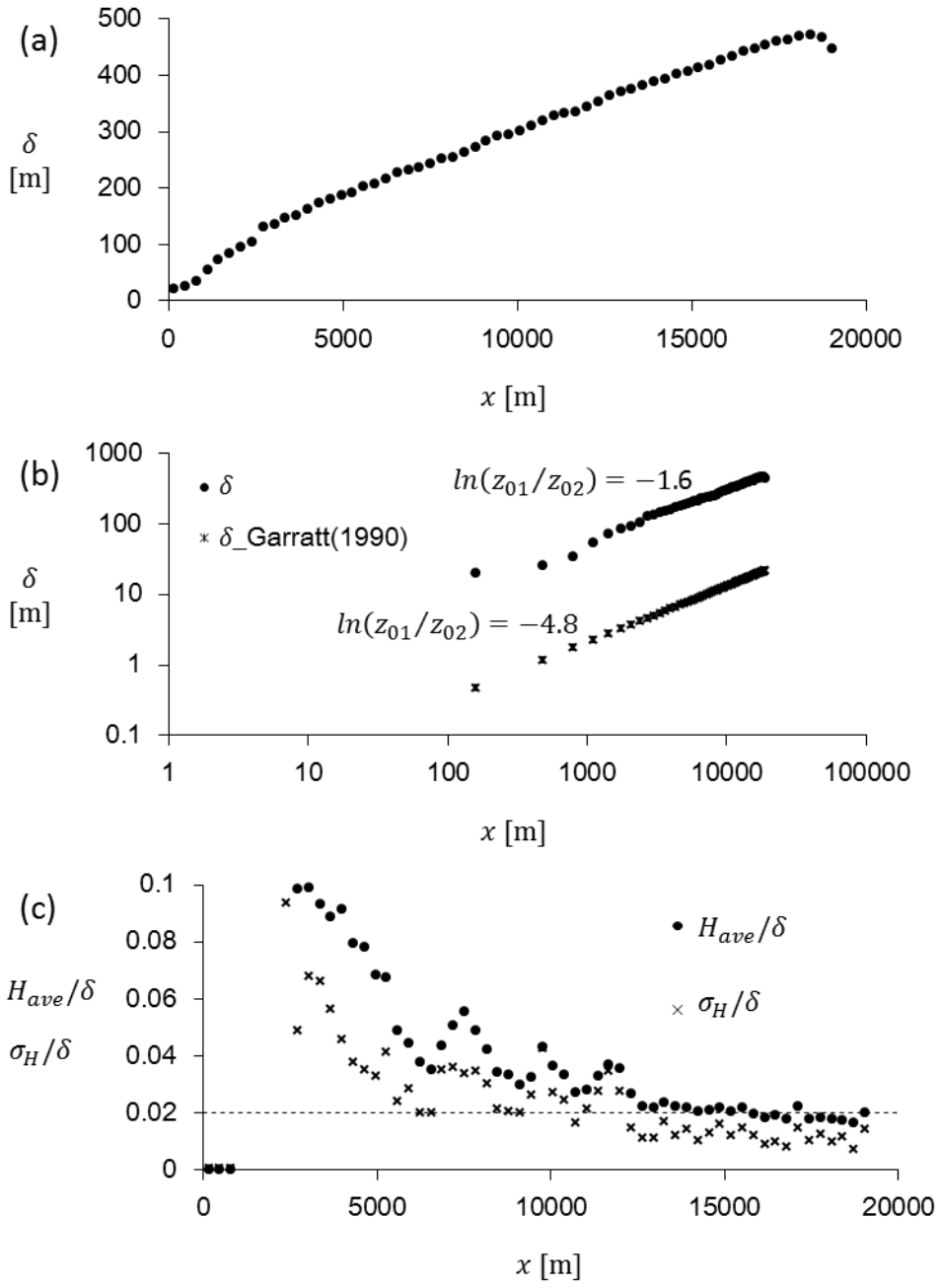

Figure 5.2 Boundary layer height, δ calculated from the (a) simulation and compared with (b) Garratt (1990). (c) Normalised values of the H_{ave} and σ_H to the δ.

5.3 Wind Flow Properties

5.3.1 Streamwise profile

As shown in Fig. 5.3, the friction velocity, u_*, was obtained by extrapolating the $u'w'$ profiles along the domain streamwise as the $u_* = \sqrt{|u'w'|}$. The U_∞ is referred to the freestream velocity at 600 m height from the ground measured from the mean velocity profile of u. The values multiply by 0.1 to fit it in the same scale range of the u_*. The other side of the *y*-axis shows the normalised boundary layer height along the domain streamwise, $d\delta/dx$. The u_* is almost homogeneous in streamwise except at the domain inlet. Same goes to the U_∞ and $d\delta/dx$ but there is a sudden drop at the end of the domain for the $d\delta/dx$ because the boundary layer did not develop anymore at this point.

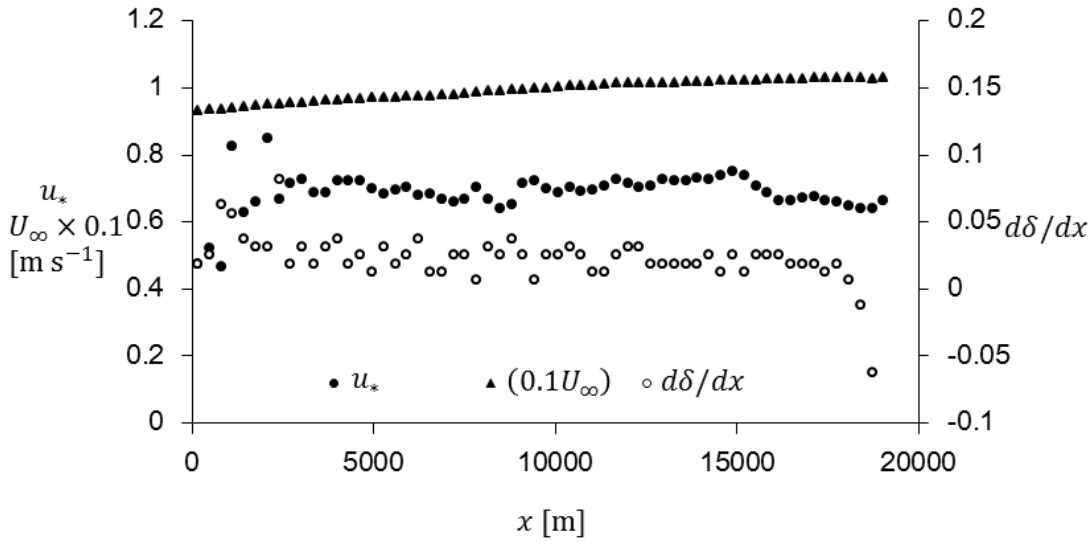

Figure 5.3 The friction velocity, u_*, freestream velocity, U_∞ and the normalised boundary layer height along the domain streamwise, $d\delta/dx$.

5.3.2 Vertical profile

The flow field of the simulation also can be described by the several vertical profiles. Raupach et al. (1991) stated that the normalised vertical profiles of single-point velocity moments ($\overline{u^2}$, $\overline{v^2}$, $\overline{w^2}$, $\overline{uw}$, and higher moments) to the u_* and δ should collapse to common curves independent of wall roughness at a certain height. Figure 5.4 shows that the normalised profiles of U, $\overline{u'w'}$ and the standard deviations $\sigma_u = \left(\overline{u^2}\right)^{1/2}$, $\sigma_v = \left(\overline{v^2}\right)^{1/2}$ and $\sigma_w = \left(\overline{w^2}\right)^{1/2}$ all 'tied up' onto common curves when z/δ more than 0.6. This condition is exceptional in the roughness sublayers close to the surface because a realistic urban geometry applied in this study. The vertical profiles from this study also somehow obeying the wind tunnel tests on the aligned and staggered uniform cube from Cheng and Castro (2002).

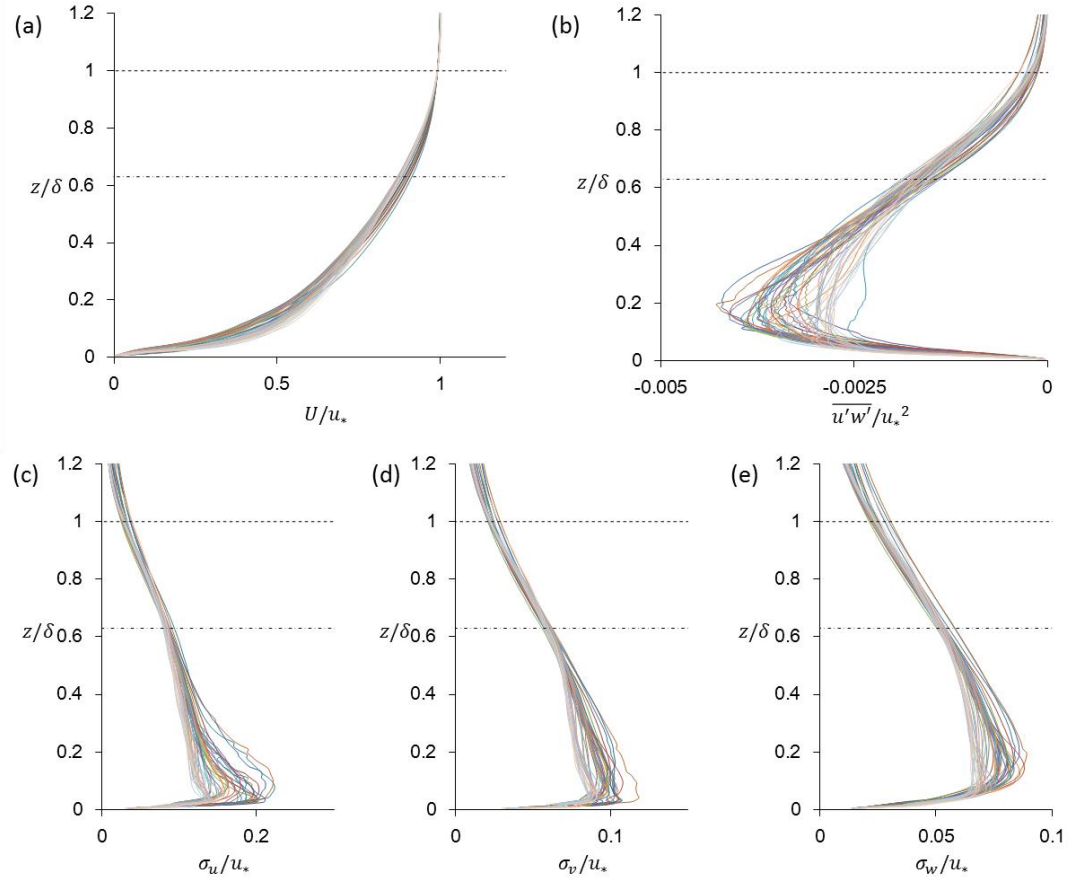

Figure 5.4 Profiles against z/δ of (a) U/u_*, (b) $\overline{u'w'}/{u_*}^2$, (c) σ_u/u_*, (d) σ_v/u_* and (e) σ_w/u_*.

5.4 Summary

Several main urban parameters such as the H_{max}, H_{ave}, σ_H, λ_p and λ_f of the domain enclosed in the LBM simulations described briefly. These parameters indicated the characteristics of the rough and dense urban morphology as the λ_p and λ_f increased along domain streamwise. There are also many high rise buildings which over 60 m height. While, the H_{ave} and σ_H values lay in between 10 m and 15 m respectively. The urban boundary layer started to develop from the beginning of the building edge and reached at almost 500 m height near the domain outlet. The general description on the streamwise and the vertical wind flows also presented in this chapter. The U_∞ shown an acceptable homogeneous distribution along the streamwise compare to the u_*. Whereas, the vertical profiles illustrated were reliable as those profiles matched with the theoretical and experimental results from the flow over a rough-wall and the turbulent boundary layers.

CHAPTER 6

HORIZONTAL DISTRIBUTION OF THE FLOW FIELD WITHIN A REALISTIC URBAN AREA

6.1 Introduction

The horizontal distribution (*xy*-plan) of several flow statistics at different heights were presented in this chapter. These figures provide visual information which was referred to get a better understanding of the wind flow characteristics within and over a realistic urban area. Also, the reliability of the accomplished numerical simulations can be confirmed. Furthermore, the proposed gust index definition from Chapter 2 also used to map it spatial distribution and visually inspected in this chapter. The gust index component maps also illustrated and discussed. The data presented here mainly retrieved from the large eddy simulation (LES) that applied the lattice Boltzmann method (LBM).

6.2 Horizontal Distribution of the Flow Field

The horizontal distribution (*xy*-plan) of several flow statistics at different heights (i.e.; 2 m, 54 m, 98 m and 198 m) were illustrated and described briefly in this section. The flow statistics listed as the instantaneous wind velocity (u_{ins}), each component of the mean wind (u, v and w), instantaneous, mean and turbulent part of the Reynolds stress ($u_{ins}w_{ins}$, uw and $u'w'$) and the standard deviation of the v and w component (σ_v and σ_w). Figure 6.1 to 6.11 show all those horizontal distributions. Each chosen height represent the pedestrian level, Doppler lidar height (installed on top of a building within Tokyo Tech campus), above roughness length and free stream height respectively. All mean statistics were temporally average for the last 600 s of the simulation time. The colour range assign accordingly.

6.2.1 Instantaneous wind velocity

The instantaneous wind velocity of the streamwise direction (u_{ins}), is shown in Fig. 6.1. Coherent streaky pattern became more apparent at higher level. The tailed streaks along the streamwise influence by the existent of the urbanize area (i.e.; high-rise buildings). It also can be seen that the streaks width change with height and fetch from the inlet. Approximately, the width of the streaks at the latter half of the horizontal distribution of the 54 m, 98 m and 198 m height, are more consistent as the boundary layer (refer to Fig. 5.2a of Chapter 5) is high enough at this point. More thinner and shorter streak pattern can be seen at 2 m height mainly at the open spaces. The flow field at this level was directly modified by the urban morphology and induced more intermittent flow distribution.

6.2.2 Mean wind velocity

Figure 6.2 to 6.4 show the mean wind of the streamwise (u), spanwise (v) and vertical (w) components respectively. The u is a dominant component compared to v and w by simply referring to the colour range of the plot. This is due to the inflow setting which is from the left to the right of the domain. The u streaks became broader in spanwise and elongate in the streamwise. The same judgement as describe for the u_{ins} use to explain these patterns. However, the streaks pattern are smoothen due to the temporal average as mentioned earlier. The flow field change with height logarithmically. Therefore, the horizontal distribution became more homogeneous at higher level (i.e.; 198 m) especially at the latter half of the domain fetch. The discrete distribution pattern for v and w up to 98 m mainly modified by the urban morphology (i.e.; buildings, streets and open spaces). At 198 m, elongated streaky pattern became more distinct for both components although 'blurred' ground morphology still can be seen.

6.2.3 Reynolds stress

The instantaneous, mean and turbulent component of the Reynolds stress (i.e.; $u_{ins}w_{ins}$, uw and $u'w'$) shown in Fig. 6.5 to 6.7 correspondingly. The colour range of all components is similar for all height except at 2 m. It makes the evaluation of this vertical transport of momentum simpler. The instantaneous and mean characteristics of the Reynolds stress did not show a significant different compared to the turbulent component. More homogeneous spatial distribution can be identified at the ground level (i.e.; 2 m). At the higher levels, the upwards (positive) and downwards (negative) momentum transport separated by the streaky structures that are elongated along the streamwise direction. It indicates that the streaky structures are predominantly important in the turbulent transport process at the upper level (i.e.; within the inertial sublayer, roughness sublayer). However, these streaky structures were also discretized along the broad streets and open spaces which signified the influence of the urban canyon on the upper layer flow field. The

turbulent characteristics became more homogeneous at the upper layer because the mean component is more significant, where the freestream profile obeying the logarithmic law.

6.2.4 Standard deviation

Figure 6.8 and 6.10 show the standard deviation of the spanwise (σ_v) and vertical (σ_w) components respectively. While, Fig. 6.9 and 6.11 are the mean velocity (i.e.; v and w) with the same colour range of the correspond standard deviation. The σ_v distribution at all levels illustrated are always larger compared to the σ_w (i.e.; more fluctuation in spanwise (v') instead of vertical direction (w')). Moreover, v dominates the distribution over w at the ground level (i.e.; 2 m). In contrast, w begins to take over v at 54 m and became more apparent at higher level (i.e.; 98 m and 198 m). In general, these explain that the local instantaneous in the spanwise (v_{ins}) at the all levels is always larger compared to the one in vertical (w_{ins}) as the standard deviation is given by:

$$\sigma_A^2 = \frac{1}{N}\sum_{i=0}^{N-1}(A_i - \bar{A})^2 = \frac{1}{N}\sum_{i=0}^{N-1} A_i'^2 = \overline{A'^2}$$
$$\sigma_A = \left(\overline{A'^2}\right)^{1/2}. \tag{6.1}$$

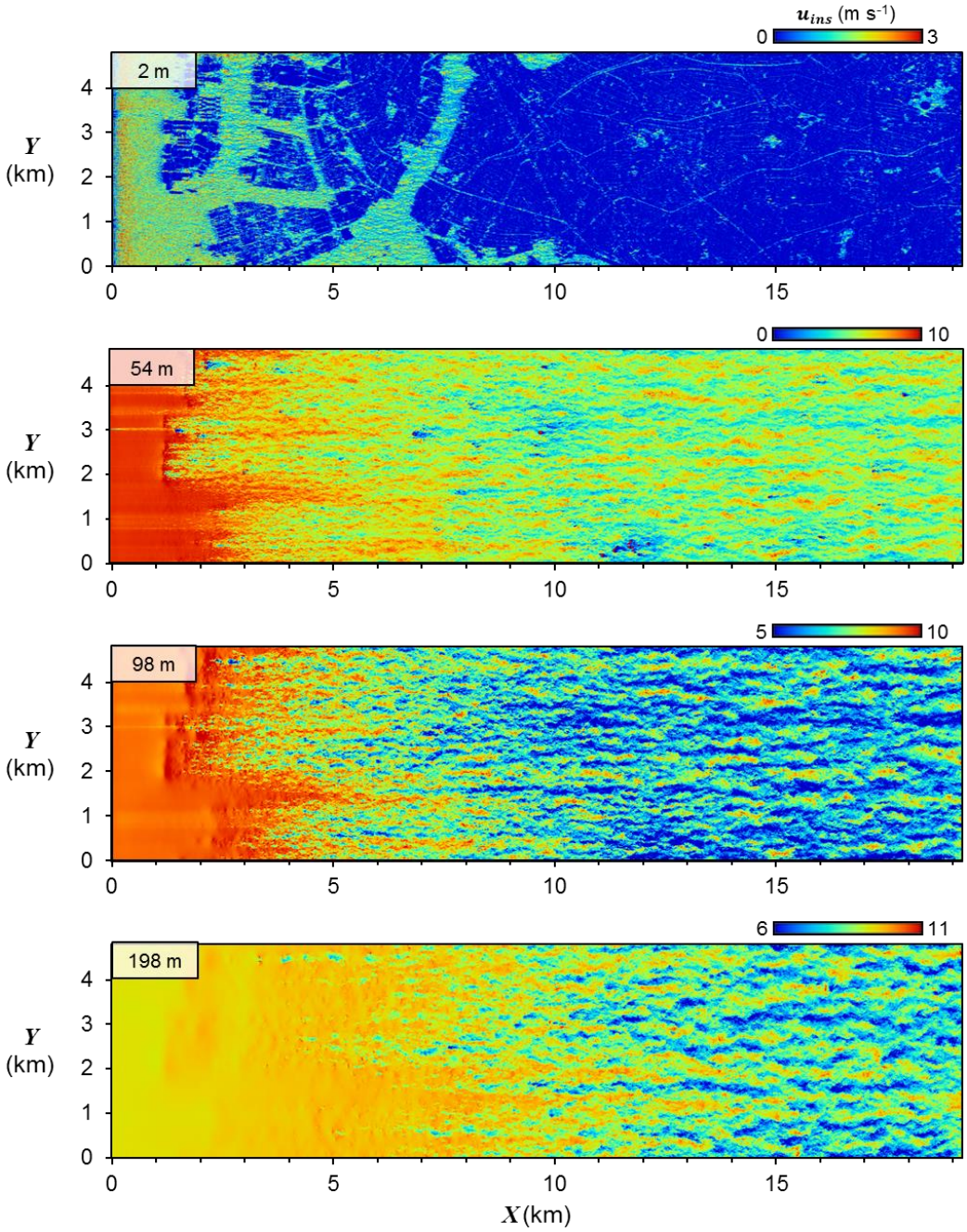

Figure 6.1 Horizontal distribution (*xy*-plan) of the instantaneous wind velocity, u_{ins}, at 2, 54, 98 and 198 m height.

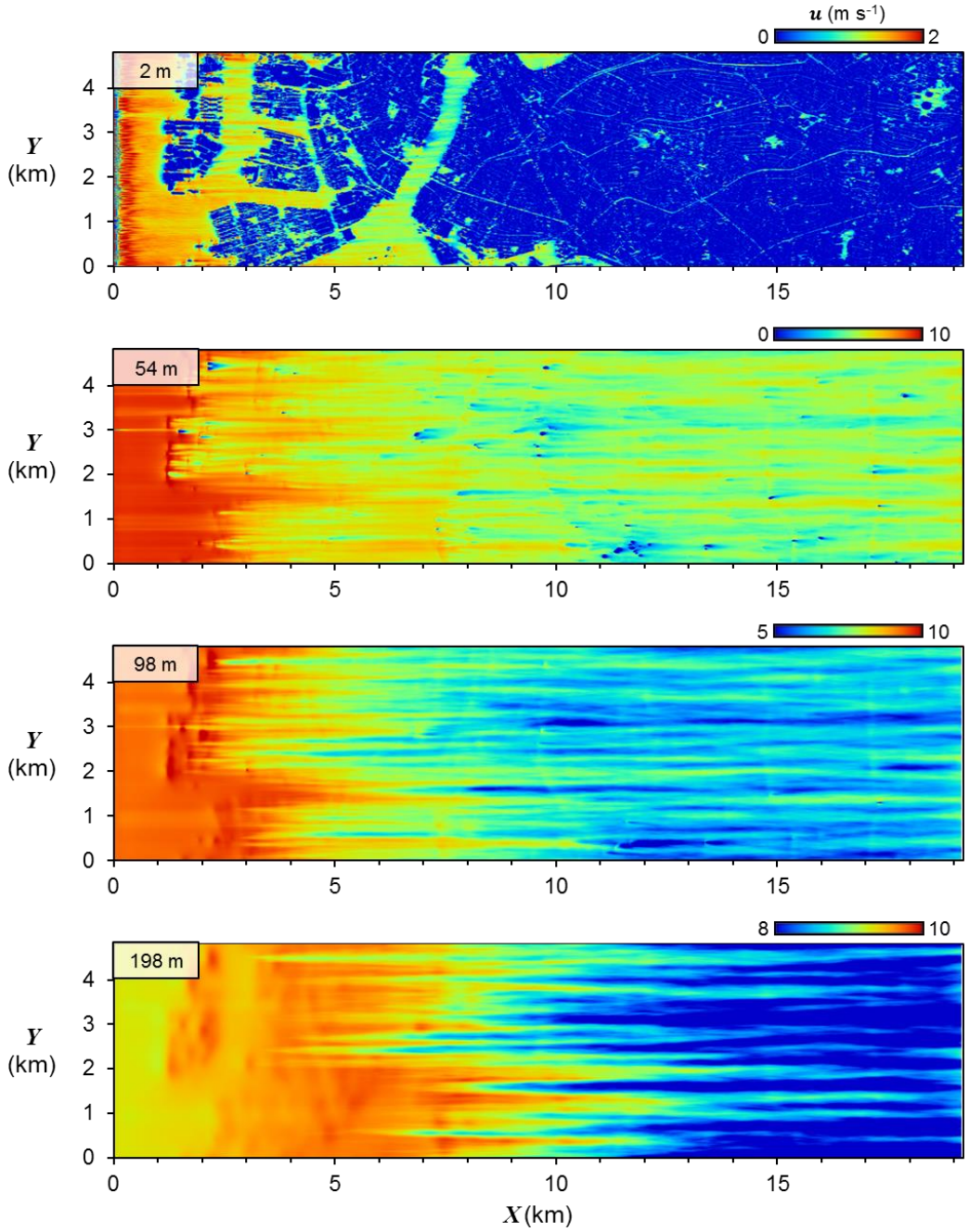

Figure 6.2 Horizontal distribution (*xy*-plan) of the mean wind velocity (u-component) at 2, 54, 98 and 198 m height.

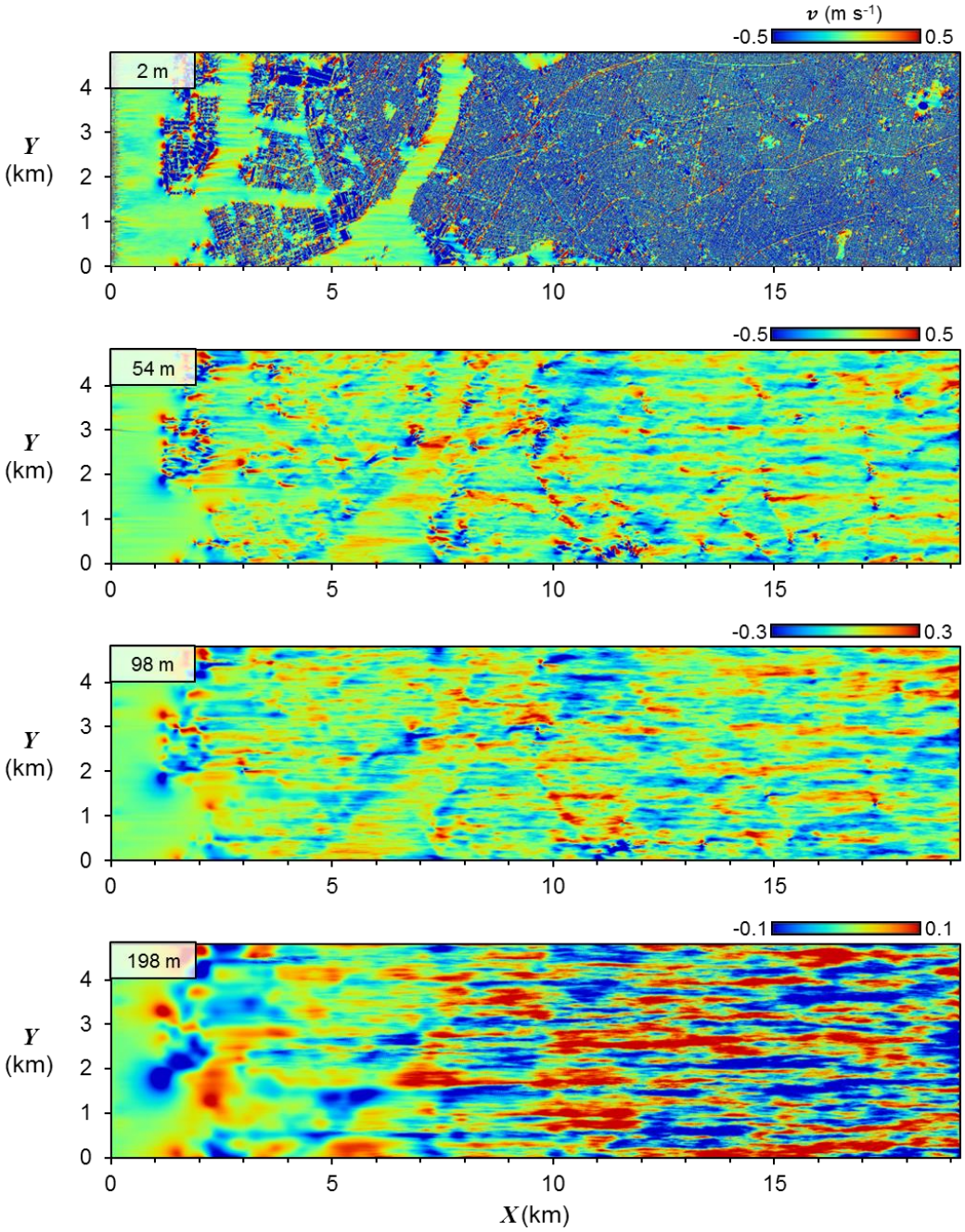

Figure 6.3 Horizontal distribution (*xy*-plan) of the mean wind velocity (v-component) at 2, 54, 98 and 198 m height.

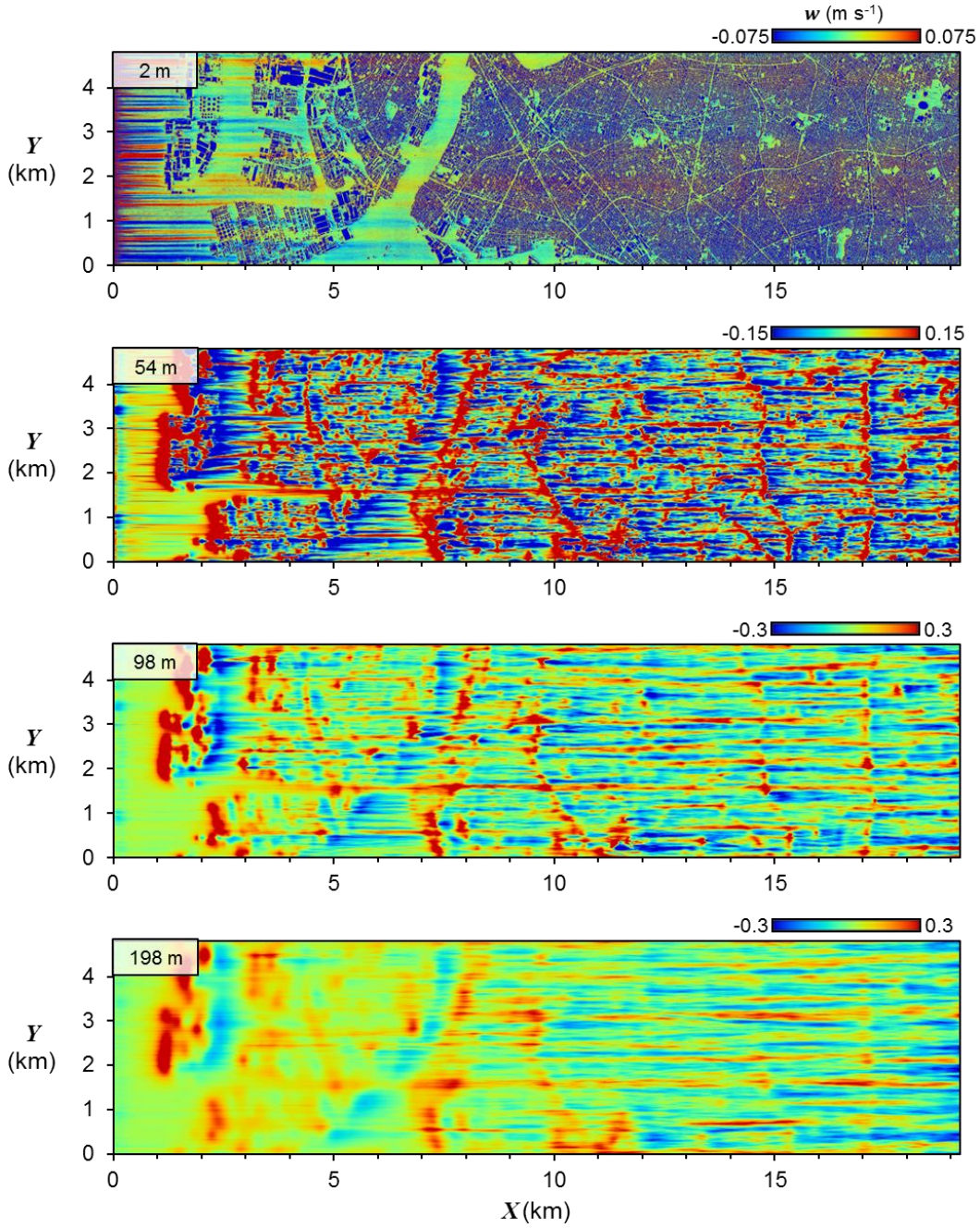

Figure 6.4 Horizontal distribution (*xy*-plan) of the mean wind velocity (*w*-component) at 2, 54, 98 and 198 m height.

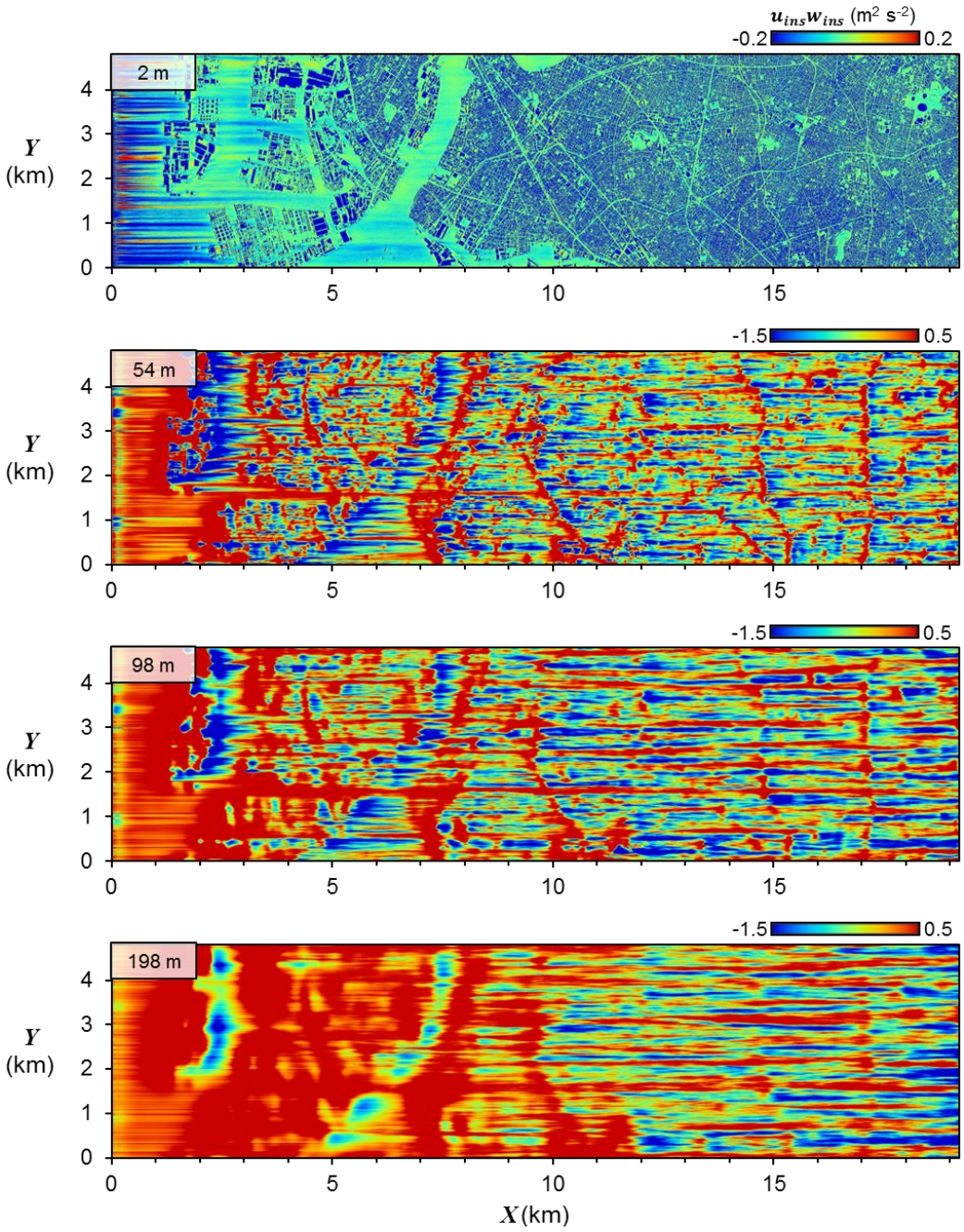

Figure 6.5 Horizontal distribution (*xy*-plan) of the Reynolds stress (instantaneous component) at 2, 54, 98 and 198 m height.

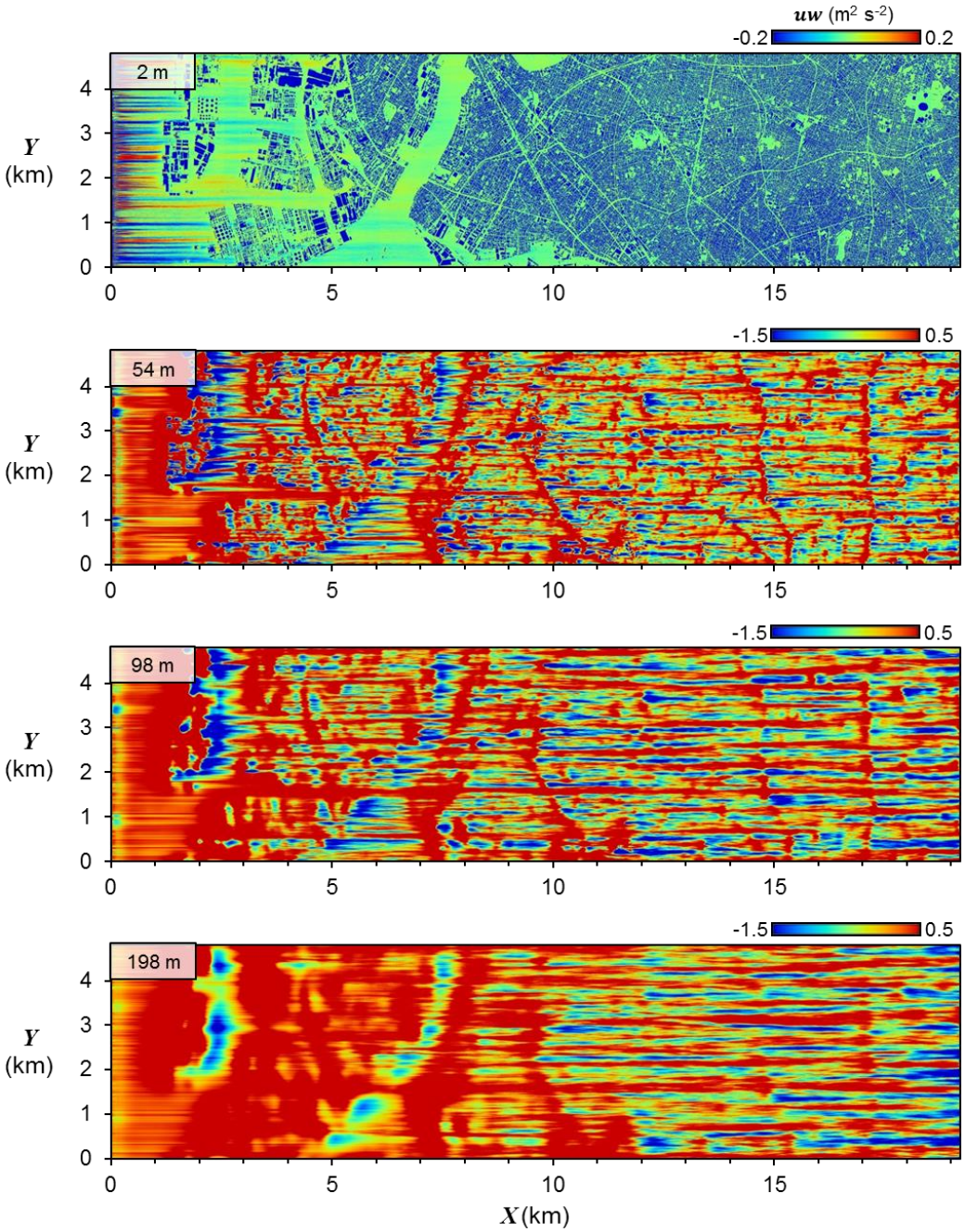

Figure 6.6 Horizontal distribution (*xy*-plan) of the Reynolds stress (mean component) at 2, 54, 98 and 198 m height.

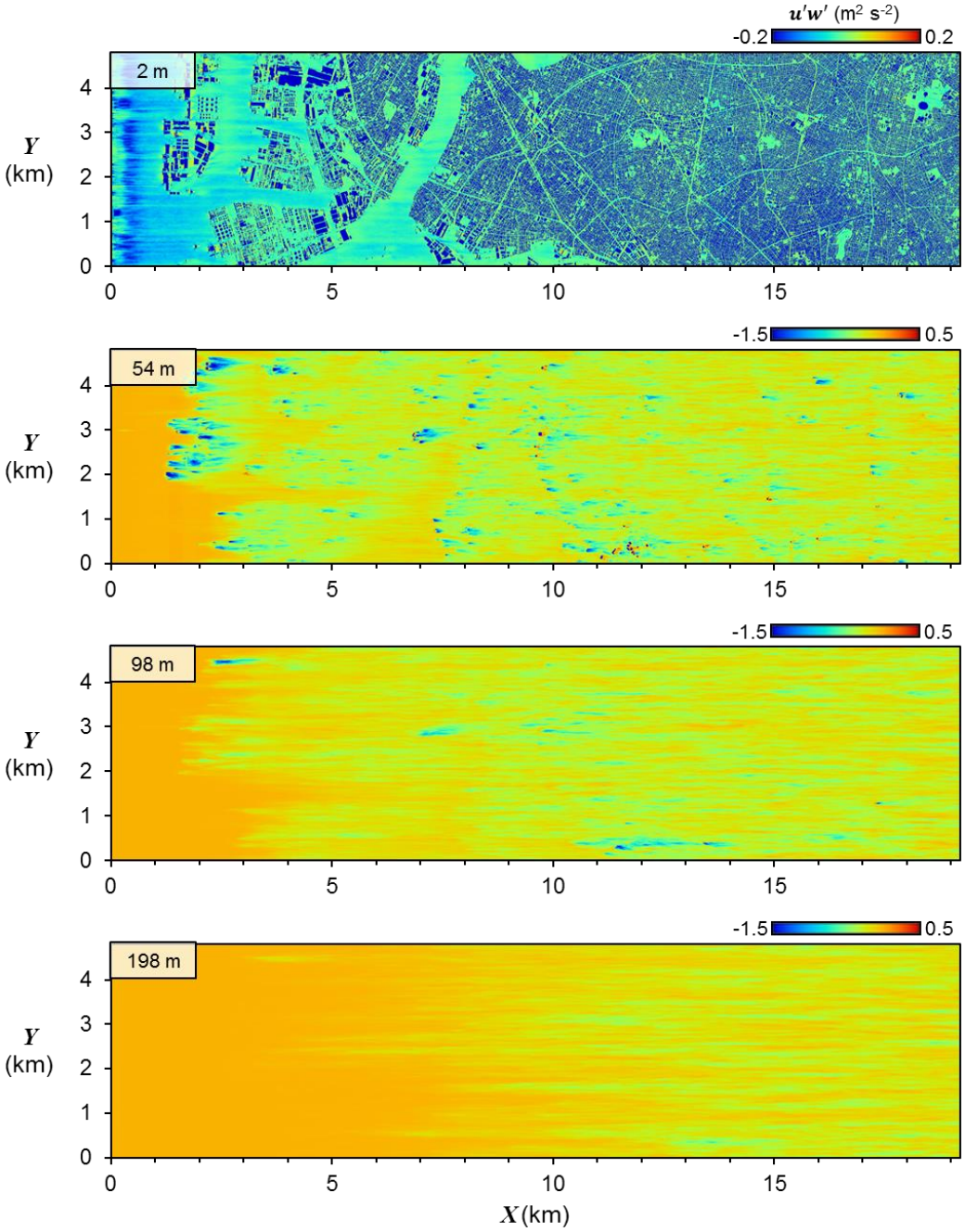

Figure 6.7 Horizontal distribution (*xy*-plan) of the Reynolds stress (turbulent component) at 2, 54, 98 and 198 m height.

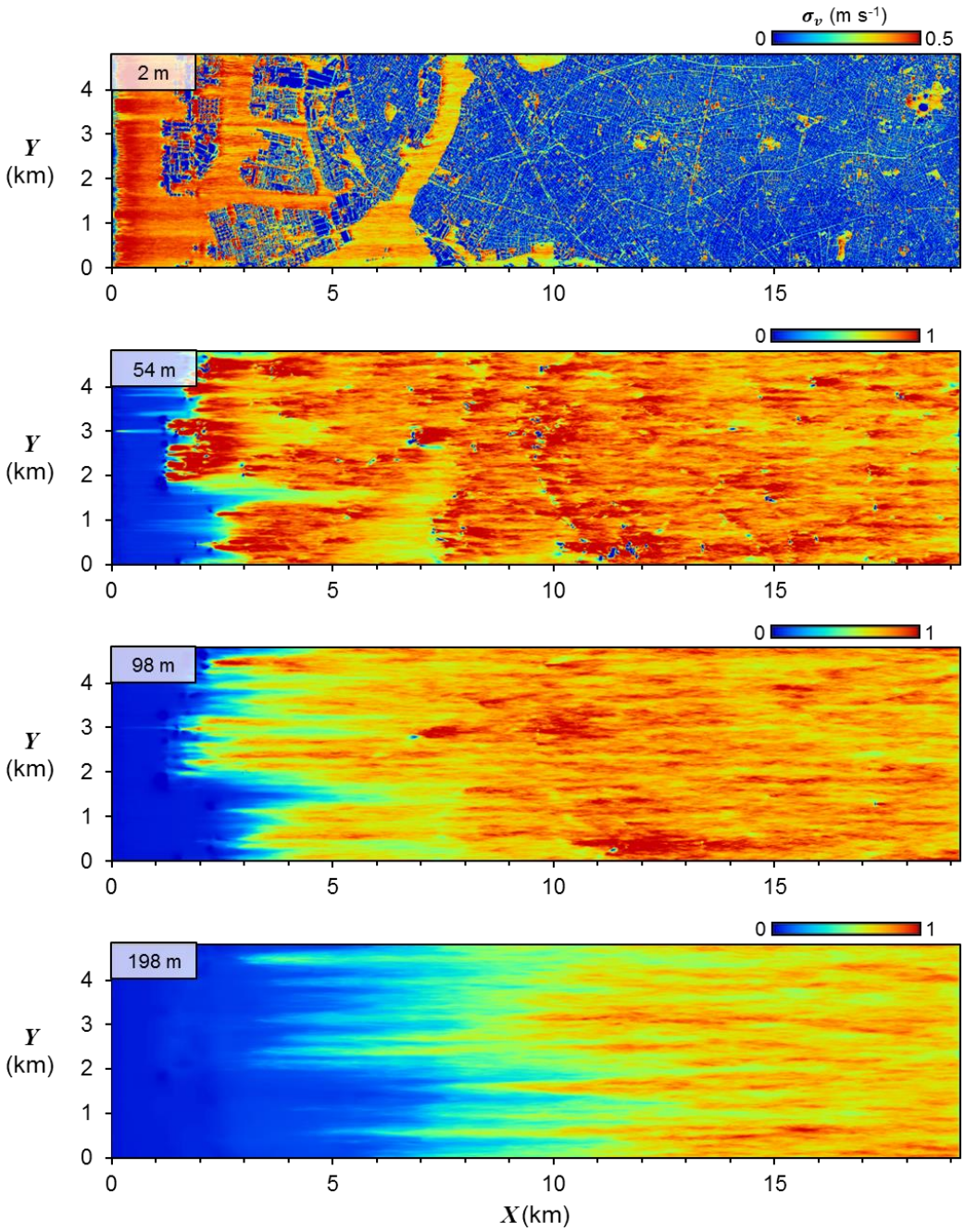

Figure 6.8 Horizontal distribution (*xy*-plan) of the standard deviation (v-component) at 2, 54, 98 and 198 m height.

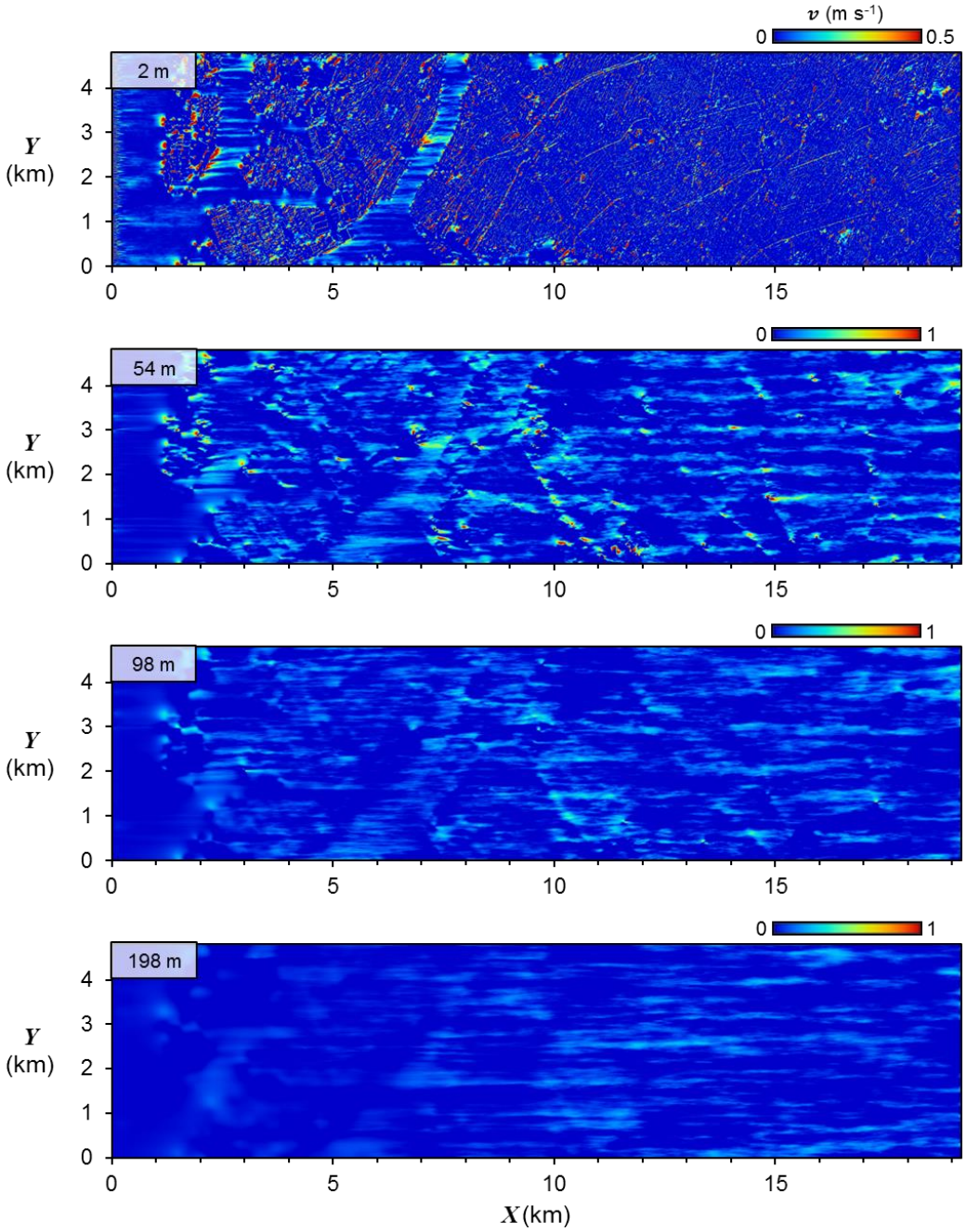

Figure 6.9 Horizontal distribution (*xy*-plan) of the mean wind velocity (v-component) at 2, 54, 98 and 198 m height (same as Fig. 6.3 but following the colour range of Fig. 6.8).

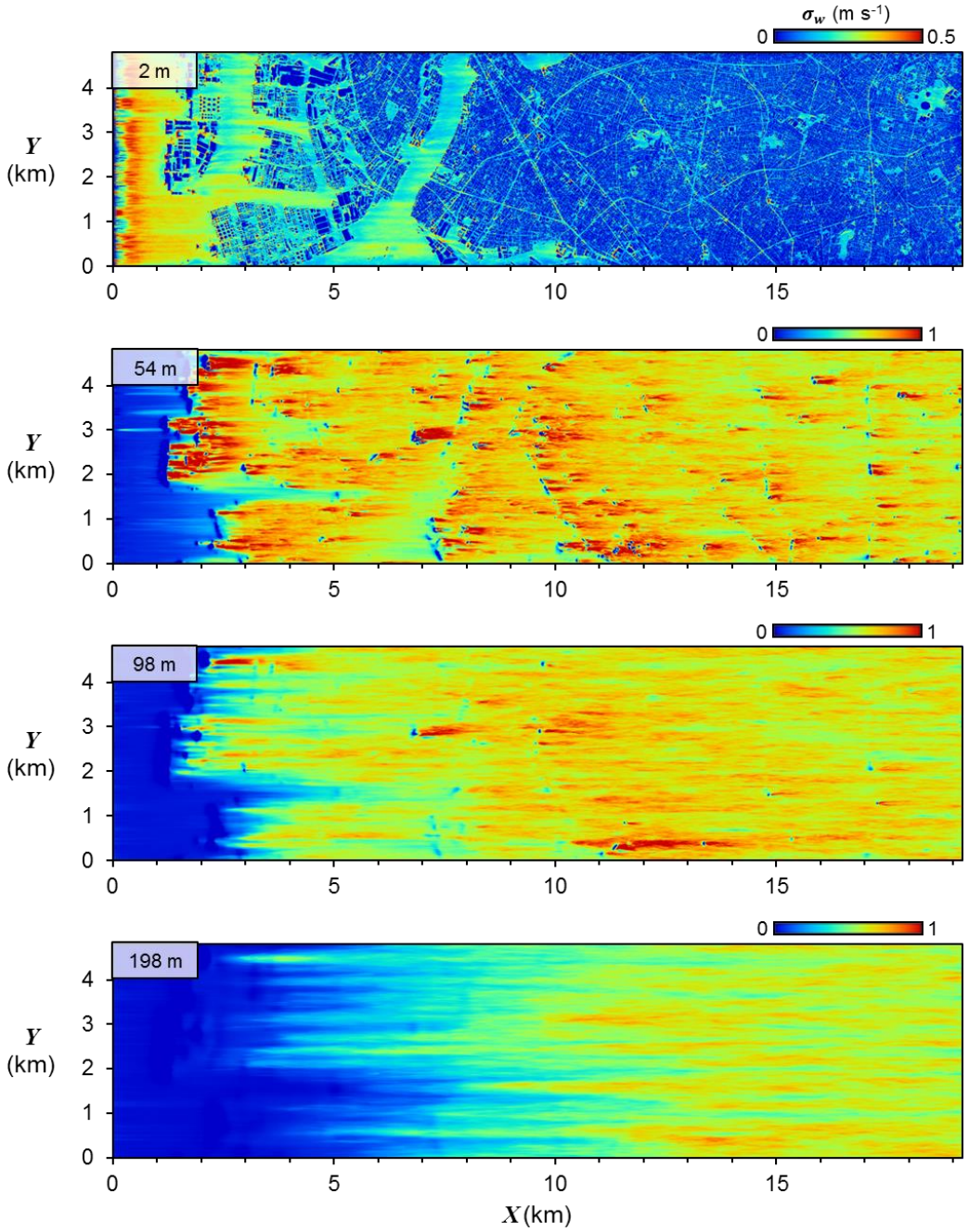

Figure 6.10 Horizontal distribution (*xy*-plan) of the standard deviation (*w*-component) at 2, 54, 98 and 198 m height.

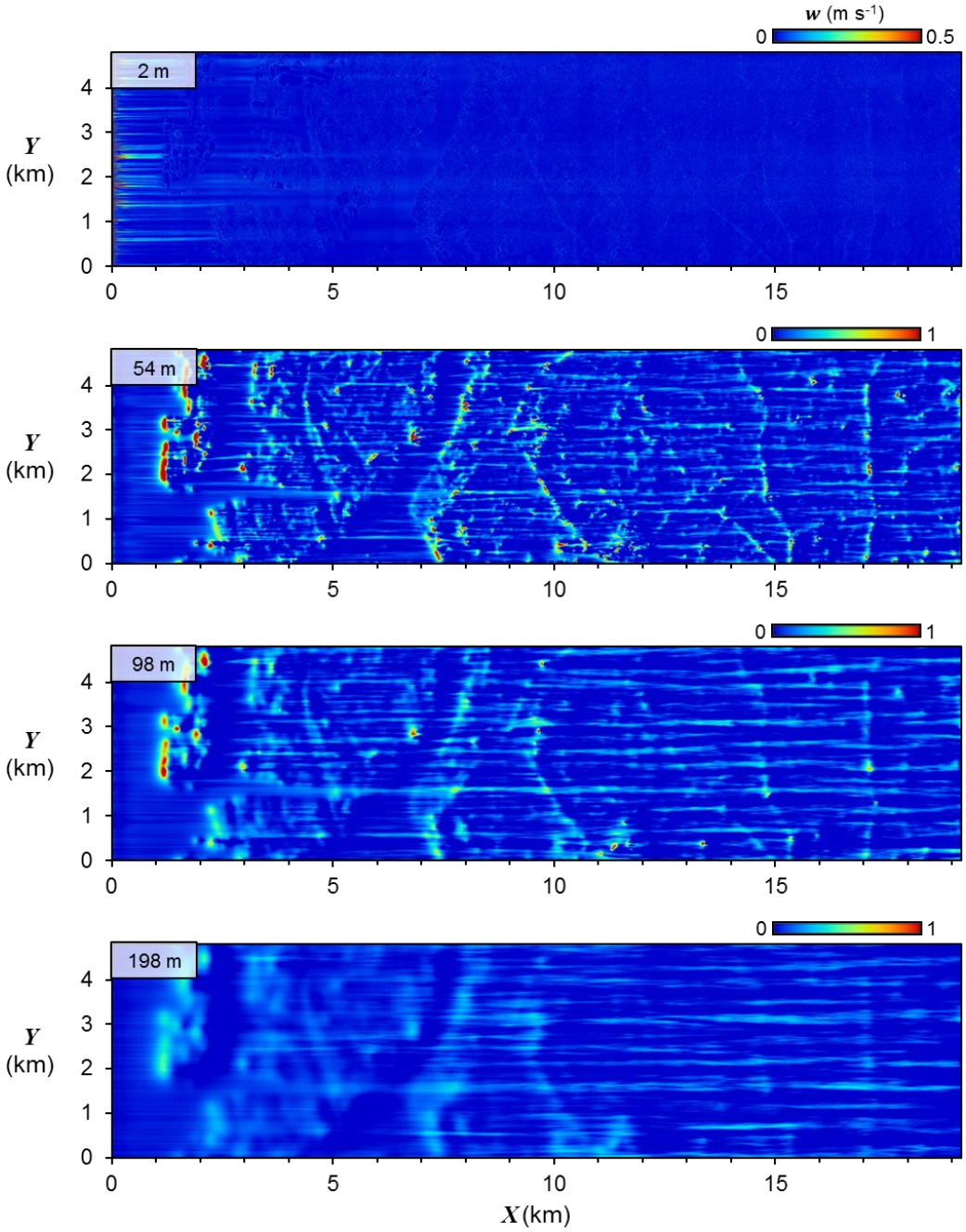

Figure 6.11 Horizontal distribution (*xy*-plan) of the mean wind velocity (*w*-component) at 2, 54, 98 and 198 m height (same as Fig. 6.4 but following the colour range of Fig. 6.10).

6.3 Horizontal Distribution of the Gust Index and its Component

The gust at 2 m height that normalized to the freestream velocity at 600 m height (i.e.; domain top) used to plot the GI spatial distribution (Huda et al. 2014; Huda et al. 2015) as shown in Fig. 6.12. The same range of the colour contour used to differentiate the gust index distribution on the different surface geometry which categorized as the commercial land, skyscrapers and residential area. The spot of the maximum GI concentrate more within the skyscrapers and commercial land compared to the residential area. In general, the higher distribution of the gust index may occur around the taller buildings that have some open space around it compared to the lower one nearby it. The building height of these areas can be referred back in Fig. 3.1 of Chapter 3. From the figure also, it is suggested that the proposed GI definition works well and understandable for the spatial distribution.

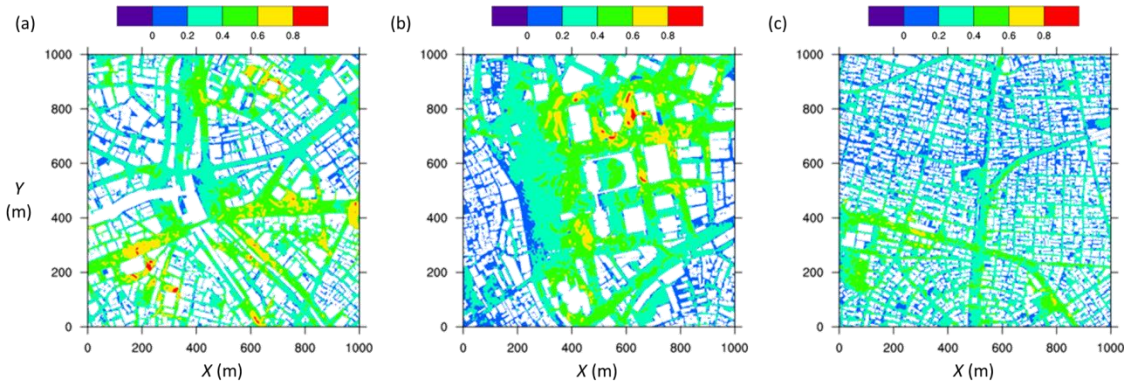

Figure 6.12 Gust index distribution at 2 m height for the 1,000 m × 1,000 m of the (a) commercial land, (b) skyscrapers and (c) residential area by using the proposed definition.

However, it is inadequate to quantitatively evaluate correlation between the gust and the urban parameter as the simulation done separately for different surface geometry. Therefore, another simulation was executed on a huge urban domain that considered the realistic building height variation and considerable range of the surface density. Figure 6.13 shows the horizontal distribution of the GI, MWR and TPR (as defined in Eqs. 2.2 to 2.5, Chapter 2) at 2 m height for the whole computational domain. A high GI was apparent at the domain inlet where there was

just a flat surface compared to the densely built-up area in the inland domain The big open spaces at x = 0~1 km (near inlet), 2~3 km (y = 2~4.8 km) and 5~8 km (across the entire domain in the y diagonal) had different magnitudes of GI, which decreased with distance in the x direction. There were also several locations with a high GI within the building canopies. These locations were examined by decomposing the GI into the MWR and TPR, which were visually inspected.

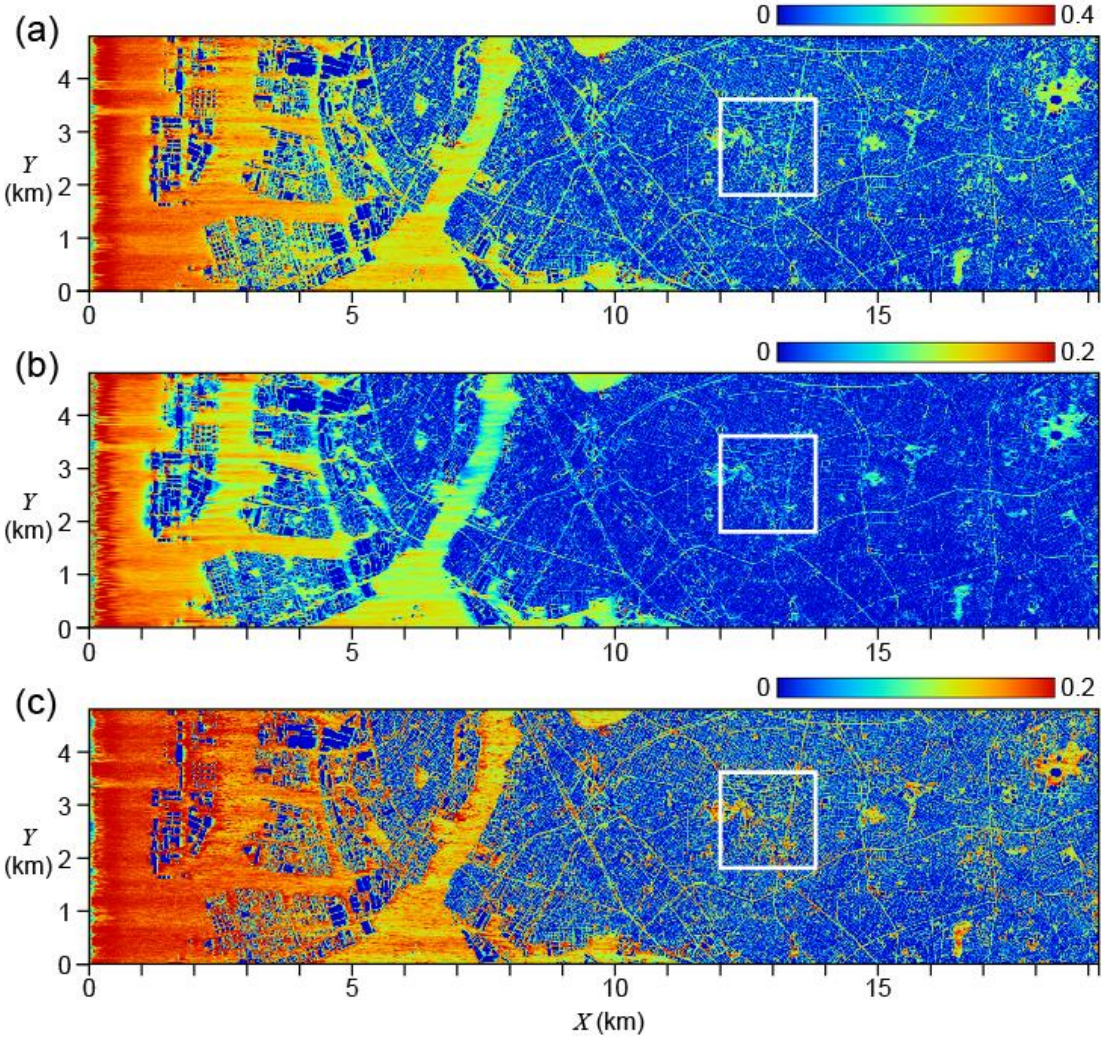

Figure 6.13 Horizontal distribution of the (a) gust index, $\widetilde{U}_{max}$, (b) mean wind ratio, $\widetilde{U}$, and (c) turbulent part ratio, $\widetilde{U}'$, at 2 m height.

Near the inlet, the flow field was not obstructed by any buildings and the wind speed, which indicated both the MWR and TPR, was faster than in the built-up area at the pedestrian level as seen in Fig. 6.13b, c. Another reason for the large GI

near the inlet was that the boundary layer height was low in locations where the gusty downdraft easily penetrated close to the ground. This could explain the decreasing GI with distance in the *x* direction within big open spaces. The influence of boundary layer development is further examined in sect. 7.3 of Chapter 7. Locations with a large GI in the built-up areas were mostly accounted for by the TPR, which in built-up areas was comparable with the TPR in the inlet, whereas the MWR in built-up areas was much smaller than in the inlet.

The area of focus in the white box is magnified in Fig. 6.14 to show more detail. The proposed GI plotted in Fig. 6.14a is compared to the distribution of the conventional gust factor (G) in Fig. 6.14b as defined in Eq. 2.1 of Chapter 2. G was very high around the building and within the narrow street. The main reason for this was because the local U was very low and almost stagnant, which was likely to cause a large G, with a small maximum wind speed relative to the surrounding area. This conventional definition limited the main goal of this study in determining the spatial distribution of the maximum wind that induces strong gusts at the pedestrian level.

The MWR was much lower than the TPR in the densely built-up area, particularly in the narrow streets within the building cluster. This implies that a group of buildings can effectively reduce the mean wind speed and generate turbulence near the ground. This characteristic is quantified in Sect. 7.4 of Chapter 7

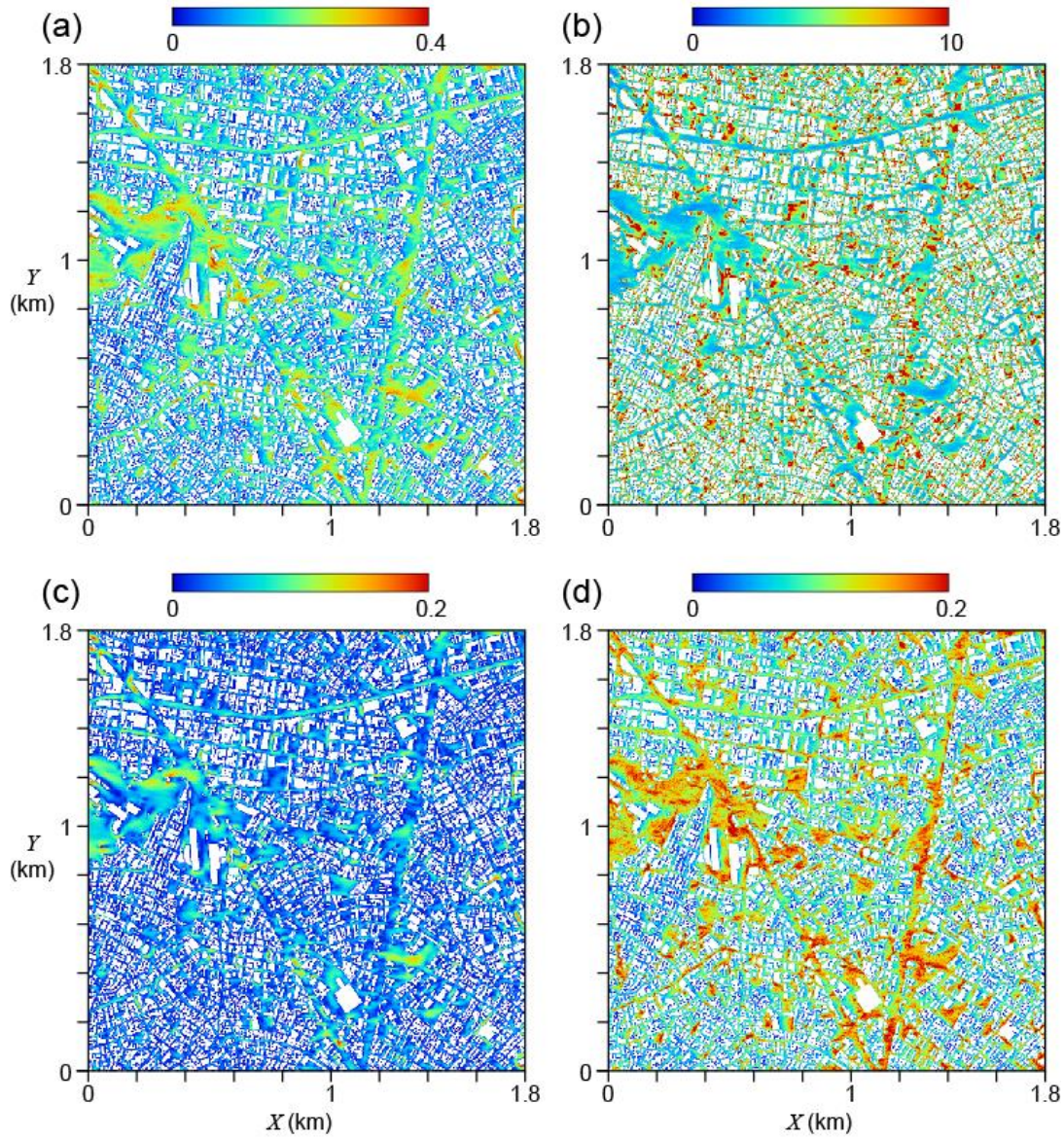

Figure 6.14 Magnified view overlain with the building height of the (a) gust index, $\widetilde{U}_{max}$, (c) mean wind ratio, $\widetilde{U}$, (d) turbulent part ratio, $\widetilde{U}'$, from Fig. 6.13 and (b) the spatial distribution of the conventional gust factor, G.

6.4 Summary

The horizontal distribution (*xy*-plan) of the instantaneous wind velocity, mean wind, Reynolds stress and standard deviation visualised. The wind flow characteristics of each slice at different height (i.e.; 2 m, 54 m, 98 m, 198 m) described mainly by referring the coherent streak pattern. Elongated and widen streaks in streamwise and spanwise respectively can be seen at the higher level. In contrast, near the ground, the building morphology directly modified the flow and created shorter and thinner streak pattern. Smaller domains from PALM used to examine the distribution of the GI at 2 m height spatially. The illustrated figures confirmed that the proposed GI definition works well and understandable. This GI definition imposed into the huge domain of the LBM simulation and successfully mapped the distribution at the ground level (i.e.; 2 m). Also, the new GI definition certified by comparing it with the conventional GF map. By visually inspected, the TPR seem dominated the contributed on the GI compared to the MWR. Further analysis will be presented in the next chapter to quantify the gust index and the urban parameter in obtaining their general relationship.

CHAPTER 7

GENERAL RELATIONSHIP BETWEEN THE GUST INDEX AND THE URBAN MORPHOLOGY

7.1 Introduction

The prime objective of this research will be presented in this chapter. The relationship between the gust index (GI) and the urban morphology being generalise by the patch approach. The averaged GI in patch and the chosen bulk urban parameter were employed to quantitatively evaluate the gusts event in an urban area. An optimum patch size relative to the whole domain size was examined to obtain the general and robust relationship. This assessment also extended for the mean wind ratio (MWR) and turbulent part ratio (TPR) for more comprehensive knowledge on the GI. Meteorologically, the consequence of the boundary layer development on the GI and its components also inspected. Furthermore, the GI and its components at the ground level (i.e.; 2 m) studied and compared with the statistics at the upper layer (i.e.; surface layer).

7.2 Determination of the Optimum Size of Patches

Takebayashi and Oku (2014) introduced a grid-partitioning method to determine the general relationship between the MWR and gross characteristics of city morphology. In this method, the horizontal domain is divided into homogeneous patch areas, and the area average of mean wind velocity is calculated for each patch for comparison with the gross building parameters in the same patch. They found a clear relationship between λ_p and MWR. This method also applied in this study to evaluate the GI and TPR as well as the MWR for different values of λ_p. The whole simulation domain used was divided into homogeneous square patches of several sizes, ranging from 80 to 2400 m per side. The GI, MWR and TPR in each patch were averaged and λ_p was also calculated. Although other urban parameters including λ_f were also examined, the results shown and discussed here focus only on λ_p because gusts at the pedestrian level had the best correlation with this parameter at the patch scales of interest. However, in the context of the height dependency of gust behaviour, roughness length (z_0) is also examined in sect. 7.5.

Figure 7.1 shows the relationship between these wind components and λ_p for all patch sizes, which was averaged again for 0.02 bin increments of the λ_p. Again, this figure focuses only on the latter half of the domain to avoid the influence of boundary layer development and to clarify the relationship with the building geometry, and also only considers up to λ_p = 0.5. The adequacy of limiting the analysis to the latter half of the domain is examined in sect. 7.3. Figure 7.1 shows a clear relationship between each normalised velocity ratio and λ_p. The distributions are scattered when the λ_p is less than 0.28 but are almost linear for all patch sizes when the λ_p is greater than 0.28.

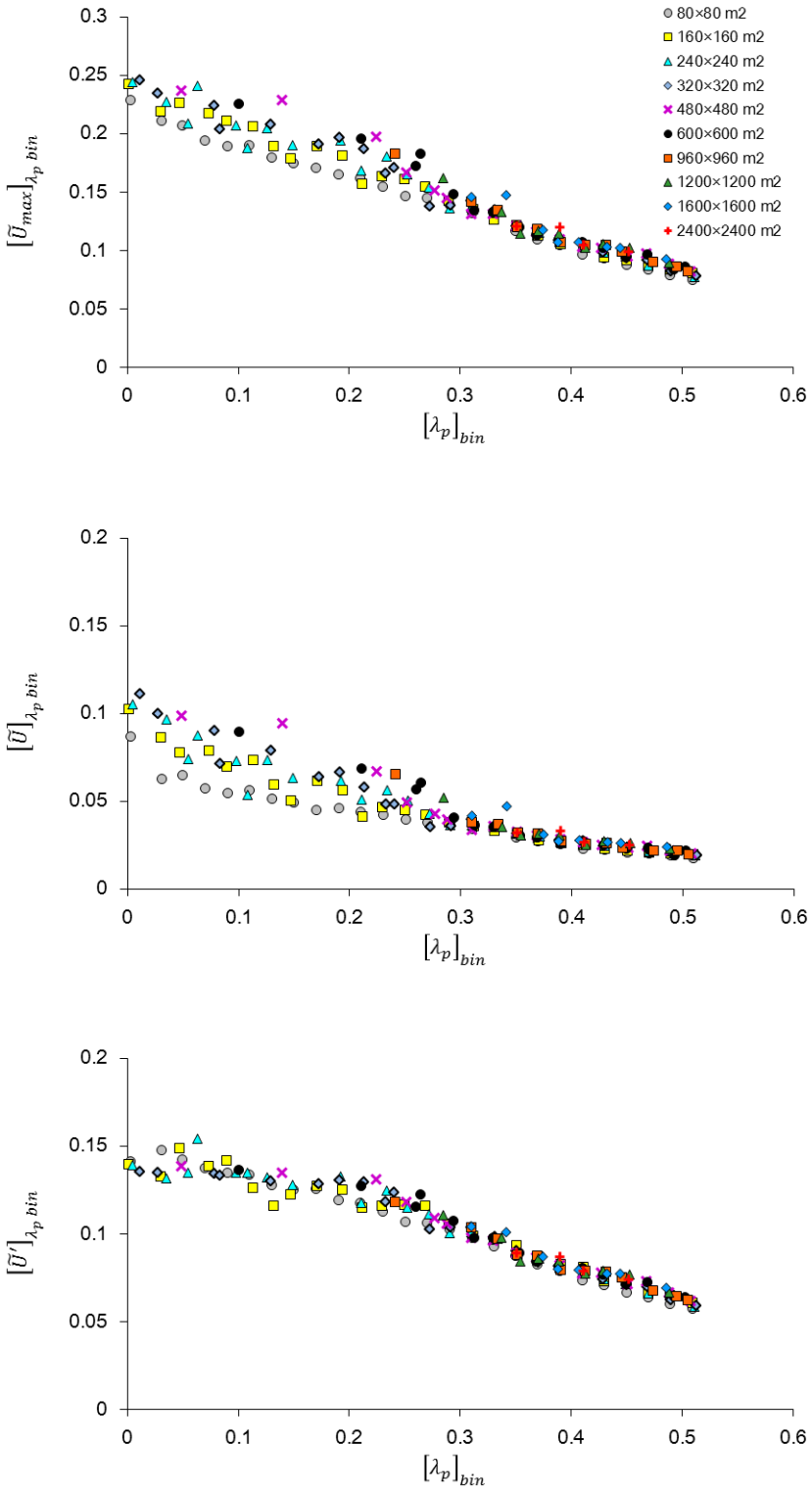

Figure 7.1 The bin analysis of the spatial average of the different patch sizes of the (a) gust index, $[\widetilde{U}_{max}]_{\lambda_p\ bin}$, (b) mean wind speed ratio, $[\widetilde{U}]_{\lambda_p\ bin}$, and (c) turbulent part ratio, $[\widetilde{U}']_{\lambda_p\ bin}$, versus the plan area index, $[\lambda_p]_{bin}$, at 2 m height for the latter half of the simulation domain.

An optimum patch size needs to be recognised to determine the general and robust relationship between the wind component and the bulk building parameter. If the patch size is too small, fine and specific morphological information (e.g., street width) becomes more important than the mean characteristics of the gross area (Takebayashi and Oku 2014). A patch area that is too large decreases the number of samples required to obtain statistically robust results in a domain of limited size. Therefore, the scatter of variables in a bin of λ_p was evaluated to determine how the variable (e.g.; GI, MWR and TPR) is relevant to λ_p, and to find a minimum threshold value of patch size.

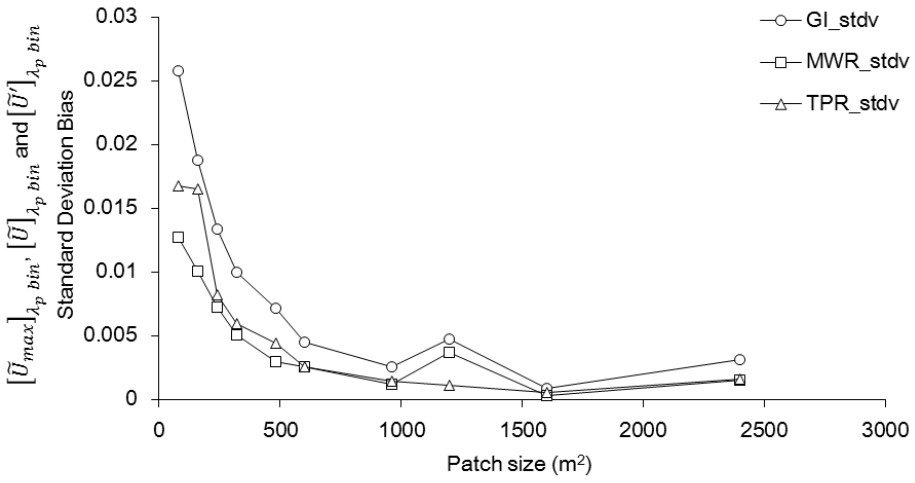

Figure 7.2 Standard deviation bias analysis of the different patch sizes (m^2) from the gust index, $[\widetilde{U}_{max}]_{\lambda_p\ bin}$, mean wind speed ratio, $[\widetilde{U}]_{\lambda_p\ bin}$, and turbulent part ratio, $[\widetilde{U'}]_{\lambda_p\ bin}$.

Figure 7.2 shows the bias of the standard deviation of each non-dimensional velocity component plotted for all patch size candidates. A patch size bigger than 480 × 480 m^2 seem to be insensitive to the variance of each normalised velocity ratio. Therefore, this optimum patch size was used in the analyses.

7.3 Influence of Boundary Layer Development on the Normalised Velocity Ratios

Next, the large GI near the inlet, which depended on the boundary layer height (δ) (Fig. 6.13 of Chapter 6) was evaluated. The δ is the distance normal from the ground surface to the height where $U = 0.99U_\infty$. On average, δ_1 = 105 m, δ_2 = 238 m, δ_3 = 346 m and δ_4 = 442 m for the first quarter (Q1) to the fourth quarter (Q4) as in Figure 7.3, respectively. Figure 7.4 shows the spatial and bin average of the GI, MWR and TPR plotted on λ_p with different colours for the different areas, which are quarters of the entire domain separated along *x*, in the order of Q1 as the inlet and Q4 as the outlet. The value of each normalised velocity ratio at Q1 was larger than for the other quarters at the same λ_p. The values for Q2 were slightly larger than for Q3 and Q4 which were almost the same. It was confirmed that the choice of the second half of the domain for the analysis was suitable to discuss the effect of the surface geometry. It was free from the effects of boundary layer development, which was dependent on the inflow settings. In addition, the values in Q2 and Q3 were equivalent when λ_p was smaller than 0.24. Therefore, the values for Q2 were used to cover the small sampling numbers for the low λ_p values in the latter half of the domain, which are discussed in the following sections.

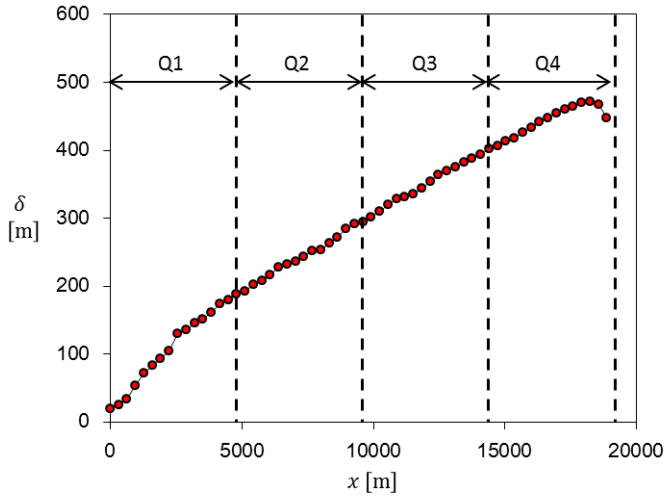

Figure 7.3 The boundary layer development along streamwise, *x*. Also shown the quarters distance from the domain inlet (Q1) to the outlet (Q4).

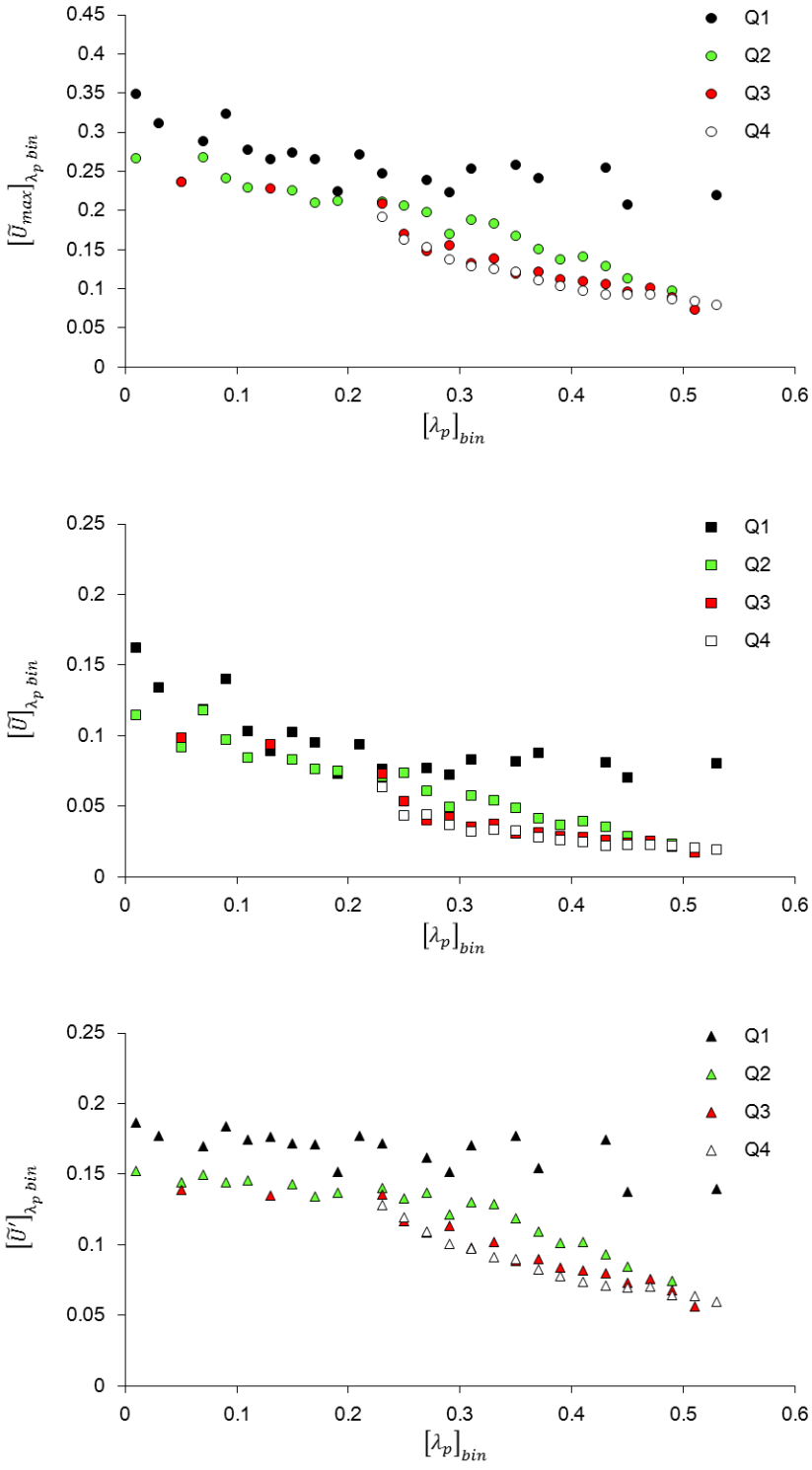

Figure 7.4 The spatial and bin average of the 480 × 480 m^2 patches for the gust index, $[\widetilde{U}_{max}]_{\lambda_p\ bin}$, mean wind speed ratio $[\widetilde{U}]_{\lambda_p\ bin}$, and turbulent part ratio, $[\widetilde{U}']_{\lambda_p\ bin}$ versus the plan area index, $[\lambda_p]_{bin}$, at 2 m for the whole domain divided into four quarter in the streamwise direction.

The physical interpretation of the effects of boundary layer height was considered on each normalised velocity ratio. The wind speed drastically increased in the direction normal from the ground when the boundary layer height was low, and high-speed gusts easily approached the ground level as noted previously. When a boundary layer is high enough, the flow field within a built-up area is mostly controlled by the surface roughness, which in this case was determined by the building morphology, because the vertical wind speed distribution follows a logarithmic profile. The rate of development became milder with distance in the *x*-direction, and its effect became harder to recognise.

Figure 7.5 shows the distribution spatial average of the 480 × 480 m^2 patches (not average in bin) for the last three quarters (Q2+Q3+Q4). There were several isolated plots scattered away from the linear trendline. Therefore, patches within $0.415< \lambda_p <0.432$ range were chosen in examine the boundary layer height effects on the higher values of the GI (red circle) compared to the plots closer to the line (green circle).

It was confirmed visually in Fig. 7.6 that those patches with higher GI laid on Q2 (i.e.; patch number 15, 91 and 330; refer to App. A8) while the other selected patches were distributed within the latter half domain (Q3+Q4). As explained above, the boundary layer height is still low in the former half domain, which contributed on the high GI within this area although the λ_p of the patches were in the same range with those in the latter half. Moreover, the patches with higher GI also have shown a significant building geometry (i.e.; building form and height), the arrangement and large open spaces. Further examination on these characteristics will be done in Sec. 7.4.

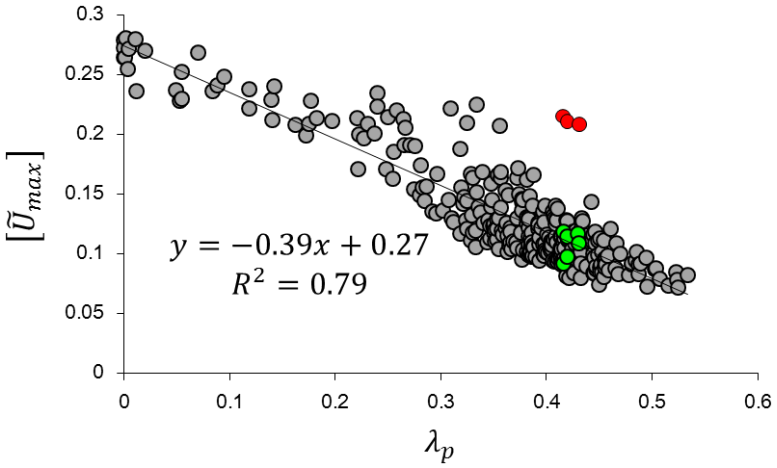

Figure 7.5 The spatial average of the 480 × 480 m^2 patches for the gust index, $[\tilde{U}_{max}]$ versus the plan area index, λ_p, at 2 m for the last three quarters (Q2+Q3+Q4). Chosen isolated scatter plots (red circle) and closed to linear trendline (green circle) were 0.415< λ_p<0.432.

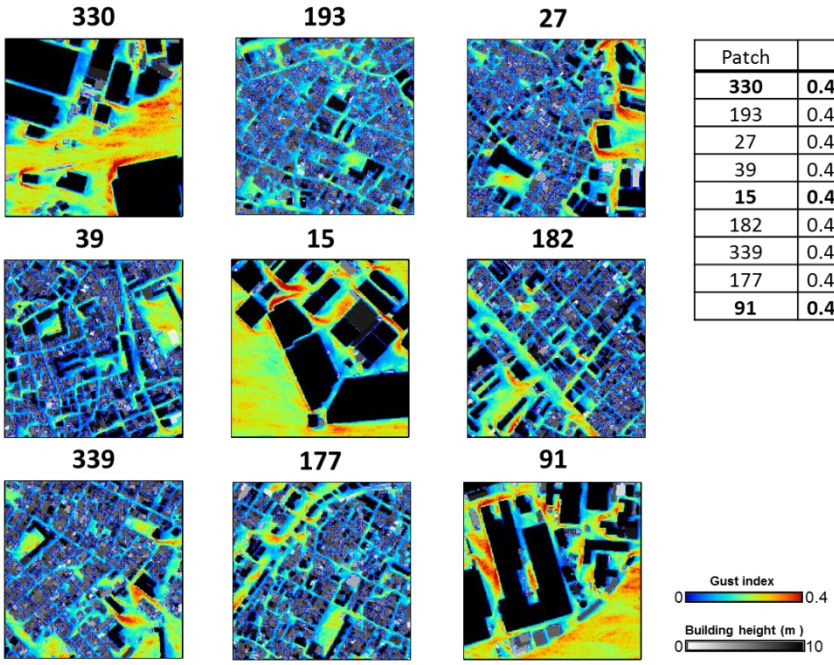

Patch	λ_p	$[\tilde{U}_{max}]$
330	**0.415382**	**0.215175**
193	0.415781	0.091679
27	0.415903	0.118543
39	0.419462	0.097692
15	**0.419601**	**0.210647**
182	0.420000	0.114349
339	0.429323	0.117017
177	0.430625	0.108534
91	**0.431007**	**0.208445**

Figure 7.6 Selected 480 × 480 m^2 patches of Fig. 7.5 and its corresponding plan area index, λ_p and gust index, $[\tilde{U}_{max}]$. Isolated scatter plot (Patch 15, 91 and 330) and closed to linear trendline (others).

7.4 General Relationship between Pedestrian-level Flow Characteristics and the Plan Area Index, λ_p

Figure 7.7 shows the spatial average of the 480 × 480 m square patches of the GI, MWR and TPR, with an average bin increment of λ_p = 0.02 for the last three quarters, which were 4.8~19.2 km from the domain inlet (Q2 + Q3 + Q4) and the latter half of the domain (Q3 + Q4). Instead of only the latter half of the domain, the last three quarters were also needed to increase the number of samples, particularly for the lower λ_p. Because the boundary layer height was still low at around 4.8 km from the domain inlet, the last three quarters had a slight positive bias from the latter half of the domain at higher λ_p but the two regions were almost consistent in the lower λ_p.

As shown in Fig. 7.7, all of the normalised velocity ratios decreased monotonically with increasing λ_p, and the TPR profile was always dominant compared to the MWR for all λ_p values. This means that intermittent gusty events were important for producing the maximum wind speed at the pedestrian level, and were milder in the built-up area than in the open area.

Another important feature shown in this figure is the ‘kink’ (refer to App. A9 and A10) in the profile of each normalised velocity ratio at around 0.28. The MWR decreased steeply at lower values, but was almost constant at higher ones. The TPR was almost constant at lower values but decreased at higher ones. The GI decreased almost linearly because it is the sum of the MWR and TPR. These features are described in Table 1, which shows the gradient of the lines when λ_p is smaller or larger than 0.28. Takebayashi and Oku (2014) found a similar kink in the profile of MWR at almost the same λ_p in their numerical simulation.

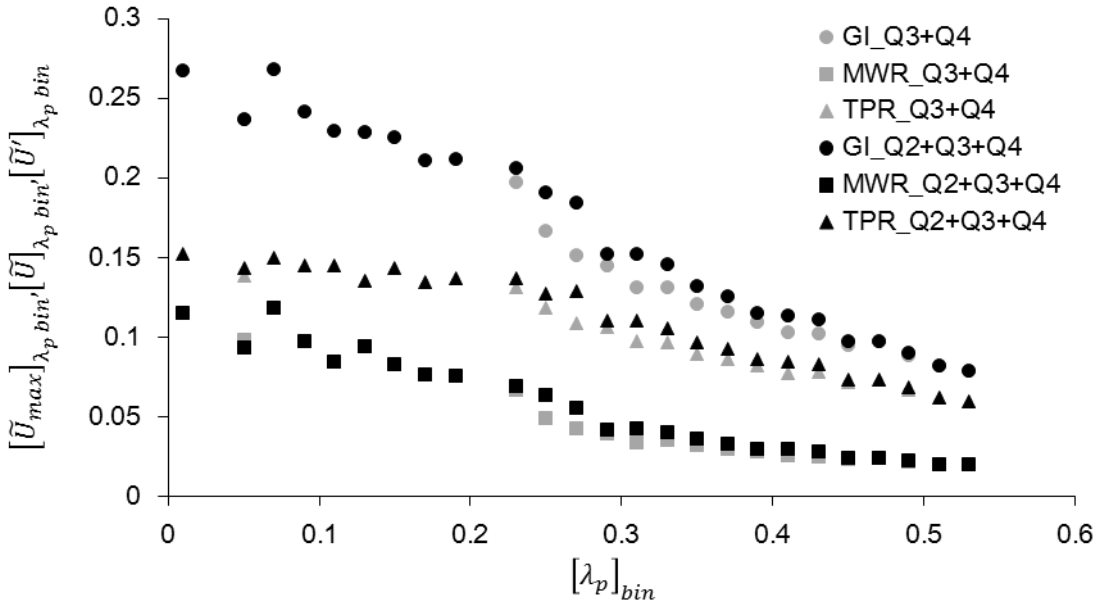

Figure 7.7 The spatial and bin average of the 480 × 480 m^2 patches for the gust index, $[\widetilde{U}_{max}]_{\lambda_p\ bin}$, mean wind speed ratio, $[\widetilde{U}]_{\lambda_p\ bin}$, and turbulent part ratio, $[\widetilde{U}']_{\lambda_p\ bin}$, versus the plan area index, $[\lambda_P]_{bin}$, at 2 m for the last three quarters from the domain inlet (Q2 + Q3 + Q4) and the latter of the half domain (Q3 + Q4).

Table 7.1 The gradient, m, of the mean wind speed ratio, $[\widetilde{U}]$, and the turbulent part ratio, $[\widetilde{U}']$, for plan area indices < 0.28 and > 0.28 from selected patches of Fig. 7.7.

$[\lambda_p]$	MWR	TPR
$[\lambda_p]$ < 0.28	-0.2512	-0.1048
$[\lambda_p]$ > 0.28	-0.0631	-0.1354

This could be explained by following the flow regime classification within the building canopy (Oke 1987). In the isolated flow regime (when λ_p < 0.28), the MWR depends simply on the building cover, because each obstacle individually imposes drag on the flow within the canopy. Obstacles can also efficiently generate turbulence fluctuations, which result in a constant TPR for an increasing λ_p in this flow regime. In the skimming flow regime (λ_p > 0.28), the mean flow in the canopy layer is decoupled from the upper layer. This produces a very small MWR and also keeps the spatial variation small because the MWR is small everywhere, resulting in little variation in the MWR with increasing λ_p. For the TPR, the size of turbulent eddies are limited by the horizontal size of the narrow open spaces. This accounts for the decreasing TPR with increasing λ_p. The decrease in TPR may also be caused by the flow in the canopy layer becoming decoupled from the turbulent structures above it in the skimming flow regime (e.g.; Inagaki et al. 2012). Although separate discussions have been conducted for individual flow regimes, real cities include open spaces of various sizes, with a mixture of different flow regimes in an averaging domain. Therefore, the relative contribution of the flow regimes, which is represented by λ_p in the current analysis, is also relevant to the variation in each normalised velocity ratio.

Zaki et al. (2011) indicated that the relationship between the drag coefficient and λ_p changes depending on the variation in the height of building roughness because the skimming flow regime becomes less representative in such cases. This is because the drag coefficient is relevant to the flow around the upper part of tall buildings (e.g.; Xie et al. 2008; Nakayama et al. 2011; Kanda et al. 2013), which are usually isolated from each other. However, flow near the ground is still strongly influenced by the surrounding small buildings. Then, λ_p becomes the most important parameter to consider the flow structure near the ground within the building canopy, and the consideration of flow regimes (Oke 1987) is still useful for analysing the flow properties in the three-dimensionally complex building canopies of real cities, based on morphological information.

Figure 7.8 shows several isolated plots were scattered away from the distribution that collapsed near the linear line although their λ_p were in the same range. Therefore, the features of those patches were examined visually as shown in Fig. 7.9 to investigate the basis of the deviation. The plots and patches of Fig. 7.8 and 7.9 were only from the latter half domain to exclude the influence of the boundary layer height on the GI distribution. At a glance, the patches with higher GI compared with the one nearer to the linear line in its own λ_p range have a similarity in the building configurations as mentioned previously in Sec. 7.3. Briefly, the patches with locally huge in volume (i.e.; large and tall buildings) will have higher GI compared to the area which enclosed with small and low rise buildings. Moreover, the surrounding open spaces also became an essential indication in contributing higher GI compared to the area where the buildings were evenly distributed. These possibilities might also important in determining the local instantaneous maximum wind speed, U_{max}, for the gusts alert system as shown in Fig. 1.2 and potentially analyse in detail for the future works.

7.5 The Gust Index and its Component at Different Heights

A distinct relationship between each normalised velocity ratio and the λ_p at the pedestrian level was described in the previous section by mainly following the procedure introduced by Takebayashi and Oku (2014). A comprehensive review of urban microclimate studies (e.g.; Roth 2000) indicated that the roughness length parameter best represents the aerodynamic properties of building roughness and effectively reproduces the turbulence statistics above the roughness sublayer in cities. Therefore, the relevance of each normalised velocity ratio on z_0 together with λ_p at the pedestrian level was briefly evaluated. Also, the manner of the relationship changes transiently to follow a similarity law in the surface layer with increasing elevation was been identified.

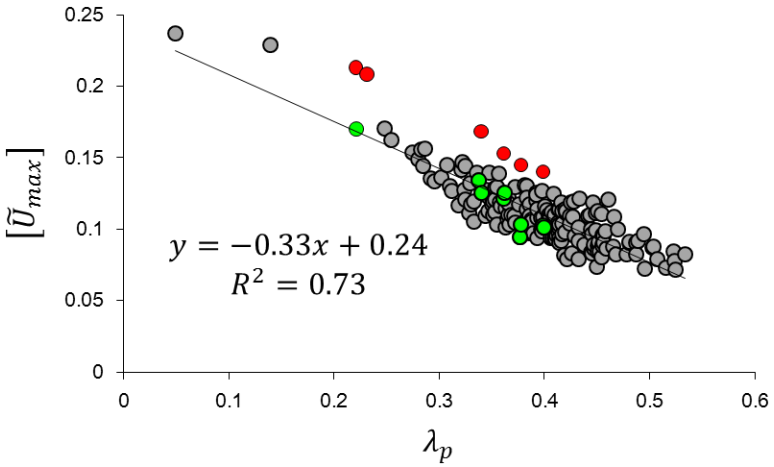

Figure 7.8 Same as Fig. 7.5 but only for the latter half domain (Q3+Q4).

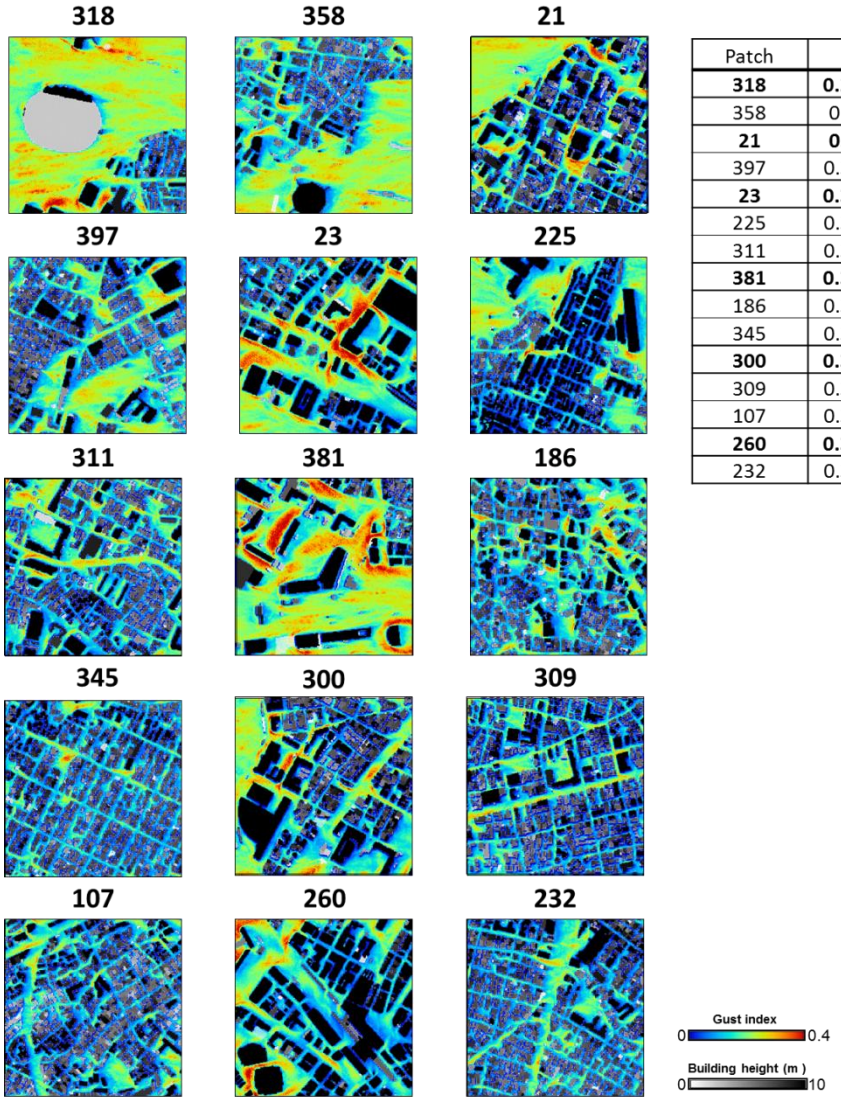

Patch	λ_p	$[\tilde{U}_{max}]$
318	**0.220486**	**0.213162**
358	0.22125	0.170322
21	**0.23092**	**0.208507**
397	0.337587	0.134085
23	**0.339635**	**0.168392**
225	0.340503	0.125192
311	0.361215	0.12177
381	**0.361302**	**0.152911**
186	0.362153	0.125646
345	0.376840	0.094656
300	**0.377639**	**0.145045**
309	0.377969	0.103291
107	0.398455	0.102962
260	**0.398698**	**0.140309**
232	0.399167	0.101197

Figure 7.9 Selected 480 × 480 m^2 patches of Fig. 7.8 and its corresponding plan area index, λ_p and gust index, $[\tilde{U}_{max}]$. Isolated scatter plot (Patch 21, 23, 260, 300, 318 and 381) and closed to linear trendline (others).

Figure 7.10 shows a comparison of the GI, MWR, TPR, λ_p and z_0 at the pedestrian level (i.e.; 2 m) and 16 m height for the last two quarters. The height of 16 m is the level where the average TPR is at a maximum above the canopy layer. A modified Macdonald equation from Kanda et al. (2013) was used to calculate the z_0 in which the frontal area index, λ_f, the average, H_{ave}, and standard deviation, σ_H, of building heights, and the maximum building height, H_{max}, in patch domains were considered in addition to λ_p.

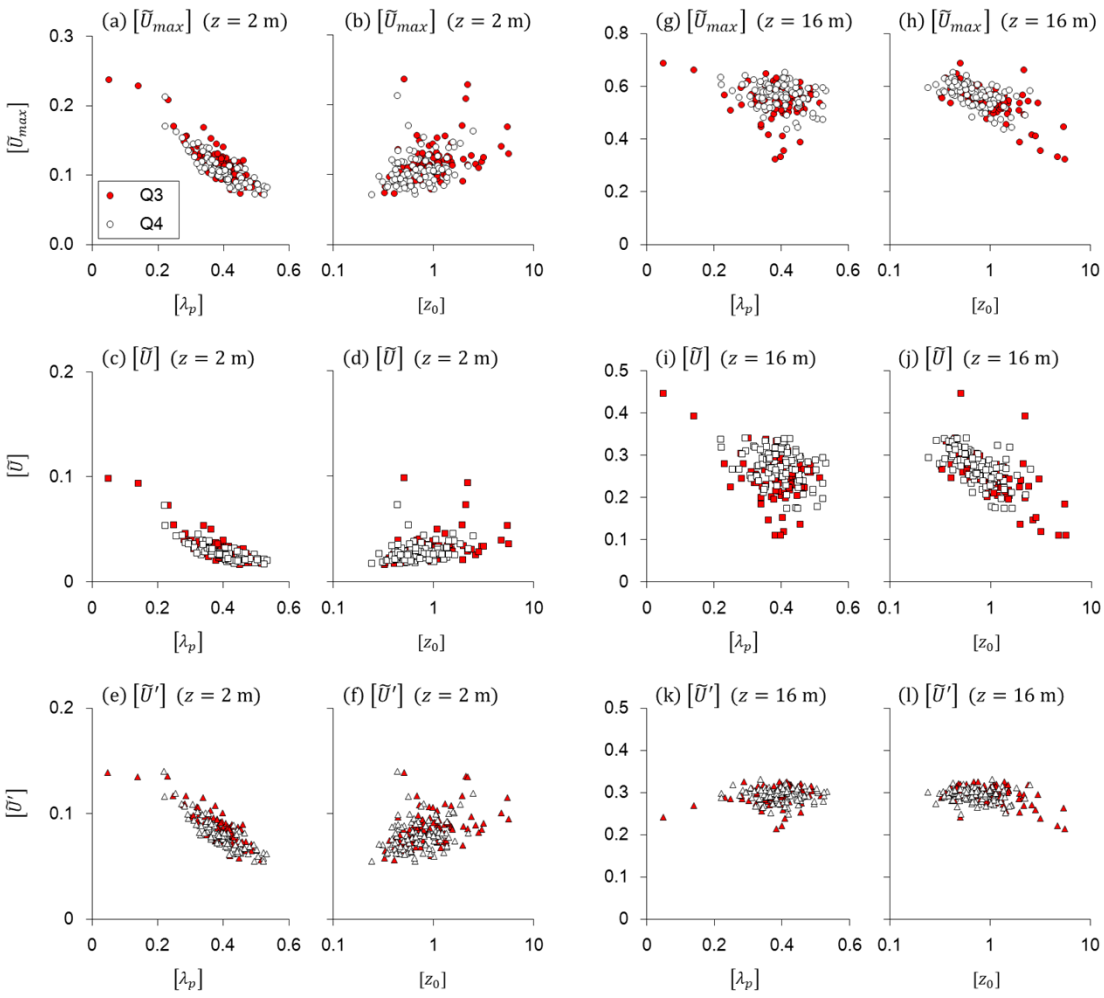

Figure 7.10 The gust index, $[\tilde{U}_{max}]$, mean wind speed ratio, $[\tilde{U}]$, and turbulent part ratio, $[\tilde{U}']$, versus the plan area index, $[\lambda_p]$, and the roughness length, $[z_0]$ in the 480 × 480 m^2 patches at a height of 2 and 16 m for the latter half of the domain (Q3 + Q4).

Although the TPR was larger than the MWR in the bottom layer as seen previously (see, Fig. 7.10c-f), the contribution of MWR overcame that of the TPR at the higher level (see, Fig. 7.10i-l) because the increasing rate of turbulent intensity with increasing height was zero near this level (not shown). In addition, the mean wind speed increased logarithmically with increasing height up to the top of the boundary layer. At the pedestrian level, the plots of all normalised velocity ratios were more concentrated and showed a clearer dependence on λ_p than z_0. At 16 m from the ground, all normalised velocity ratios depended more on z_0 than on λ_p. This implies that λ_p is sufficient to comprehensively represent the wind flow characteristics at the ground level while z_0 is more representative in the upper layer, as seen in Roth (2000).

The velocity factors had less of an effect on z_0 at the pedestrian level because the magnitude of z_0 was mainly accounted for by the taller buildings and drag coefficient, while the smaller buildings could be mostly neglected, although they still determine the velocity factors at this level as seen in the previous section. At the higher levels, the flow structures were mainly configured by taller buildings where z_0, as a comprehensive aerodynamic parameter, was more relevant than λ_p.

7.6 Summary

From this chapter, a bulk relationship between the gust index GI that averaged in a square patch (i.e.; 480 × 480 m^2) and the plan area index that represents the urban parameter had been examined. It is quantitatively revealed that low boundary layer height enhances GI near the domain inlet, mainly owing to the turbulent component gathered from a large vertical gradient of mean wind velocity. It was found that when air velocity is high, it can easily impinge the layer near to the ground. It was also shown that the GI monotonically decreases with increasing building area coverage. Although this characteristic is seen in area-averaged quantities, it is still not obvious

the locally maximum GI in an area, which is highly related to the shapes of individual buildings, also decrease simply with increasing building coverage. There are clear gradient deflections in the profiles of MWR and TPR along λ_p range. At the lower λ_p, MWR decrease and TPR is constant with increasing λ_p. Meanwhile, MWR is almost constant and TPR decrease with increasing λ_p at higher λ_p. These tendencies are explained by the regime shift of the flow in canopy layer. Considering the wind flow attribute at the higher level, its structures are majorly configured by taller buildings where z_0, as an aerodynamic parameter, becomes a relevant parameter than λ_p.

CHAPTER 8

CONCLUDING REMARKS

8.1 Introduction

This chapter will summarize all the work done and conclude the findings in this research. In the nutshell, the final aim of this study was successfully achieved by executing the large eddy simulation models which output a rich three dimensional dataset. The novelty was contributed by a general relationship between the intensity of gust and the urban morphology. Many more features need to be considered for the prospective work in order to comprehensively evaluate the gust occurrence within a build up area yet keep the feasibility of the study.

8.2 Research Findings

The gust characteristic within an urban canopy was examined by executing the large eddy simulation models. To generalize the discussion, followings are the major findings of this research.

1. A new indicator namely the gust index (GI) was defined as the local instantaneous maximum wind speed normalized by the free stream velocity. This spatial GI encounters the locality limitation of the conventional gust factor, G. The proposed GI was justified using the probability distribution function (PDF).
2. Besides the parallelized large eddy simulation (LES) model (PALM), another sophisticated large eddy simulation of the lattice Boltzmann method (LBM) was feasible to be executed over a huge domain with 2 m resolution due to the recent progress in supercomputers.
3. Two different large eddy simulation models applied at different stages of this research. After the results produced by these two models had been validated, the study suggests that results (from these two models) were of the same accuracy.
4. The reliability of the LBM simulation outcomes inspected from the streamwise and vertical profiles of the flow field and confirmed by the theoretical and experimental results of previous study.
5. The horizontal distributions of the flow field at different height also presented in order to examine the compatibility of the simulation and gain thorough understanding.
6. The GI distribution map was capable to be plotted and visually examined to get the first insight of the gusts in the build up area at any locations and height within the domain range.
7. The gustiness quality was measured by break down the GI into its components which is the mean wind ratio (MWR) and the turbulent part ratio (TPR).
8. Quantitatively, the GI and its components and also the urban parameter that averaged in a square patch, is proposed as a general quantity to compare among different locations and experiments in urban canopy. By applying this patch approach, a framework to generalise the relationship between the gusts and the urban parameter was systematically constructed.

9. It was revealed that low boundary layer height enhances GI near the domain inlet, which is mostly owing to the turbulent component. This is due to the large vertical gradient of mean wind velocity in which higher velocity air can easily impinge on to the layer closer to the pedestrian / ground level.
10. It is also shown that the GI monotonically decreases with increasing building area coverage, λ_p. There are clear bend in the profiles gradient of MWR and TPR along λ_p range. At the lower λ_p, MWR decrease and TPR is constant with increasing λ_p. Meanwhile, MWR is almost constant and TPR decrease at higher λ_p. These tendencies are explained by the regime shift of the flow in canopy layer.
11. Considering the meteorological approach of the wind flow attribute at the higher level, its structures are majorly configured by taller buildings where the roughness length, z_0, becomes a relevant parameter than λ_p. Vice versa, component ratios are densely concentrated and show clearer dependence on λ_p at the pedestrian level.
12. This research initiate an adjoin of two main streams of the gusts in urban area where one of it is focusing on the influence of detail structures of individual buildings, and the other is based on the knowledge of the similarity law such as the Monin-Obukhov similarity or its modification to the roughness sublayer.

8.3 Recommendations and Implications for Further Research

For further scientific understanding, the following are recommended to be investigated in the future works.

1. Several megacities chosen as the simulation domain with an acceptable domain size and sufficient range of the urban morphological parameter. Wind statistics from these megacities can be compared to confirm the relationship between the GI and the chosen urban parameter is universal and robust.

2. Instead of the urban parameter presented in this research, more urban geometrical and aerodynamics parameters can be considered to present the general relationship between the GI and the urban morphology.
3. Different directions of the input wind of certain simulation domain can be tested. The gust index performance can be examined on the wind direction dependence parameter such as the frontal area index, λ_f.
4. Besides the building heights, this research involved only flat domain bottom surface. Therefore, it can be enhanced with the ground topography for more realistic outcomes.
5. As this research was restricted to neutral stratification, the buoyancy effect could be added in the simulation condition from which the difference in the induced gusts could be compared.
6. The comparative study was limited mainly to the numerical simulation output. It would be interesting to measure the maximum instantaneous wind speed within the real urban model by using the wind tunnel experiment or field measurement (i.e. Doppler lidar). It is also suggested that the measurement points and locations representing the flow characteristics of an area should be considered.
7. The results from this gusts study can be utilised in developing the gusts alert system as shown in Fig. 1.2. The mesoscale weather prediction can provide the information about the strong wind speed. Referring to the robust general relationship of the GI and the urban bulk parameter, the expected distribution of the GI in an area can be determined. This estimation is feasible because the GI is a scalable parameter and its probability distribution function was independent with the inflow setting as mentioned in Sec. 4.3.

8.4 Summary

Finally, by conducting this research the queries of the overlying problems clarified at this moment. Improved outcomes are expected in near future by considering the listed recommendations.

REFERENCES

Azad AK, Alam MM (2010) Determination of Wind Gust Factor at Windy Areas of Bangladesh. In 13th Asian Congress of Fluid Mechanics, 17-21 December, 2010, IUT, Dhaka, Bangladesh, pp 521-524

Bernaschi M, Fatica M, Melchionna S, Succi S, Kaxiras E (2010) A flexible high-performance Lattice Boltzmann GPU code for the simulations of fluid flows in complex geometries. Concurrency and Computation: Practice and Experience 22(1):1-14

Castillo MC, Inagaki A, Kanda M (2011) The effects of inner-and outer-layer turbulence in a convective boundary layer on the near-neutral inertial sublayer over an urban-like surface. Boundary-Layer Meteorol 140(3):453-469

Cheng H, Castro IP (2002) Near wall flow over urban - like roughness. Boundary-Layer Meteorol 104(2):229-259

Coceal O, Belcher SE (2004) A canopy model of mean winds through urban areas. Q J R Meteorol Soc 130(599):1349-1372

Davis FK, Newstein H (1968) The variation of gust factors with mean wind speed and with height. J App Meteorol 7(3):372-378

Garratt JR (1990). The internal boundary layer - a review. Boundary-Layer Meteorol 50(1-4):171-203

Gust. Retreived from http://www.merriam-webster.com/dictionary/gust

He J, Song CCS (1999) Evaluation of pedestrian winds in urban area by numerical approach. J Wind Eng 81:295-309

He X, Zou Q, Luo LS, Dembo M (1997) Analytic solutions of simple flows and analysis of nonslip boundary conditions for the lattice Boltzmann BGK model. J Stat Phys 87(1-2):115-136

Hou S, Sterling J, Chen S, Doolen GD (1994) A lattice Boltzmann subgrid model for high Reynolds number flows. arXiv preprint comp-gas/9401004

Hu T, Yoshie R (2013) Indices to evaluate ventilation efficiency in newly-built urban area at pedestrian level. J Wind Eng Ind Aerodyn 112:39-51

Huda AN, Inagaki A, Kanda M, Onodera N, Aoki T (2015) Large eddy simulation of the gust index in an urban area using the lattice Boltzmann method. Boundary-Layer Meteorol (Under review)

Huda AN, Inagaki A, Kanda M, Onodera N, Aoki T (2015) Spatial distribution of the gust index over an urban area in Tokyo. Proceedings of the 9th International Conference on Urban Climate jointly with 12th Symposium on the Urban Environment, 20-24 July, 2015, Toulouse, France

Huda AN, Inagaki A, Kanda M, Onodera N, Aoki T (2015) Large eddy simulation of the gust factor using lattice Boltzmann method within a huge and high resolution urban area of Tokyo. J Japan Society of Civil Engineers, Ser. B1(Hydraulic Engineering) 71(4):I_37-I_42

Huda AN, Inagaki A, Kanda M, Onodera N, Aoki T (2014) A Huge and high resolution large eddy simulation domain of Tokyo urban area by using lattice Boltzmann method. Proceedings of the Academy for Co-creative Education of Environment and Energy Science, 12-16 December, 2014, Perth, Western Australia, Australia

Huda AN, Inagaki A, Kanda M, Onodera N, Aoki T (2014) Simulation of the gust factor in highly dense urban area in Tokyo. Proceedings of the 1st International Conference on Computational Engineering and Science for Safety and Environmental Problems, 13-16 April, 2014, SIC, Sendai, Japan, pp 718-72

Inagaki A, Castillo MCL, Yamashita Y, Kanda M, Takimoto H (2012) Large-eddy simulation of coherent flow structures within a cubical canopy. Boundary-Layer Meteorol 142(2):207-222

Japan Meteorological Agency (JMA), http://www.jma.go.jp/jma/index.html

Jiménez J (2004) Turbulent flows over rough walls. Annu Rev Fluid Mech 36;173-196

Kanda M (2006) Large-eddy simulations on the effects of surface geometry of building arrays on turbulent organized structures. Boundary-Layer Meteorol 118(1):151-168

Kanda M, Inagaki A, Miyamoto T, Gryschka M, Raasch S (2013) A New Aerodynamic Parametrization for Real Urban Surfaces. Boundary-Layer Meteorol 148(2):357-377

Kanda M, Moriwaki R, Kasamatsu F (2004) Large-eddy simulation of turbulent organized structures within and above explicitly resolved cube arrays. Boundary-Layer Meteorol 112(2):343-368

Keck M, Raasch S, Letzel MO, Ng E (2014) First Results of High Resolution Large-Eddy Simulations of the Atmospheric Boundary Layer. J Heat Island Inst Int 9(2):39-43

Kobayashi H, Ham F, Wu X (2008) Application of a local SGS model based on coherent structures to complex geometries. Int J Heat Fluid Flow 29(3):640-653

Kobayashi H (2006) Large eddy simulation of magnetohydrodynamic turbulent channel flows with local subgrid-scale model based on coherent structures. Phys Fluids (1994-present) 18(4):045107

Kubota T, Miura M, Tominaga Y, Mochida A (2008) Wind tunnel tests on the relationship between building density and pedestrian-level wind velocity: Development of guidelines for realizing acceptable wind environment in residential neighborhoods. Build Environ 43:1699-1708

Leonardi S, Castro IP (2010) Channel flow over large cube roughness: a direct numerical simulation study. J Fluid Mech 651:519-539

Letzel MO, Helmke C, Ng E, An X, Lai A, Raasch S (2012) LES case study on pedestrian level ventilation in two neighbourhoods in Hong Kong. Meteorol Z 21(6):575-589

Letzel MO, Krane M, Raasch S (2008) High resolution urban large-eddy simulation studies from street canyon to neighbourhood scale. Atmos Environ 42(38):8770-8784

Macdonald RW (2000) Modelling the mean velocity profile in the urban canopy layer. Boundary-Layer Meteorol 97(1):25-45

Martilli A, Clappier A, Rotach MW (2002) An urban surface exchange parameterisation for mesoscale models. Boundary-Layer Meteorol 104(2):261-304

Martinuzzi R, Tropea C (1993) The flow around surface-mounted, prismatic obstacles placed in a fully developed channel flow (Data Bank Contribution). J Fluids Eng 115(1):85-92

Monahan HH, Armendariz M (1971) Gust factor variations with height and atmospheric stability. J Geophys Res 76(24):5807-5818

Murakami S, Fujii K (1983) Turbulence characteristics of wind flow at ground level in built-up area. J Wind Eng Ind Aerodyn 15:133-144

Nakayama H, Takemi T, Nagai H (2011) LES analysis of the aerodynamic surface properties for turbulent flows over building arrays with various geometries. J App Meteorol Clim, 50(8):1692-1712

National Oceanic and Atmospheric Administration (NOAA), http://www.noaa.gov/

Oke TR (1987) Boundary layer climates. 2nd edn. Methuen, London 435 pp

Onodera N, Aoki T, Shimokawabe T, Kobayashi H (2013) Large-scale LES wind simulation using lattice Boltzmann method for a 10km × 10km area in metropolitan Tokyo. TSUBAME e-Science J Global Sci Inf Comput Cent 9:1-8

Park SB, Baik JJ, Han BS (2013) Large-eddy simulation of turbulent flow in a densely built-up urban area. Environ Fluid Mech 15(2):235-250

Raasch S, Schröter M (2001) PALM – A large-eddy simulation model performing on massively parallel computers. Meteorol Z 10:363-372

Raupach MR, Antonia RA, Rajagopalan S (1991). Rough-wall turbulent boundary layers. App Mech Rev 44(1):1-25

Razak AA, Hagishima A, Ikegaya N, Tanimoto J (2013) Analysis of airflow over building arrays for assessment of urban wind environment. Build Environ 59:56-65

Roth M (2000) Review of atmospheric turbulence over cities. Q J R Meteorol Soc 126(564):941-990

Takebayashi H, Oku K (2014) Study on the evaluation method of wind environment in the street canyon for the preparation of urban climate map. J Heat Island Inst Int 9(2):55-60

Verkaik JW (2000) Evaluation of two gustiness models for exposure correction calculations. J Appl Meteorol 39(9):1613-1626

Wieringa J (1973) Gust factors over open water and built-up country. Boundary-Layer Meteorol 3(4):424-441

Wilson DK (2000) The Role of Wind Gusts in the Near-Ground Atmosphere (No. ARL-TR-2290). Army Res Lab Adelphi MD 51 pp

Wind gust. Retreived from http://graphical.weather.gov/definitions/defineWindGust.html

Xie ZT, Coceal O, Castro IP (2008) Large-eddy simulation of flows over random urban-like obstacles. Boundary-Layer Meteorol 129(1):1-23

Yin X, Zhang J (2012) An improved bounce-back scheme for complex boundary conditions in lattice Boltzmann method. J Comput Phys 231(11):4295-4303

Yu H, Girimaji SS, Luo LS (2005) DNS and LES of decaying isotropic turbulence with and without frame rotation using lattice Boltzmann method. J Comput Phys 209(2):599–61

Zaki SA, Hagishima A, Tanimoto J, Ikegaya, N (2011) Aerodynamic parameters of urban building arrays with random geometries. Boundary-Layer Meteorol 138(1): 99-120

Zou Q, He X (1996) On pressure and velocity flow boundary conditions and bounce back for the lattice Boltzmann BGK model. eprint. arXiv preprint comp-gas/9611001

APPENDIX

Appendix A1 Tokyo meteorological station, retrieved from Japan Meteorological Agency (JMA).

Appendix A2 Tokyo wind yearly wind measurement, retrieved from Japan Meteorological Agency (JMA).

東京 年ごとの値 主な要素

年	風向・風速(m/s)				
	平均風速	最大風速		最大瞬間風速	
		風速	風向	風速	風向
1978	3.1	16.3	南南西	25.8	南南西
1979	3.4	17.5	南	38.2	南
1980	3.5	16.1	北北西	28.5	北北西
1981	3.3	16.5	北北西	28.8	北北東
1982	3.5	18.4	南	37	南
1983	3.5	14.4	北	28.2	北
1984	3.4	12.3	北北西	24.7	南西
1985	3.4	16.7	南	36.7	南
1986	3.5	13.8	北西	26.3	北西
1987	3.6	14	北北西	25.3	北北西
1988	3.6	14.5	北北西	26.4	北北西
1989	3.7	14.6	北北西	25.9	北北西
1990	3.6	14.4	南	30.8	南
1991	3.4	13.1	北西	26.9	南南西
1992	3.3	12.8	北	26.4	北北西
1993	3.3	15.5	北北西	30.6	北西
1994	3.3	12.3	北西	27.8	北西
1995	3.3	16	北	31.5	北
1996	3.3	17	北北西	36.1	北北西
1997	3.4	15.4	南西	29.5	南
1998	3.2	12.9	南西	29.2	南西
1999	3.3	13.9	北北西	29	北北西
2000	3.2	13.8	北西	26.7	北
2001	3.2	17.7	北東	34.1	北北東
2002	3.2	13.9	西	33.2	西北西
2003	3.1	11.4	北北西	26.8	南南西
2004	3.7	17.5	南西	40.2	南西
2005	3.4	13.4	北東	27.3	北北西
2006	3.4	13.5	北北西	33.4	北北西
2007	3.4	14.9	東南東	30.8	北北西
2008	2.8	14.2	北西	27.9	北西
2009	2.9	13.1	南	30.2	南
2010	2.9	14.6	南	29.2	南
2011	2.9	16.9	南	36	南
2012	3	16.3	南	32.7	南
2013	3.1	14.5	南南西	32.5	南
2014	2.9	11.8	南	25.8	南
2015	2.9]	11.0]	北北西	21.7]	南南西

赤線は、観測場所を移転した場合、観測装置を変更した場合または観測の時間間隔を変更した場合に、その前後のデータが均質でないことを示します。
http://www.data.jma.go.jp/obd/stats/etrn/view/annually_s.php?prec_no=44&block_no=47662&year=&month=&day=&view=

Appendix A3 Tokyo wind monthly wind measurement, retrieved from Japan Meteorological Agency (JMA).

東京 2014年（月ごとの値） 主な要素

月	風向・風速(m/s)				
	平均	最大風速		最大瞬間風速	
	風速	風速	風向	風速	風向
1	2.8	10.3	北西	22.1	北北西
2	3.3	11	北西	23.1	北西
3	3.5	11.8	南	24	南南東
4	3.1	9.9	北北西	19	北北西
5	3.4	11.3	北西	22.5	北西
6	2.6	7.4	南東	11.6	南南東
7	2.8	9.8	南	17.8	南
8	3.2	11.4	南	24.2	南
9	2.6	8.7	北北東	19	南
10	2.7	11.5	北西	25.8	南
11	2.5	7.5	北北西	15.9	北北西
12	2.5)	10.4)	西北西	16.8)	西北西

http://www.data.jma.go.jp/obd/stats/etrn/view/monthly_s1.php?prec_no=44&block_no=47662&year=2014&month=1&day=14&view=

Appendix A4 Tokyo wind daily wind measurement, retrieved from Japan Meteorological Agency (JMA).

東京 2015年1月（日ごとの値） 主な要素

日	風向・風速(m/s)				
	平均	最大風速		最大瞬間風速	
	風速	風速	風向	風速	風向
1	4.4	9.4	北西	18.7	北北西
2	2.1	4.2	北西	7.8	北西
3	3	7.4	西北西	10.9	西北西
4	1.3	2.8	西北西	3.8	北北東
5	2.4	5	北北西	9.1	北北西
6	5.2	8.9	南南西	19.3	南
7	4.2	7	北北西	16.1	北北西
8	4.4	8.4	北西	13.6	北北西
9	4.1	8.1	北西	14.4	北西
10	3.5	8.8	北西	17.7	北西
11	2.7	5.7	南南東	10	北北西
12	4.6	9.1	北西	15.8	北西
13	3.3	7.5	西北西	11.1	西北西
14	1.6)	3.5	北西	5.9	北西
15	3.2	8.1	北北西	14.1	北西
16	2.8	5.7	南東	10.7	西北西
17	4.2	9.4	北北西	19.1	北北西
18	3.3	6.4	北西	11.5	北北西
19	2.5)	5.7	北北西	10.2	北北西
20	3.6	6.8	北西	12.6	北西
21	3.1	5	北北西	9.3	北北西
22	2.4	5.2	北北西	9.1	北西
23	4.3	9.1	北北西	17.6	北
24	2.4	6.6	北	10.9	西北西
25	2	4.9	南東	8.2	南南東
26	2	3.8	南南東	6	南南東
27	3.1	6.3	北北西	12.1	北西
28	4	7.6	北北西	14.6	北北西
29	2.5	5.1	北北西	9.7	北西
30	3.3	5.5	北北西	11	北北西
31	4.4	10.5	北西	19.3	西北西

http://www.data.jma.go.jp/obd/stats/etrn/view/daily_s1.php?prec_no=44&block_no=47662&year=2015&month=1&day=&view=

Appendix A5 Tokyo wind 10 min wind measurement, retrieved from Japan Meteorological Agency (JMA).

東京 2015年1月14日（１０分ごとの値）

時分	風向・風速(m/s)			
	平均	風向	最大瞬間	風向
0:10	2.8	北北西	5.9	北西
0:20	2.9	北北西	5.1	北西
0:30	2	北北西	3.9	北
0:40	2.4	北北西	4.2	北
0:50	1.8	北西	3	北北西
1:00	2.4	北北西	4.4	北西
1:10	2.2	北北西	3.8	北西
1:20	2.2	北北西	4.2	北北西
1:30	1.7	北北西	3.4	北北西
1:40	0.9	北西	2.8	北
1:50	1.6	北北西	3.4	北西
2:00	1.8	北北西	3.9	北北西
2:10	1	北	2.9	北
2:20	1.9	北北西	3.6	北
2:30	1.6	北西	2.8	北西
2:40	1.5	北	3.2	北
2:50	2.1	北北西	4.2	北北西
3:00	2	北北西	4.3	北西
3:10	1.8	北北西	4	北北西
3:20	1.4	北	2.8	北北東
3:30	1.3	北北西	3.7	北北西
3:40	2.1	北北西	3.2	北
3:50	1.3	北北東	3	北北東
4:00	1.8	北東	3.2	北東
4:10	1.4	北北東	2.7	北北東
4:20	0.5	北北西	0.9	北北西
4:30	1.4	北北西	3.2	北北東
4:40	2	北北西	3.3	北北西
4:50	2.2	北西	3.6	北北西
5:00	1.6	北西	3.5	北西
5:10	2.3	北西	3.4	西北西
5:20	1.6	西北西	3.2	西北西
5:30	3.1	北西	4.5	北西
5:40	2.2	北西	4	北西
5:50	3.4	北西	4.9	北西
6:00	2.9	北西	4.9	北西
6:10	2	北北西	3.3	北西
6:20	1.4	北北西	3.1	北
6:30	1.3	北	3.5	北北西
6:40	2.1	北西	4.6	北北西
6:50	1.6	北西	2.9	北西
7:00	1.9	北西	3.2	西北西
7:10	2	北西	4	北西
7:20	2.1	西北西	3	西北西
7:30	2.7	北西	4.4	北西
7:40	2.6	西北西	4.3	西北西
7:50	2.1	西北西	3.3	西北西
8:00	2.1	西北西	3.2	西北西
8:10	2.3	北西	4.4	北西
8:20	2.6	北北西	4.4	北北西
8:30	1.6	北北西	2.9	北北西
8:40	1.8	北北西	3.4	北
8:50	1.5	北	3.5	北北西
9:00	2.5	北北西	4.5	北
9:10	2.6	北北西	4.8	北西
9:20	1.8	北西	2.9	北西
9:30	2.3	北西	4.1	北西
9:40	2	北西	4	西北西
9:50	1.5	北北西	2.9	西北西
10:00	1.1	北	2.5	北西
10:10	1.8	北西	3.3	北西
10:20	1.4	北東	3.2	北東
10:30	1.3	北東	3	東北東
10:40	1.7	北東	3.2	北東
10:50	2.4	北西	4.1	北西
11:00	1.7	北西	3.7	北北西
11:10	1.5	北北西	3.4	北北東
11:20	1.6	北東	2.9	北北東
11:30	1.2	北	2.8	北北西
11:40	1.6	北東	3.3	東
11:50	1.3	北	2.5	北北東
12:00	1.6	北東	2.9	北東

時分	風向・風速(m/s)			
	平均	風向	最大瞬間	風向
12:10	1.1	北北西	2.7	北北西
12:20	0.9	西南西	2	西南西
12:30	1.2	南南西	2.1	西南西
12:40	1.6	北北西	3.4	北北東
12:50	1.6	東北東	3.4	北北東
13:00	0.8	北	2.2	北北東
13:10	×	×	2.4]	北北東]
13:20	1.2	東	2.2	東北東
13:30	1.2	北北東	2.5	東北東
13:40	1.1	北東	2.3	東北東
13:50	1.6	東	3.7	東南東
14:00	2.1	東	3.8	東北東
14:10	1.7	北北東	3.6	北東
14:20	1.2	北北東	2.4	北
14:30	1.1	北	2	北
14:40	0.9	西北西	1.7	西
14:50	1	南西	1.8	南西
15:00	0.9	南南西	1.8	南南西
15:10	0.7	南南西	1.6	南西
15:20	1	南	2.1	南南東
15:30	1	南	1.5	南南西
15:40	1.4	南南東	2.1	南南東
15:50	1.5	南	2.2	南
16:00	1.4	南南東	2.4	南南東
16:10	1.4	南	2.5	南南東
16:20	1.1	南	1.9	南南東
16:30	0.7	南南東	1.1	南
16:40	0.9	南	1.4	南
16:50	0.5	南南東	0.9	北北東
17:00	0.5	北西	1.2	北北西
17:10	0.6	西南西	1.4	西南西
17:20	0.7	西南西	1.4	南西
17:30	0.3	西南西	0.8	南東
17:40	0.6	西南西	1	南
17:50	1.1	南南東	1.4	南南東
18:00	1	南	1.6	南南東
18:10	0.5	西北西	1	西南西
18:20	0.3	南南西	1	南西
18:30	0.4	南南東	0.9	南
18:40	0.7	西北西	1.2	北西
18:50	1.5	北北東	2.6	北北東
19:00	1.6	北北東	2.1	北北東
19:10	1.7	北	2.5	北北西
19:20	2	北北西	3.3	北北西
19:30	1.4	北	2.7	北北東
19:40	1.5	北	3.5	北北西
19:50	1.4	北	3.2	北北西
20:00	2.1	北北東	4.5	北北東
20:10	2.3	北北東	4.4	北北東
20:20	1.8	北	3.3	北北東
20:30	1.7	北北東	2.7	北北東
20:40	1.5	北	2.9	北北東
20:50	1.7	北北東	2.9	北北東
21:00	1	北北西	1.8	北西
21:10	1.3	北北東	2.9	北北東
21:20	1.7	北	2.7	北北東
21:30	1.5	北北西	2.5	北北西
21:40	1.4	北北西	2.5	北西
21:50	2.3	北西	3.1	西北西
22:00	1.3	北北西	2.3	北西
22:10	2	北北西	5.4	北西
22:20	2.5	北北西	3.9	北西
22:30	1.2	北西	2.5	北
22:40	1.7	北西	2.6	北西
22:50	2.1	北西	3.2	北北西
23:00	1.7	北北西	3	北
23:10	1.7	北	3.3	北
23:20	0.7	北	2.5	北北西
23:30	1.8	北北西	3.5	北北西
23:40	1.3	北北西	2.5	北西
23:50	1.8	西北西	3.8	北西
24:00:00	2	北北西	3.8	北

http://www.data.jma.go.jp/obd/stats/etrn/view/10min_s1.php?prec_no=44&block_no=47662&year=2015&month=1&day=14&view=

Appendix A6　リーフレット「雨と風（雨と風の階級表）」[Leaflet "Rain and wind (Class tables of rain and wind)"], retrieved from Japan Meteorological Agency (JMA).

風の強さと吹き方

（平成12年8月作成）（平成14年1月一部改正）
（平成19年4月一部改正）（平成25年3月一部改正）

平均風速（m/s）おおよその時速	風の強さ（予報用語）	速さの目安	人への影響	屋外・樹木の様子	走行中の車	建造物	おおよその瞬間風速（m/s）
10～15 ～約50km/h	やや強い風	一般道路の自動車	風に向かって歩きにくくなる。傘がさせない。	樹木全体が揺れ始める。電線が揺れ始める。	道路の吹流しの角度が水平になり、高速運転中では横風に流される感覚を受ける。	樋(とい)が揺れ始める。	20
15～20 ～約70km/h	強い風		風に向かって歩けなくなり、転倒する人も出る。高所での作業はきわめて危険。	電線が鳴り始める。看板やトタン板が外れ始める。	高速運転中では、横風に流される感覚が大きくなる。	屋根瓦・屋根葺材がはがれるものがある。雨戸やシャッターが揺れる。	
20～25 ～約90km/h	非常に強い風	高速道路の自動車	何かにつかまっていないと立っていられない。飛来物によって負傷するおそれがある。	細い木の幹が折れたり、根の張っていない木が倒れ始める。看板が落下・飛散する。道路標識が傾く。	通常の速度で運転するのが困難になる。	屋根瓦・屋根葺材が飛散するものがある。固定されていないプレハブ小屋が移動、転倒する。ビニールハウスのフィルム（被覆材）が広範囲に破れる。	30
25～30 ～約110km/h							40
30～35 ～約125km/h	猛烈な風	特急電車	屋外での行動は極めて危険。	多くの樹木が倒れる。電柱や街灯で倒れるものがある。ブロック塀で倒壊するものがある。	走行中のトラックが横転する。	窯業系サイディングの一部がはがれ、下地材が露出するものがある。	50
35～40 ～約140km/h							60
40～ 約140km/h～						住家で倒壊するものがある。鉄骨構造物で変形するものがある。	

（注1）平均風速は10分間の平均、瞬間風速は3秒間の平均です。風の吹き方は絶えず強弱の変動があり、瞬間風速は平均風速の1.5倍程度になることが多いですが、大気の状態が不安定な場合等は3倍以上になることがあります。

（注2）この表を使用される際は、以下の点にご注意ください。
1 風速は地形や障りの建物などに影響されますので、その場所での風速は近くにある観測所の値と大きく異なることがあります。
2 風速が同じであっても、対象となる建物、構造物の状態や風の吹き方によって被害が異なる場合があります。この表では、ある風速が観測された際に、通常発生する現象や被害を記述していますので、これより大きな被害が発生したり、逆に小さな被害にとどまる場合もあります。
3 人や物への影響は日本風工学会の「瞬間風速と人や街の様子との関係」を参考に作成しています。今後、表現など実状と合わなくなった場合には内容を変更することがあります。

気象庁　〒100-8122 東京都千代田区大手町1-3-4　ホームページ：http://www.jma.go.jp/
TEL：03-3212-8341（代表）　FAX：03-6689-2917（耳の不自由な方向け）

平成26年3月

Appendix A7 Comparing the streaky pattern of the instantaneous wind speed, u_{ins} from the LES-LBM simulation and the Doppler lidar observation.

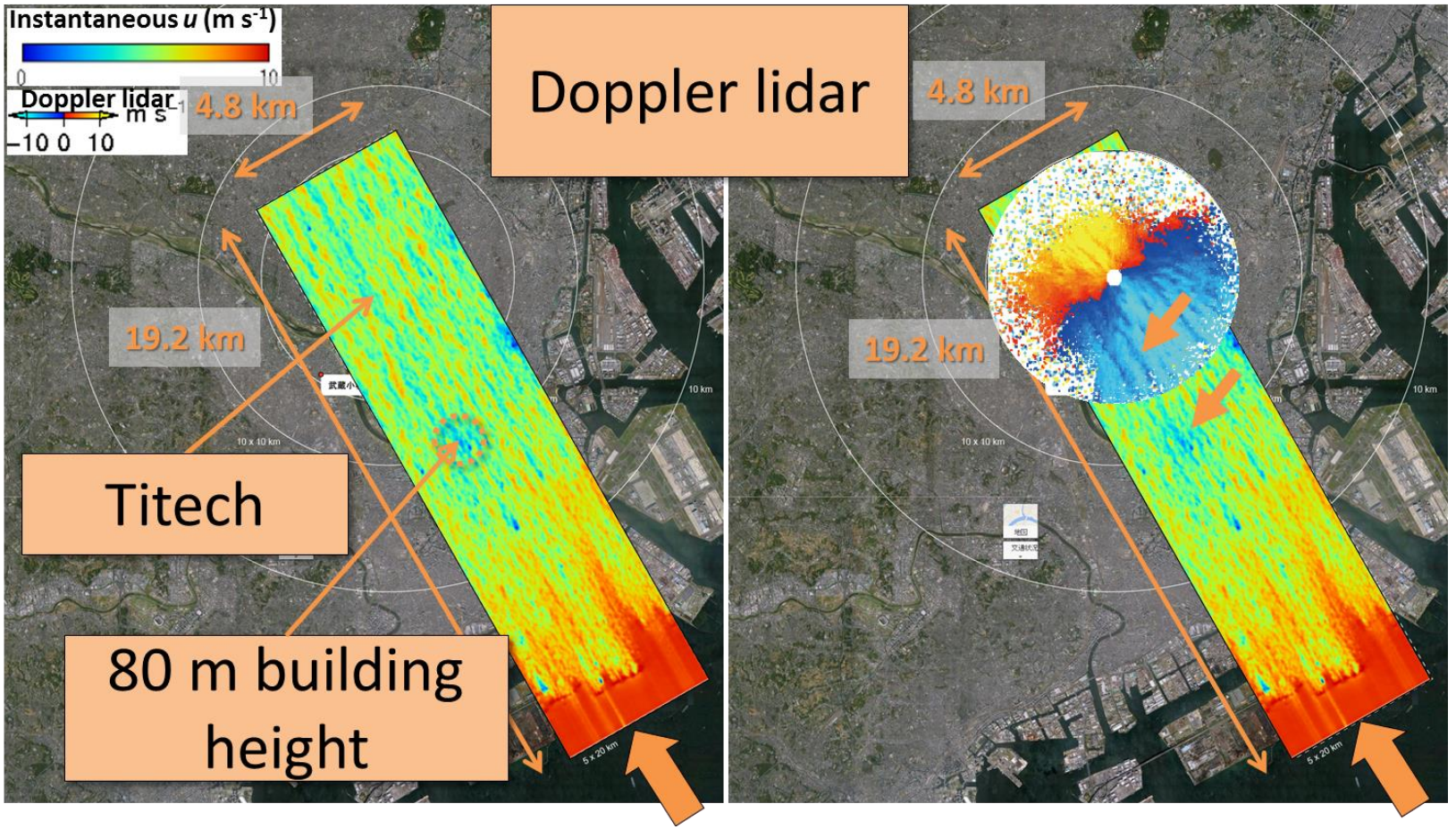

Appendix A8 Decomposition of the whole domain into 400 patches (480 × 480 m^2 for each patch).

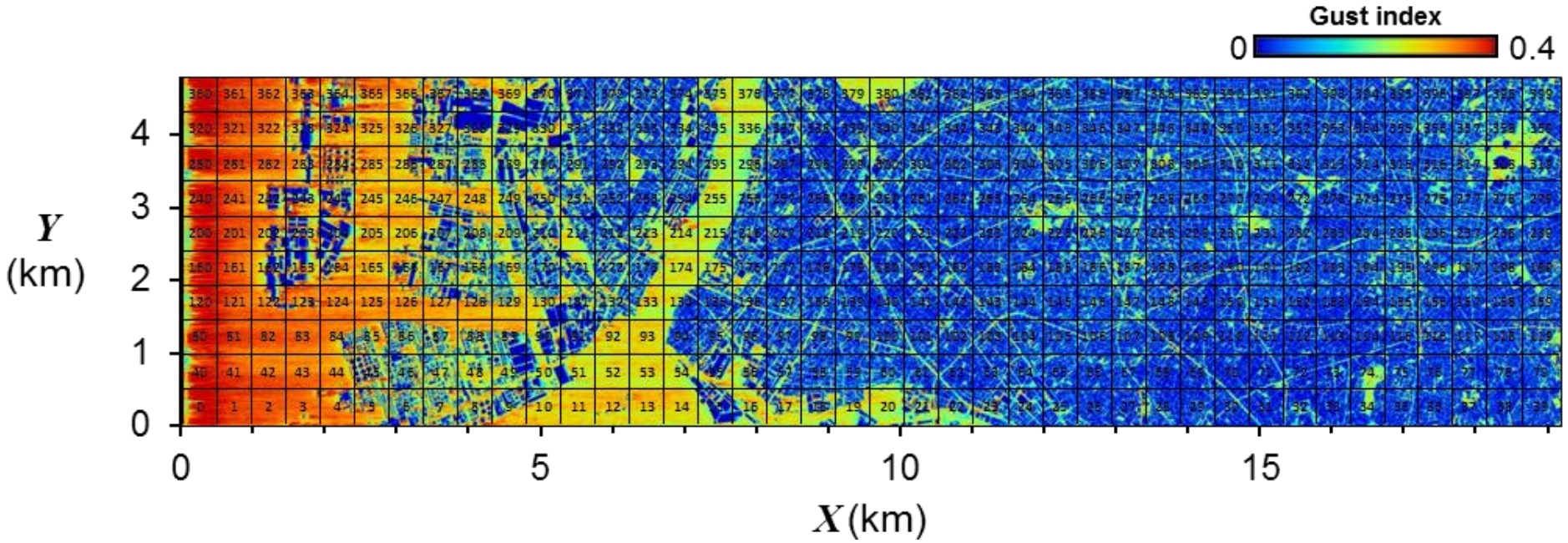

Appendix A9 Program to determine the 'kink' point by using multi-phase linear regression and least mean square method (run using Phyton).

```
# Given xdata(1:n),ydata(1:n)
# Find m={a1,b1,a2,b2,x0} such that we
# Minimize data misfit in least-squares sense
# ie min sum( ydata(1:istar)-a1*xdata(1:istar)-b1 )^2 +
#     sum( ydata(istar+1:end)-a2*xdata(istar+1:end)-b2 )^2
# With constraint: x(istar) <= x0=(b2-b1)/(a1-a2) <= x(istar+1)
#     (ie x0 is the intersection of the two fit lines and is at the break in data
#     between the istarth and istar+1th points.)

import matplotlib.pyplot as plt
import numpy as np

ddir = 'D:\\REGRESS\\'
fname = 'lamdaP_mwr.csv'

#------------------read data and find parameter----------------
f = open(ddir+fname,'r')
lines = f.readlines()[1:]

x=[] ; y=[]
for line in lines:
   line.strip()
   cols=line.split(',')
   x.append(float(cols[0])) ; y.append(float(cols[1]))

print len(x),len(y)
m={}
for i in range(5,150,1):
   star = i

   fit1 = np.polyfit(x[0:star],y[0:star],1) #a=fit[0]   b=fit[1]
   fit1_fn = np.poly1d(fit1)
   y_fit1 = np.polyval(fit1_fn,x[0:star])

   fit2 = np.polyfit(x[star:],y[star:],1)
   fit2_fn = np.poly1d(fit2)
   y_fit2 = np.polyval(fit2_fn,x[star:])

   x0 = (fit2[1]-fit1[1])/(fit1[0]-fit2[0])
   if x0<x[star-1] :continue
   if x0>x[star] :continue

   ydiff1 = (y[star-1]-y_fit1[star-1])**2
   ydiff2 = (y[star]-y_fit2[star])**2
   ydiff = ydiff1 + ydiff2

   m[i]=float(ydiff)

x_star =  min(m,key=m.get)
error_min = m[x_star]
print "your x_0 number is:", x_star, "and your error_min is: ", error_min
#-------------------------------------------------------------------------

#---------------------------------calc regression value-----------
fit1 = np.polyfit(x[0:x_star],y[0:x_star],1) #a=fit[0]   b=fit[1]
fit1_fn = np.poly1d(fit1)
y_fit1 = np.polyval(fit1_fn,x[0:x_star])

ybar1 = np.sum(y[0:x_star]) / len(y[0:x_star])
ssreg1 = np.sum((fit1_fn(x[0:x_star]) - ybar1) ** 2)
sstot1 = np.sum((y[0:x_star] - ybar1) ** 2)
Rsqr1 = ssreg1 / sstot1
print "regression line 1, a1(gradient) and b1:", fit1, "R^2=",Rsqr1

fit2 = np.polyfit(x[x_star:],y[x_star:],1)
fit2_fn = np.poly1d(fit2)
y_fit2 = np.polyval(fit2_fn,x[x_star:])

ybar2 = np.sum(y[x_star:]) / len(y[x_star:])
ssreg2 = np.sum((fit2_fn(x[x_star:]) - ybar2) ** 2)
sstot2 = np.sum((y[x_star:] - ybar2) ** 2)
Rsqr2 = ssreg2 / sstot2
print "regression line 2, a2(gradient) and b2:", fit2, "R^2=",Rsqr2

x0 = (fit2[1]-fit1[1])/(fit1[0]-fit2[0])
print "x_0 defined from reg-line:", x0, "your real x:",x[x_star-1], x[x_star]

#-----------plot image------
fig, ax = plt.subplots(1,1)
ax.set_ylim([0.0,0.3])
ax.plot(x,y,'bo')
ax.plot(x[0:x_star],y_fit1,'r.')
ax.plot(x[x_star:],y_fit2,'g.')
ax.axvline(x[x_star], color='k', linestyle='--')
ax.annotate(str(x[x_star]),xy=(x[x_star],0.005))
ax.annotate("R^2="+str(Rsqr1)[0:4],xy=(0.1,0.12))
ax.annotate("reg-line1:"+str(fit1),xy=(0.1,0.13))
ax.annotate("R^2="+str(Rsqr2)[0:4],xy=(0.05,0.01))
ax.annotate("reg-line2:"+str(fit2),xy=(0.05,0.02))

#plt.show()

plt.savefig('lamdaP_mwr.png')
```

Appendix A10 'Kink' point for the mean wind ratio, $[\widetilde{U}]$, and the turbulent part ratio, $[\widetilde{U}']$, versus the plan area index, λ_p. Spatial average distribution of the 480 × 480 m^2 patches for the last three quarters (Q2+Q3+Q4).